Characterizing the background in $t\bar{t}$ events with a $J/\psi \to \mu^-\mu^+$ in proton-proton collisions at $\sqrt{s} = 13$ TeV using the ATLAS detector

by

Kevin Nicholas Barends

Supervisor: Dr Sahal Yacoob

Co-supervisors: Assist. Prof. Tim Andeen and Prof. Peter Onyisi

A thesis submitted in fulfillment for the
degree of Master of Science

in the

UCT-ATLAS Group
Department of Physics
Faculty of Science
University of Cape Town

June 2019

Declaration of Authorship

I, Kevin Nicholas Barends , declare that this thesis titled, "Characterizing the background in $t\bar{t}$ events with a $J/\psi \to \mu^-\mu^+$ in proton-proton collisions at $\sqrt{s} = 13$ TeV using the ATLAS detector" and the work presented in it are my own. I confirm that:

- This work was done wholly or mainly while in candidature for a research degree at this University.
- Where any part of this thesis has previously been submitted for a degree or any other qualification at this University or any other institution, this has been clearly stated.
- Where I have consulted the published work of others, this is always clearly attributed.
- Where I have quoted from the work of others, the source is always given. With the exception of such quotations, this thesis is entirely my own work.
- I have acknowledged all main sources of help.
- Where the thesis is based on work done by myself jointly with others, I have made clear exactly what was done by others and what I have contributed myself.

Signed: Signed by candidate

Date: February 2019

"Our greatest glory is not in never falling, but in rising every time we fall."

- Confucius

UNIVERSITY OF CAPE TOWN

Abstract

UCT-ATLAS Group
Department of Physics
Faculty of Science

Master of Science

by Kevin Nicholas Barends

So far, various measurements have been performed for the top quark mass using jets as a dominant experimental signature. The leading precision measurement of 1732.44 $\pm$0.13$\pm$0.47 GeV is a combination of top quark mass measurements conducted by the CMS collaboration. However, these various measurements suffered from large jet reconstruction uncertainties. This study looked at a different experimental signature involving a lepton and J/ψ such that the top quark decay mode is t $\rightarrow$ W ($\rightarrow$ lν)b ($\rightarrow$ J/ψ [$\rightarrow$ $\mu^+\mu^-$]+X). This signature combines the kinematics of the three leptons in the final state and therefore, is not significantly dependent on the reconstructed kinematics of the jets. The statistical uncertainty in the top mass measurement was determined from the invariant mass of the lepton and J/ψ distribution through a template morphing maximum likelihood method, giving a value of 2.9 GeV. This signature comes with background contributions from non-prompt and mis-reconstructed leptons and from selecting J/ψ mesons which did not originate from top quark B-hadron decays. The background contribution from non-prompt and mis-reconstructed leptons was determined to be overestimated in the muon channel but more accurately estimated in the electron channel in the signal region. This background lepton contribution was determined using the common methodology by the ATLAS experiment. The background contribution from J/ψ mesons was determined by applying a two-dimensional fit on the mass and pseudo-proper time of the J/ψ. These background contributions were reduced by applying a tighter selection cut on the J/ψ mass and including an additional selection cut on the pseudo-proper time of the J/ψ mesons. These cuts improved the signal contribution but, due to limited statistics, could not be shown to improve the uncertainty in the mass measurement.

Acknowledgements

Firstly, I would like to thank my family and friends for always pushing me to do more than expected, never give and learn from failure. Their emotional and psychological support has given me the strength to go all the way and complete this degree.

Secondly, I would like to thank the National Research Foundation and the University of Cape Town's Postgraduate Funding Office for assisting me financially. I would not have been able to pursue a Master's degree if it were not for their generosity.

Thirdly, I would like to thank my co-supervisors Professor Peter Onyisi and Assistant Professor Tim Andeen. They were always willing to assist whenever I needed help as well as gave up loads of their unscheduled time to ensure I get a better understanding.

Lastly, I would like to extend my admiration and appreciation to my supervisor Sahal Yacoob. He was always there for me when I needed any assistance both academically and personally. He was always willing to listen and would try his utmost to guide me in the right direction. I would not have been introduced to the wonderful world of CERN and the particle physics community if it were not for him. Thank you Sahal.

Contents

Declaration of Authorship i

Abstract iii

Acknowledgements iv

List of Figures viii

List of Tables xiii

Abbreviations xiv

1 Introduction 1

2 Theoretical Overview 3
2.1 The Standard Model of particle physics . . . 3
2.1.1 Fermions . . . 3
2.1.2 Bosons . . . 4
2.1.3 Standard Model Interactions . . . 5
2.1.4 Standard Model Lagrangian . . . 5
2.1.5 Vacuum Stability of the Standard Model . . . 7
2.1.6 Particle Decays in the Standard Model . . . 8
2.2 Top Quark . . . 9
2.2.1 Physical processes of the top quark . . . 9
2.2.1.1 Single-top . . . 9
2.2.1.2 Top quark pair production . . . 10
2.2.2 Definition of the top mass . . . 11
2.2.3 A review on the different top quark mass measurements . . . 12

3 CERN and the LHC 13
3.1 CERN . . . 13
3.2 The Large Hadron Collider . . . 14
3.2.1 Luminosity . . . 15

4 The ATLAS Detector 17
4.1 Overview . . . 17
4.1.1 The Coordinate System . . . 18

4.2 The Magnet System . . . 19
4.3 Inner Detector . . . 20
4.4 Calorimeters . . . 20
4.5 Muon Spectrometer . . . 22
4.6 Forward Detectors . . . 23
4.7 Trigger and Data Acquisition System . . . 23
4.8 Pile-up . . . 23

5 Particle reconstruction and identification within the ATLAS detector 25
5.1 Overview . . . 25
5.2 Charged Particles in the Inner Detector . . . 26
5.3 Electrons and Photons . . . 27
5.4 Muons . . . 27
5.5 Jets . . . 28
5.5.1 b-tagged Jets . . . 29
5.6 Missing Transverse Energy . . . 29
5.7 Lepton Isolation . . . 30

6 Analysis 31
6.1 Data and Simulation . . . 32
6.2 Preselection . . . 33
6.3 Experimental Signature . . . 34
6.3.1 W boson: Electrons . . . 34
6.3.2 W boson: Muons . . . 35
6.3.3 B-tagged jets . . . 36
6.3.4 J/ψ: Muons . . . 36
6.4 Non-prompt and Fake Lepton Background . . . 36
6.4.1 Overview . . . 36
6.4.2 Data and Simulation . . . 37
6.4.3 Object Selection . . . 38
6.4.4 Matrix Method . . . 38
6.4.5 Measurement of the real efficiency . . . 39
6.4.6 Measurement of the fake efficiency . . . 40
6.4.7 Efficiencies . . . 42
6.4.8 Validation of measured efficiencies . . . 43
6.5 Signal region object kinematics . . . 45
6.6 J/ψ background . . . 49
6.6.1 Non-prompt signal J/ψ determination . . . 51
6.6.2 Non-prompt signal J/ψ sanity check . . . 54
6.6.3 Throwing away unwanted J/ψ mesons . . . 54
6.6.4 Double parton scattering . . . 56
6.7 Uncertainty in the top mass measurement . . . 57
6.7.1 Extracting the mass from the data . . . 57
6.7.2 Impact on the uncertainty measurement . . . 60
6.7.2.1 Tighter J/ψ mass cut . . . 60
6.7.2.2 Additional pseudo-proper time cut . . . 62
6.7.2.3 Tighter J/ψ mass and an additional pseudo-proper time cut . . . 63

7 Conclusion **66**

A Signal region object kinematics **70**

Bibliography **73**

List of Figures

2.1 An illustration of the fundamental particles within the SM. . . . 4
2.2 An illustration showing the particles in each successive generation of fermions being heavier than the particles in the former generation, except in the neutrino case as their masses are still unknown. The area of each illustration is indicative of the corresponding particle's mass. . . . 4
2.3 These Feynman diagrams show examples of the allowed interactions within the SM while the descriptions describe the rest of the allowed interactions. . . . 5
2.4 The SM Lagrangian in its incredible detail. . . . 6
2.5 The SM Lagrangian extremely compressed to fit on a mug. . . . 7
2.6 Regions of absolute stability, meta-stability and instability of the SM vacuum in the top mass-Higgs mass plane. The black dot shows the current state of the vacuum of the SM. . . . 8
2.7 Single top t-channel production process where a top quark is produced along with a d, s or b quark. . . . 10
2.8 Single top s-channel production process where a top quark is produced along with an anti-b quark. . . . 10
2.9 W+top quark associated production process where a top quark is produced along with a W boson. . . . 10
2.10 Top quark pair production where a top and anti-top quark is produced from gluon interactions. . . . 11
2.11 Top quark pair production where a top and anti-top quark is produced from quarks annihilating. . . . 11

3.1 An illustration showing the accelerator complex at CERN. . . . 14
3.2 The cumulative luminosity delivered to ATLAS (green) and recorded by ATLAS (yellow) during stable beams for proton-proton collisions at $\sqrt{s} = 13$ TeV in the LHC during the data-taking period between 2015 and 2018. . . . 16

4.1 An illustration showing the ATLAS detector and all its sub-detectors. . . . 18
4.2 An illustration of the ATLAS coordinate system. . . . 19
4.3 The solenoid magnet in the factory after winding the coils. . . . 19
4.4 An illustration showing the geometry of the eight barrel and eight end-cap toroid coils. . . . 19
4.5 An illustration of the ATLAS inner detector showing all three subdetectors. . . . 20
4.6 An illustration of the ATLAS calorimeters showing all three subdetectors. . . . 21
4.7 An illustration of the ATLAS muon subsystem. . . . 22
4.8 An illustration of the ATLAS forward detectors. . . . 23

4.9 The recorded luminosity distribution of the mean number of interactions per bunch crossing in proton-proton collisions for the data-taking period of 2015-2018 at $\sqrt{s} = 13$ TeV. 24

5.1 An illustration showing detector signatures for different particles in the ATLAS detector. 26

6.1 Distributions of the transverse momentum p_T for data and the contribution from the different SM processes for events passing the tight (left) and loose (right) selection criteria when the selected lepton is an electron candidate. 41
6.2 Distributions of the pseudorapidity for data and the contribution from the different SM processes for events passing the tight (left) and loose (right) selection criteria when the selected lepton is an electron candidate. 41
6.3 Distributions of the transverse momentum p_T for data and the contribution from the different SM processes for events passing the tight (left) and loose (right) selection criteria when the selected lepton is a muon candidate. 42
6.4 Distributions of the pseudorapidity for data and the contribution from the different SM processes for events passing the tight (left) and loose (right) selection criteria when the selected lepton is an muon candidate. 42
6.5 The measured real ϵ_{real} (blue) and fake ϵ_{fake} (red) efficiencies in the transverse momentum (left) and pseudorapidity (right) distributions in the muon channel. No systematic uncertainties are shown. 43
6.6 The measured real ϵ_{real} (blue) and fake ϵ_{fake} (red) efficiencies in the transverse momentum (left) and pseudorapidity (right) distributions in the electron channel. No systematic uncertainties are shown. 43
6.7 Distributions of the transverse momentum p_T (left) and pseudorapidity η (right) in the electron channel for data including the contributions from the non-prompt or fake lepton backgrounds and the different SM processes within the validation region. The lower plot shows the ratio between the data and the theoretical prediction. 44
6.8 Distributions of the transverse momentum p_T (left) and pseudorapidity η (right) in the muon channel for data including the contributions from the non-prompt or fake lepton backgrounds and the different SM processes within the validation region. The lower plot shows the ratio between the data and the theoretical prediction. 45
6.9 Distributions of the transverse momentum p_T (left) and pseudorapidity η (right) in the muon channel for data including the contributions from the non-prompt or fake lepton backgrounds after scaling by a constant factor of 1.8 and the different SM processes within the validation region. The lower plot shows the ratio between the data and the theoretical prediction. 45
6.10 The upper plot shows the distributions of the transverse momentum (left) and pseudorapidity (right) of the lepton candidates in the signal region muon channel. These distributions contain the data, the contributions from the different signal and background SM processes and the contribution from non-prompt or fake lepton backgrounds. Only the statistical uncertainty in the data is shown. The lower plot shows the ratio between the data and the theoretical predictions. . . . 47

6.11 The upper plot shows the distributions of the transverse momentum (left) and pseudorapidity (right) of the lepton candidates in the signal region electron channel. These distributions contain the data, the contributions from the different signal and background SM processes and the contribution from non-prompt or fake lepton backgrounds. Only the statistical uncertainty in the data is shown. The lower plot shows the ratio between the data and the theoretical predictions. 47
6.12 The upper plot shows the distributions of the transverse momentum (left) and pseudorapidity (right) of the muon candidates coming from the J/ψ in the signal region electron channel. These distributions contain the data, the contributions from the different signal and background SM processes and the contributions from non-prompt or fake lepton backgrounds. Only the statistical uncertainty in the data is shown. The lower plot shows the ratio between the data and the theoretical predictions. 48
6.13 The upper plot shows the distributions of the transverse momentum (left) and pseudorapidity (right) of the J/ψ candidates in the signal region electron channel. These distributions contain the data, the contributions from the different signal and background SM processes and the contribution from non-prompt or fake lepton backgrounds. Only the statistical uncertainty in the data is shown. The lower plot shows the ratio between the data and the theoretical predictions. . . . 48
6.14 The upper plot shows the invariant mass distribution of the muon pairs matched to a common vertex in the signal region electron channel. This distribution contains the data, the contributions from the different signal and background SM processes and the contribution from non-prompt or fake lepton backgrounds. Only the statistical uncertainty in the data is shown. The peak within the plot represents the resonant J/ψ meson mass. The lower plot shows the ratio between the data and the theoretical predictions. 49
6.15 The upper plot shows the invariant mass distribution of the lepton and J/ψ candidates in the signal region electron channel. This distributions contains the data, the contributions from the different signal and background SM processes and the contribution from non-prompt or fake lepton backgrounds. Only the statistical uncertainty in the data is shown. The peak within the plot represents the signal contribution while the tail represents the background contribution to the top mass value which produced this distribution. The lower plot shows the ratio between the data and the theoretical predictions. 49
6.16 The upper plot shows the pseudo-proper time distribution of the J/ψ candidates in the signal region electron channel. This distribution contains the data, the contributions from the different signal and background SM processes and the contribution from non-prompt or fake lepton backgrounds. Only the statistical uncertainty in the data is shown. The peak within the plot represents the contribution from prompt J/ψ mesons. The lower plot shows the ratio between the data and the theoretical predictions. 51
6.17 Two-dimensional plot of the pseudo-proper time of the J/ψ candidates and the invariant mass of the dimuon pair in the signal region. On the left is the color map where the right y-axis represents the counts and on the right is the lego plot. 52
6.18 The invariant mass distribution of the dimuon pair (on the left) and the pseudo-proper time distribution of the J/ψ candidates (on the right) with the contributions from each individual process as well as the total contribution. The prompt J/ψ contribution comes out to be very small and can be seen by the red projections. 53

6.19 The invariant mass distribution of the dimuon pair (on the left) and the pseudo-proper time distribution of the J/ψ candidates (on the right) with the contributions from each individual process as well as the total contribution. The prompt J/ψ contribution comes out to be very small and can be seen by the red projection. 54
6.20 The left plot is the pseudo-proper time distribution of the J/ψ candidates after a tighter J/ψ mass selection cut between 2.9 GeV and 3.3 GeV was only applied. The right plot is the invariant mass distribution of the dimuon pair after the pseudo-proper time selection cut of $\tau > 0$ ps was only applied. In each distribution, the contributions from the individual processes as well as the total contribution is shown. The prompt J/ψ contribution comes out to be very small and can be seen by the red projection. 55
6.21 The invariant mass distribution of the dimuon pair (on the left) and the pseudo-proper time distribution of the J/ψ candidates (on the right) after a tighter J/ψ mass selection between 2.9 GeV and 3.3 GeV and a pseudo-proper time selection cut of $\tau > 0$ ps was applied. In each distribution, the contributions from the individual processes as well as the total contribution is shown. The prompt J/ψ contribution comes out to be very small and can be seen by the red projection. . 56
6.22 The invariant mass distribution of the J/ψ and lepton candidates for the data and the two template MC samples. The MC samples were normalized to data. . 58
6.23 The invariant mass distribution of the J/ψ and lepton candidates for the 170 GeV (left) and 175 GeV (right) MC samples in the signal region. The probability density function fit and the signal and background components are shown. 59
6.24 The interpolated templates which represent the invariant mass distribution of the J/ψ and lepton candidates for different values for the top mass, starting with two MC template samples of 170 GeV and 175 GeV is shown on the left. The invariant mass distribution of the J/ψ and lepton candidates for data and the probability density function fit result of the interpolation between 170 GeV and 175 GeV is shown on the right. In the upper right of the right plot, the statistical uncertainty of the top mass measurement is shown. 60
6.25 The invariant mass distribution of the J/ψ and lepton candidates for the 170 GeV (left) and 175 GeV (right) MC samples in the signal region after applying a tighter J/ψ mass selection between 2.9 GeV and 3.3 GeV. The probability density function fit and the signal and background components are shown. 61
6.26 The mass distribution of the J/ψ candidates in the signal region after applying a tighter J/ψ mass selection cut to be between 2.9 GeV and 3.3 GeV for data and the two template MC samples. 62
6.27 The invariant mass distribution of the J/ψ and lepton candidates for the 170 GeV (left) and 175 GeV (right) MC samples in the signal region after applying a pseudo-proper time selection cut of $\tau > 0$ ps on the J/ψ candidates. The probability density function fit and the signal and background components are shown. 62
6.28 The invariant mass distribution of the J/ψ and lepton candidates for the 170 GeV (left) and 175 GeV (right) MC samples in the signal region after applying a tighter J/ψ mass selection cut to be between 2.9 GeV and 3.3 GeV and a pseudo-proper time selection cut of $\tau > 0$ ps on the J/ψ candidates. The probability density function fit and the signal and background components are shown. 64

6.29 The mass distribution of the J/ψ candidates in the signal region after applying a tighter J/ψ mass selection cut to be between 2.9 GeV and 3.3 GeV and a pseudo-proper time selection cut of $\tau > 0$ ps on the J/ψ candidates for data and the two template MC samples. 65

A.1 The upper plot shows the distributions of the transverse momentum (left) and pseudorapidity (right) of the muon candidates coming from the J/ψ in the signal region muon channel. These distributions contain the data, the contributions from the different signal and background SM processes and the contributions from non-prompt or fake lepton backgrounds. Only the statistical uncertainty in the data is shown. The lower plot shows the ratio between the data and the theoretical predictions. 70

A.2 The upper plot shows the distributions of the transverse momentum (left) and pseudorapidity (right) of the J/ψ candidates in the muon channel in the signal region muon channel. These distributions contain the data, the contributions from the different signal and background SM processes and the contribution from non-prompt or fake lepton backgrounds. Only the statistical uncertainty in the data is shown. The lower plot shows the ratio between the data and the theoretical predictions. 71

A.3 The upper plot shows the invariant mass distribution of the muon pairs matched to a common vertex in the signal region muon channel. This distribution contains the data, the contributions from the different signal and background SM processes and the contribution from non-prompt or fake lepton backgrounds. Only the statistical uncertainty in the data is shown. The peak within the plot represents the resonant J/ψ meson mass. The lower plot shows the ratio between the data and the theoretical predictions. 71

A.4 The upper plot shows the pseudo-proper time distribution of the J/ψ candidates in the signal region muon channel. This distribution contains the data, the contributions from the different signal and background SM processes and the contribution from non-prompt or fake lepton backgrounds. Only the statistical uncertainty in the data is shown. The peak within the plot represents the contribution from prompt J/ψ mesons. The lower plot shows the ratio between the data and the theoretical predictions. 71

A.5 The upper plot shows the invariant mass distribution of the lepton and J/ψ candidates in the signal region muon channel. This distributions contains the data, the contributions from the different signal and background SM processes and the contribution from non-prompt or fake lepton backgrounds. Only the statistical uncertainty in the data is shown. The peak within the plot represents the signal contribution while the tail represents the background contribution to the top mass value which produced this distribution. The lower plot shows the ratio between the data and the theoretical predictions. 72

List of Tables

6.1 Different single electron and muon triggers used in each data period. 34
6.2 Electron candidates passing the above criteria were considered signal electrons. . 35
6.3 Muon candidates passing the above criteria were considered signal muons. 35
6.4 Different preselection processes before selecting good collision data. 37
6.5 Parameter fit results of the two $t\bar{t}$ MC samples. 59
6.6 Parameter fit results of the two $t\bar{t}$ MC samples after applying a tighter selection on the mass of the J/ψ candidates to be between 2.9 GeV and 3.3 GeV. 61
6.7 Parameter fit results of the two $t\bar{t}$ MC samples after applying an additional pseudo-proper time selection cut of $\tau > 0$ on the J/ψ candidates. 63
6.8 Parameter fit results of the two $t\bar{t}$ MC samples after applying a tighter mass selection between 2.9 GeV and 3.3 GeV and an additional pseudo-proper time selection $\tau > 0$ ps on the J/ψ candidates. 64

Abbreviations

AFP	ATLAS Forward Proton
ALFA	Absolute Luminosity For ATLAS
ALICE	A Large Ion Collider Experiment
BSM	Beyond the Standard Model
CERN	Conseil Européen pour la Recherche Nucléaire (European Council for Nuclear Research)
CMS	Compact Muon Spectrometer
CSC	Cathode-Strip Chamber
DAQ	Data AcQuisition
ECal	Electromagnetic Calorimeter
FCal	Forward Calorimeter
GEANT4	GEometry ANd Tracking 4
HCal	Hadronic Calorimeter
HLT	High Level Trigger
IBL	Insertable B-Layer
ID	Inner Detector
L1	Level-1
LAr	Liquid-Argon
LEP	Large Electron Positron
LH	LikeliHood
LHC	Large Hadron Collider
LHCb	LHC-beauty
LINAC	LINac ACcelerator
LUCID	LUminosity measurement using Cherenkov Integration Detector
MC	Monte Carlo

MDT	Monitored Drift Tube
$\overline{\text{MS}}$	Modified Minimal Subtraction
MS	Muon Spectrometer
NPFL	Non-Prompt and Fake Lepton
OS	Opposite Sign
PDG	Particle Data Group
PS	Proton Synchrotron
PSB	Proton Synchrotron Booster
QCD	Quantum Chromodynamics
QED	Quantum Electrodynamics
QFT	Quantum Field Theory
RPC	Resistive Plate Chamber
SCT	SemiConductor Tracker
SM	Standard Model
SPS	Super Proton Synchrotron
SS	Same Sign
TDAQ	Trigger and Data AcQuisition
TGC	Thin Gap Chamber
TRT	Transition Radiation Tracker
WWW	World Wide Web
ZDC	Zero-Degree Calorimeter

Chapter 1

Introduction

The top quark is the heaviest quark within the Standard Model (SM) and, since its discovery in 1995 [1, 2], its mass has been a widely sought after result [3–7]. The mass of the top quark plays significant roles in a number of areas in physics [6, 7] but most importantly in two specific areas: 1) in determining the vacuum stability of the SM [8], and 2) by providing a good test for physics Beyond the SM (BSM) with its unique link to the electroweak and Higgs sectors [8–12]. Many different experiments and collaborations [6, 7] have studied and determined the mass of the top quark through direct measurements, which is currently quoted as 173.0 ± 0.4 GeV [13]. Despite the fact that the relative uncertainty of this measurement is 0.23 %, the precision of this measurement needs to improve as the precision of the vacuum stability of the SM is highly dependent on this uncertainty [8, 14].

The precision of any measurement is estimated by its associated uncertainty and therefore reducing the associated uncertainty should be the number one goal when trying to make a more accurate measurement. One way of doing this is by understanding and characterizing the different physical processes and reconstructed objects which are directly linked to the top quark (known as signal) to those which mimic the properties of the top quark (also called background).

There are many different ways to measure the mass of the top quark which all stem from two different methods, i.e. direct and indirect measurements. Direct measurements utilize the kinematic information of the decay products which come directly from the top quark [7] while indirect measurements utilize differential top and anti-top cross-section measurements and compares these measurements to theory calculations [7], in order to determine the mass of the top quark. The current measurement of the mass of the top quark mentioned above is an average of measurements made by Large Hadron Collider and Tevatron experiments which implemented a direct measurement approach [15–18]. Each experiment used common experimental signatures related to the decay products of the top quark, i.e. lepton + jets, dilepton + jets and/ or all jets, to determine the mass of the top quark. These experimental signatures combine the full

kinematic information provided by the jets with the full kinematic information provided by the lepton(s) - only for those signatures which select a lepton(s) - to determine the mass of the top quark. Therefore, the mass of the top quark within these experimental signatures is heavily dependent on reconstructing the jets with great precision since one of the biggest sources of uncertainty comes from the jet energy scale [15–18].

There are other less common decay modes of the top quark which result in new experimental signatures that could be used to measure the mass of the top quark more precisely. One uncommon experimental signature which reduces the aforementioned jet uncertainty, is lepton + b-tagged jets + J/ψ where the J/ψ decayed into two oppositely charged muons. This experimental signature seems to be quite similar to the common signatures mentioned above but instead combines the full kinematic information of the muons from the J/ψ as well as the additional lepton. This signature relies on a b quark hadronising and the B-hadron decaying to a J/ψ meson which only occurs 1.65 $\pm$ 0.14 % of the time [13]. Furthermore, only 5.961 $\pm$ 0.033 % of J/ψ mesons decay into two oppositely charged muons [13]. Therefore, this signature is statistically limited and was never studied to determine the mass of the top quark until 2016. The CMS collaboration made the first measurement of the mass of the top quark using b quark to J/ψ mesons in 2016 as enough data became available at the Large Hadron Collider [19] . This three lepton signature is almost devoid of the background physical processes [19] but it is, however, still sensitive to mis-reconstructed objects [20, 21].

In this thesis, the associated background within this uncommon experimental signature is estimated and its effect on the associated uncertainty of the mass of the top quark is determined. This analysis was performed using data collected from proton-proton collisions at a centre-of-mass energy $\sqrt{s} = 13$ TeV by the ATLAS detector in 2015 and 2016.

Chapter 2

Theoretical Overview

The following chapter consists of information from "Modern Particle Physics" [22] and "Introduction to Particle Physics" [23], unless otherwise stated.

2.1 The Standard Model of particle physics

The SM of particle physics [24–26] encapsulates the current understanding of the building blocks of matter and how these building blocks interact. The building blocks are called fermions and their interactions are governed by three of the four fundamental forces which are mediated by bosons and described by the SM. The gravitational force is not yet described by the SM. Collectively, the fermions and bosons are known as fundamental particles.

2.1.1 Fermions

The SM consists of twelve fermions, which can be seen in Figure 2.1, and twelve anti-fermions. The anti-fermions are identical to their fermion counterparts except they have an opposite electrical charge and therefore every description made about the fermions applies to the anti-fermions.

Fermions can be broken down into two main categories: quarks and leptons; with six particles (or flavours) in each category. These categories can be further broken down into three families (or generations): first, second and third. The three generations each consists of two quarks and two leptons and are almost exactly identical to each other. The difference lies in the mass of the particles in each generation, i.e. each successive generation's quarks and leptons (except for the neutrinos) are heavier than the former generations (see Figure 2.2). The neutrinos might have heavier masses as you traverse through the generations but their masses have not yet

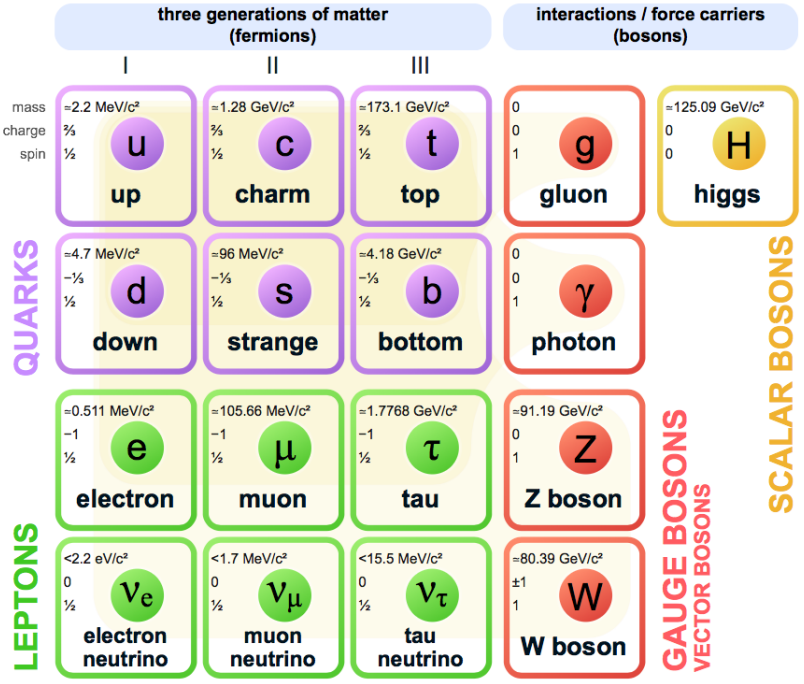

FIGURE 2.1: An illustration of the fundamental particles within the SM [27].

been accurately determined. The first generation is responsible for all of visible matter in the Universe while the second and third generations only appear in highly energetic domains.

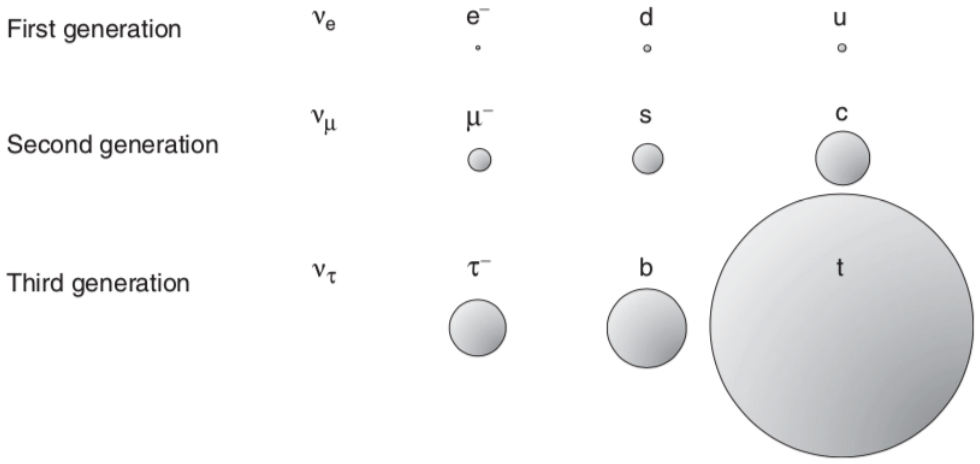

FIGURE 2.2: An illustration showing the particles in each successive generation of fermions being heavier than the particles in the former generation, except in the case of neutrinos as their masses are still unknown. The area of each illustration is indicative of the corresponding particle's mass [22].

2.1.2 Bosons

The SM consists of six bosons (see Figure 2.1, where the W^+ and W^- boson are shown in one block): five gauge (vector) bosons and one scalar boson. The one scalar boson, known as

the Higgs boson, is responsible for the mass of all fundamental particles while the five gauge bosons mediate the interactions between the fundamental particles. These interactions are governed by three fundamental forces: the electromagnetic force, the weak force and the strong force. Each fundamental force is described by a specific Quantum Field (gauge) Theory (QFT): electromagnetic force by Quantum Electrodynamics (QED), the weak force by the Weak Theory and the strong force by Quantum Chromodynamics (QCD). However, the Weak Theory and QED unify into one theory known as the Electroweak Theory at high energies.

2.1.3 Standard Model Interactions

The three fundamental forces govern the interactions between fundamental particles and each interaction is described by the properties within each field theory (see Figure 2.3). In the case of:

- Electromagnetic Force: Interactions occur between electrically charged particles which are mediated by a photon.
- Strong Force: Interactions occur between quarks which are mediated by a gluon.
- Weak Force: Interactions occur between all fermions and are mediated by the W boson (which changes flavour) or the Z boson (which never changes flavour).

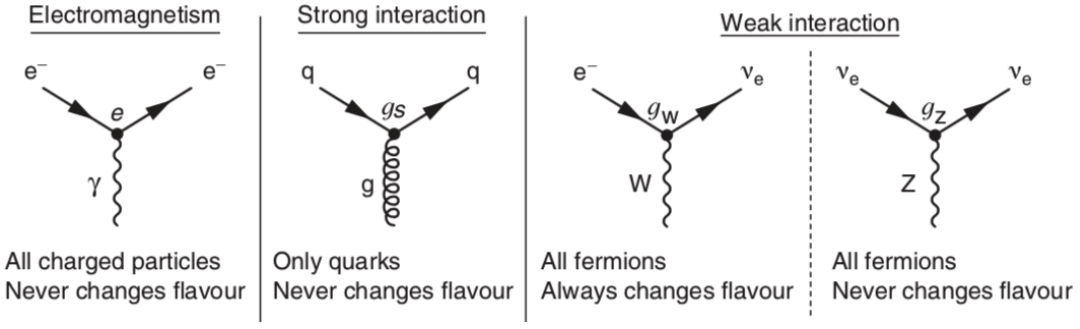

FIGURE 2.3: These Feynman diagrams show examples of the allowed interactions within the SM while the descriptions describe the rest of the allowed interactions [22].

2.1.4 Standard Model Lagrangian

Due to the fact that the SM involves three gauge theories to describe and explain fundamental particles and their interactions, the SM itself is a gauge theory. It combines the SU(3) symmetric group with the SU(2) $\times$ U(1) symmetric group, which represents the strong and electroweak forces respectively. These three symmetric groups give rise to a single equation which describes

every known interaction within the three fundamental forces. This equation, in incredible detail, is an extremely long equation and is of the form

$$
\begin{aligned}
&\mathcal{L}_{\text{StandardModel}} = \\
&-\tfrac{1}{2}\partial_\nu g^a_\mu \partial_\nu g^a_\mu - g_s f^{abc}\partial_\mu g^a_\nu g^b_\mu g^c_\nu - \tfrac{1}{4}g_s^2 f^{abc} f^{ade} g^b_\mu g^c_\nu g^d_\mu g^e_\nu + \\
&\tfrac{1}{2}ig_s^2(\bar{q}^\sigma_i \gamma^\mu q^\sigma_j) g^a_\mu + \bar{G}^a \partial^2 G^a + g_s f^{abc}\partial_\mu \bar{G}^a G^b g^c_\mu - \partial_\nu W^+_\mu \partial_\nu W^-_\mu - \\
&M^2 W^+_\mu W^-_\mu - \tfrac{1}{2}\partial_\nu Z^0_\mu \partial_\nu Z^0_\mu - \tfrac{1}{2c_w^2} M^2 Z^0_\mu Z^0_\mu - \tfrac{1}{2}\partial_\mu A_\nu \partial_\mu A_\nu - \tfrac{1}{2}\partial_\mu H \partial_\mu H - \\
&\tfrac{1}{2}m_h^2 H^2 - \partial_\mu \phi^+ \partial_\mu \phi^- - M^2 \phi^+ \phi^- - \tfrac{1}{2}\partial_\mu \phi^0 \partial_\mu \phi^0 - \tfrac{1}{2c_w^2} M \phi^0 \phi^0 - \beta_h [\tfrac{2M^2}{g^2} + \\
&\tfrac{2M}{g} H + \tfrac{1}{2}(H^2 + \phi^0 \phi^0 + 2\phi^+ \phi^-)] + \tfrac{2M^4}{g^2}\alpha_h - igc_w[\partial_\nu Z^0_\mu (W^+_\mu W^-_\nu - \\
&W^+_\nu W^-_\mu) - Z^0_\nu (W^+_\mu \partial_\nu W^-_\mu - W^-_\mu \partial_\nu W^+_\mu) + Z^0_\mu (W^+_\nu \partial_\nu W^-_\mu - \\
&W^-_\nu \partial_\nu W^+_\mu)] - igs_w[\partial_\nu A_\mu (W^+_\mu W^-_\nu - W^+_\nu W^-_\mu) - A_\nu (W^+_\mu \partial_\nu W^-_\mu - \\
&W^-_\mu \partial_\nu W^+_\mu) + A_\mu (W^+_\nu \partial_\nu W^-_\mu - W^-_\nu \partial_\nu W^+_\mu)] - \tfrac{1}{2}g^2 W^+_\mu W^-_\mu W^+_\nu W^-_\nu + \\
&\tfrac{1}{2}g^2 W^+_\mu W^-_\nu W^+_\mu W^-_\nu + g^2 c_w^2 (Z^0_\mu W^+_\mu Z^0_\nu W^-_\nu - Z^0_\mu Z^0_\mu W^+_\nu W^-_\nu) + \\
&g^2 s_w^2 (A_\mu W^+_\mu A_\nu W^-_\nu - A_\mu A_\mu W^+_\nu W^-_\nu) + g^2 s_w c_w [A_\mu Z^0_\nu (W^+_\mu W^-_\nu - \\
&W^+_\nu W^-_\mu) - 2A_\mu Z^0_\mu W^+_\nu W^-_\nu] - g\alpha[H^3 + H\phi^0\phi^0 + 2H\phi^+\phi^-] - \\
&\tfrac{1}{8}g^2\alpha_h[H^4 + (\phi^0)^4 + 4(\phi^+\phi^-)^2 + 4(\phi^0)^2\phi^+\phi^- + 4H^2\phi^+\phi^- + 2(\phi^0)^2 H^2] - \\
&gMW^+_\mu W^-_\mu H - \tfrac{1}{2}g\tfrac{M}{c_w^2} Z^0_\mu Z^0_\mu H - \tfrac{1}{2}ig[W^+_\mu(\phi^0\partial_\mu\phi^- - \phi^-\partial_\mu\phi^0) - \\
&W^-_\mu(\phi^0\partial_\mu\phi^+ - \phi^+\partial_\mu\phi^0)] + \tfrac{1}{2}g[W^+_\mu(H\partial_\mu\phi^- - \phi^-\partial_\mu H) - W^-_\mu(H\partial_\mu\phi^+ - \\
&\phi^+\partial_\mu H)] + \tfrac{1}{2}g\tfrac{1}{c_w}(Z^0_\mu(H\partial_\mu\phi^0 - \phi^0\partial_\mu H) - ig\tfrac{s_w^2}{c_w} M Z^0_\mu (W^+_\mu\phi^- - W^-_\mu\phi^+) + \\
&igs_w M A_\mu (W^+_\mu \phi^- - W^-_\mu \phi^+) - ig\tfrac{1-2c_w^2}{2c_w} Z^0_\mu (\phi^+\partial_\mu\phi^- - \phi^-\partial_\mu\phi^+) + \\
&igs_w A_\mu (\phi^+\partial_\mu\phi^- - \phi^-\partial_\mu\phi^+) - \tfrac{1}{4}g^2 W^+_\mu W^-_\mu [H^2 + (\phi^0)^2 + 2\phi^+\phi^-] - \\
&\tfrac{1}{4}g^2\tfrac{1}{c_w^2} Z^0_\mu Z^0_\mu [H^2 + (\phi^0)^2 + 2(2s_w^2 - 1)^2 \phi^+\phi^-] - \tfrac{1}{2}g^2\tfrac{s_w^2}{c_w} Z^0_\mu \phi^0 (W^+_\mu \phi^- + \\
&W^-_\mu \phi^+) - \tfrac{1}{2}ig^2\tfrac{s_w^2}{c_w} Z^0_\mu H (W^+_\mu \phi^- - W^-_\mu \phi^+) + \tfrac{1}{2}g^2 s_w A_\mu \phi^0 (W^+_\mu \phi^- + \\
&W^-_\mu \phi^+) + \tfrac{1}{2}ig^2 s_w A_\mu H (W^+_\mu \phi^- - W^-_\mu \phi^+) - g^2\tfrac{s_w}{c_w}(2c_w^2 - 1) Z^0_\mu A_\mu \phi^+\phi^- - \\
&g^1 s_w^2 A_\mu A_\mu \phi^+\phi^- - \bar{e}^\lambda(\gamma\partial + m^\lambda_e)e^\lambda - \bar{\nu}^\lambda \gamma\partial\nu^\lambda - \bar{u}^\lambda_j(\gamma\partial + m^\lambda_u)u^\lambda_j - \\
&\bar{d}^\lambda_j(\gamma\partial + m^\lambda_d)d^\lambda_j + igs_w A_\mu[-(\bar{e}^\lambda\gamma^\mu e^\lambda) + \tfrac{2}{3}(\bar{u}^\lambda_j\gamma^\mu u^\lambda_j) - \tfrac{1}{3}(\bar{d}^\lambda_j\gamma^\mu d^\lambda_j)] + \\
&\tfrac{ig}{4c_w} Z^0_\mu [(\bar{\nu}^\lambda\gamma^\mu(1+\gamma^5)\nu^\lambda) + (\bar{e}^\lambda\gamma^\mu(4s_w^2 - 1 - \gamma^5)e^\lambda) + (\bar{u}^\lambda_j\gamma^\mu(\tfrac{4}{3}s_w^2 - \\
&1 - \gamma^5)u^\lambda_j) + (\bar{d}^\lambda_j\gamma^\mu(1 - \tfrac{8}{3}s_w^2 - \gamma^5)d^\lambda_j)] + \tfrac{ig}{2\sqrt{2}} W^+_\mu [(\bar{\nu}^\lambda\gamma^\mu(1+\gamma^5)e^\lambda) + \\
&(\bar{u}^\lambda_j\gamma^\mu(1+\gamma^5)C_{\lambda\kappa}d^\kappa_j)] + \tfrac{ig}{2\sqrt{2}} W^-_\mu [(\bar{e}^\lambda\gamma^\mu(1+\gamma^5)\nu^\lambda) + (\bar{d}^\kappa_j C^\dagger_{\lambda\kappa}\gamma^\mu(1 + \\
&\gamma^5)u^\lambda_j)] + \tfrac{ig}{2\sqrt{2}}\tfrac{m^\lambda_e}{M}[-\phi^+(\bar{\nu}^\lambda(1-\gamma^5)e^\lambda) + \phi^-(\bar{e}^\lambda(1+\gamma^5)\nu^\lambda)] - \\
&\tfrac{g}{2}\tfrac{m^\lambda_e}{M}[H(\bar{e}^\lambda e^\lambda) + i\phi^0(\bar{e}^\lambda\gamma^5 e^\lambda)] + \tfrac{ig}{2M\sqrt{2}}\phi^+[-m^\kappa_d(\bar{u}^\lambda_j C_{\lambda\kappa}(1-\gamma^5)d^\kappa_j) + \\
&m^\lambda_u(\bar{u}^\lambda_j C_{\lambda\kappa}(1+\gamma^5)d^\kappa_j] + \tfrac{ig}{2M\sqrt{2}}\phi^-[m^\lambda_d(\bar{d}^\lambda_j C^\dagger_{\lambda\kappa}(1+\gamma^5)u^\kappa_j) - m^\kappa_u(\bar{d}^\lambda_j C^\dagger_{\lambda\kappa}(1- \\
&\gamma^5)u^\kappa_j] - \tfrac{g}{2}\tfrac{m^\lambda_u}{M}H(\bar{u}^\lambda_j u^\lambda_j) - \tfrac{g}{2}\tfrac{m^\lambda_d}{M}H(\bar{d}^\lambda_j d^\lambda_j) + \tfrac{ig}{2}\tfrac{m^\lambda_u}{M}\phi^0(\bar{u}^\lambda_j\gamma^5 u^\lambda_j) - \\
&\tfrac{ig}{2}\tfrac{m^\lambda_d}{M}\phi^0(\bar{d}^\lambda_j\gamma^5 d^\lambda_j) + \bar{X}^+(\partial^2 - M^2)X^+ + \bar{X}^-(\partial^2 - M^2)X^- + \bar{X}^0(\partial^2 - \\
&\tfrac{M^2}{c_w^2})X^0 + \bar{Y}\partial^2 Y + igc_w W^+_\mu(\partial_\mu\bar{X}^0 X^- - \partial_\mu\bar{X}^+ X^0) + igs_w W^+_\mu(\partial_\mu\bar{Y}X^- - \\
&\partial_\mu\bar{X}^+ Y) + igc_w W^-_\mu(\partial_\mu\bar{X}^- X^0 - \partial_\mu\bar{X}^0 X^+) + igs_w W^-_\mu(\partial_\mu\bar{X}^- Y - \\
&\partial_\mu\bar{Y}X^+) + igc_w Z^0_\mu(\partial_\mu\bar{X}^+ X^+ - \partial_\mu\bar{X}^- X^-) + igs_w A_\mu(\partial_\mu\bar{X}^+ X^+ - \\
&\partial_\mu\bar{X}^- X^-) - \tfrac{1}{2}gM[\bar{X}^+ X^+ H + \bar{X}^- X^- H + \tfrac{1}{c_w^2}\bar{X}^0 X^0 H] + \\
&\tfrac{1-2c_w^2}{2c_w} igM[\bar{X}^+ X^0 \phi^+ - \bar{X}^- X^0 \phi^-] + \tfrac{1}{2c_w} igM[\bar{X}^0 X^- \phi^+ - \bar{X}^0 X^+ \phi^-] + \\
&igMs_w[\bar{X}^0 X^- \phi^+ - \bar{X}^0 X^+ \phi^-] + \tfrac{1}{2}igM[\bar{X}^+ X^+ \phi^0 - \bar{X}^- X^- \phi^0].
\end{aligned}
$$

FIGURE 2.4: The SM Lagrangian in incredible detail [28].

Thankfully, this long equation can be summarized and compacted into an equation that can fit on a mug (see Figure 2.5). The first line of the mug describes the properties of each boson in the SM except the Higgs boson. This term not only formulates the existence of each boson but also describes how each boson interacts with itself and each other. The second line has two terms: the first term describes how the bosons (excluding the Higgs) interacts with both fermions

and anti-fermions (see Figure 2.3 for some examples) while the second term is the hermitian conjugate of the first term and is used to cancel-out the complex-values which come out of the first term to keep the Lagrangian real-valued. The third line, similarly to the second, also has two terms: the first term describes how the Higgs boson interacts with fermions while the second term, being the hermitian conjugate of the first term, describes the anti-fermion interaction. The first term in the last line describes the interaction between the weak interacting bosons (W and Z) and the Higgs boson whereas the last term in the last line describes the potential of the Higgs field (and the spontaneous symmetry breaking thereof) as well as how the Higgs boson interacts with itself.

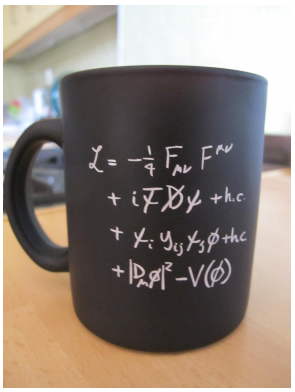

FIGURE 2.5: The SM Lagrangian extremely compressed to fit on a mug [29].

2.1.5 Vacuum Stability of the Standard Model

The SM is a gauge theory which involves quantum fields. These quantum fields can be in various configurations (also known as states), and one, or potentially more, of these states can be in a configuration of minimal energy. These minimal energy states are called vacuum states and these states can either be described as stable, unstable or meta-stable. If the state resides within a global minimum of energy, it is deemed stable. Unstable states are states within a local minimum which can decay into the global minimum by passing through the potential barrier (through a process known as quantum tunneling) which exists between the local and global minima. Meta-stable states, however reside within a local minimum which cannot decay into the global minimum before the end of the Universe due to the tunneling probability being so small that the expected decay time far exceeds the expected lifetime of the Universe [30].

To determine the vacuum stability of the SM, the effective potential of the SM needs to be examined. There are two ways to examine the effective potential, i.e. perturbatively or non-perturbatively. However, in the non-perturbative case, the top quark and Higgs interactions become so strong that the probabilities exceed 1 and therefore, the effective potential can only be computed perturbatively. After extensive calculations up to the next-to-next-to leading order of the effective potential in the perturbative regime (see [8, 14] and the references therein), the

stability regions (as well as the non-perturbative region) are shown in a phase diagram in the top mass-Higgs mass plane, which can be seen in Figure 2.6. The vacuum stability of the SM is found to be within the meta-stable region [8, 14]. However, due to the fact that the stability of the SM appears to be on the border between the stable and meta-stable region within the phase diagram, more precise measurements of the top mass and Higgs mass could put the vacuum stability within the stable region.

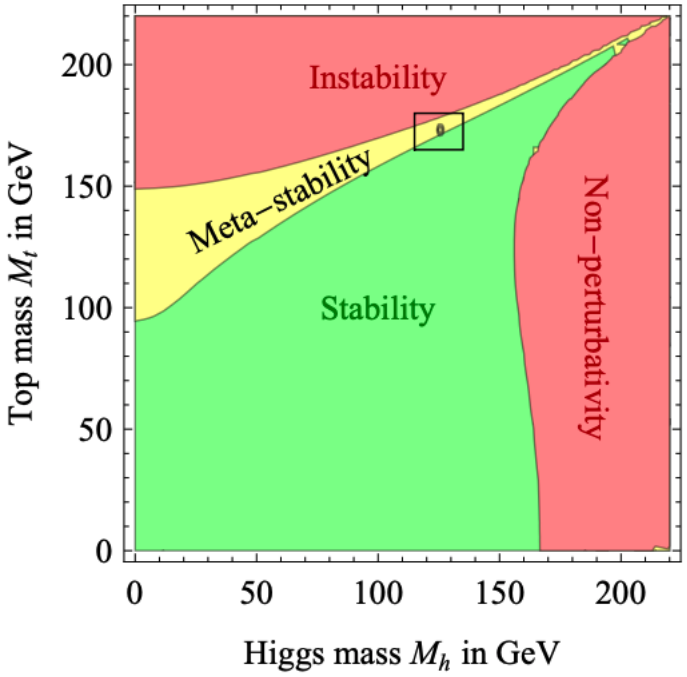

FIGURE 2.6: Regions of absolute stability, meta-stability and instability of the SM vacuum in the top mass-Higgs mass plane. The black dot shows the current state of the vacuum of the SM [8].

2.1.6 Particle Decays in the Standard Model

Most of the particles within the SM decay due to very short lifetimes but there are a few stable and long-lived particles. For any particle to decay, the decay process must be allowed via one of the SM interaction vertices (see Figure 2.3 for some examples) and must have a lower total rest mass.

Most quarks have a long enough lifetime to interact with the strong force. In QCD, colour charged particles (such as quarks and gluons) cannot be found isolated in nature (known as colour confinement). Due to colour confinement, quarks and gluons can only be found in colourless bound states known as hadrons. There are three types of hadrons: mesons which consist of a quark and an antiquark, baryons which consist of three quarks, and antibaryons which consist of three antiquarks. In high energy physics, hadrons are produced through the combination the

quarks and antiquarks which are spontaneously created from the vacuum. This combination of quarks and anti-quarks is known as hadronisation.

2.2 Top Quark

The top quark is the heaviest quark within the SM with a direct measurement mass of 173.0 $\pm$ 0.4 GeV [13]. The mass of the second heaviest quark, the bottom quark (or b quark), which has a mass of $4.18^{+0.04}_{-0.03}$ GeV [13], is forty times less than that of the top mass. Due to the very large mass of the top quark, it has an extremely short lifetime of 10^{-25} s [13]. This timescale is shorter than the timescale needed for it to form hadrons ($\mathcal{O}(10^{-24}$ s) [22]) and therefore, the top quark will decay before it hadronises. Thus, the top quark can only be experimentally studied through its decay products.

The top quark will almost solely ($\sim$ 100 %) decay into a W boson and a b quark [13] according to the SM. The W boson can decay either leptonically (into either a muon, an electron or a tau lepton) or hadronically (into quarks) which occurs 33 % and 67 % of the time, respectively [13]. The b quark has a longer lifetime and will undergo hadronisation before decaying.

2.2.1 Physical processes of the top quark

Since the top quark is the heaviest fundamental particle in the SM, very high energies are needed to produce top quarks. The production of top quarks can be broken down into two main processes: top and anti-top quark pair production ($t\bar{t}$) and single-top production.

2.2.1.1 Single-top

According to the allowed vertices in the SM, there are three most abundant ways to produce a single top quark, i.e. via a weak interaction with a W boson (t- or s-channel) or in associated production with a W boson [13][31][32].

- t-channel:
  This process occurs with an initial b quark interacting with a different flavour quark (denoted q' in the following diagram) via a W boson. This interaction produces a quark (denoted q) and a top quark.

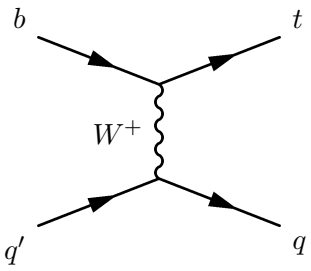

FIGURE 2.7: Single top t-channel production process where a top quark is produced along with a d, s or b quark.

- s-channel:
  This process occurs with an initial anti-quark (denoted $\bar{q}'$) annihilating with a different flavour quark (denoted q) via a W boson. In order to produce a top quark, the W boson decays into a top and and anti-b quark.

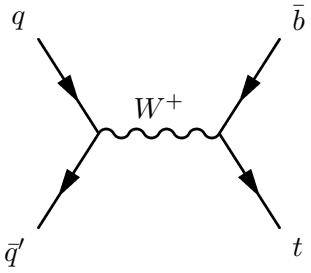

FIGURE 2.8: Single top s-channel production process where a top quark is produced along with an anti-b quark.

- W+top quark associated production:
  This process occurs with an initial gluon either being absorbed by a b quark or interacting with a b quark via a top quark. This interaction produces a W boson and a top quark.

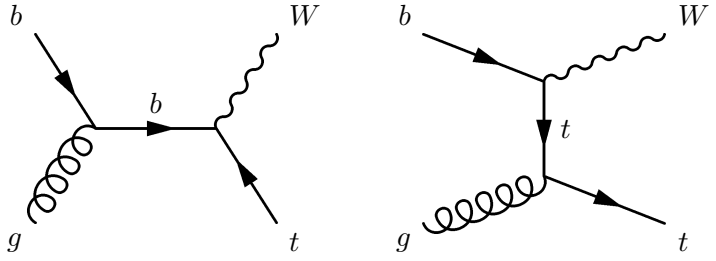

FIGURE 2.9: W+top quark associated production process where a top quark is produced along with a W boson.

2.2.1.2 Top quark pair production

There are two most abundant ways to produce a top and an anti-top quark pair, i.e. via gluon-gluon fusion or quark annihilation [13][32].

- gluon-gluon fusion:

  This process occurs when two gluons interact with each other producing two top quarks.

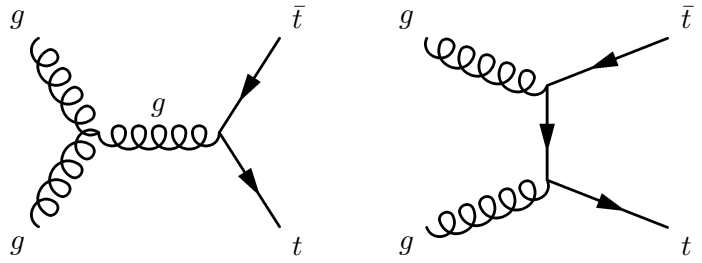

FIGURE 2.10: Top quark pair production where a top and anti-top quark is produced from gluon interactions.

- quark annihilation:

  This process occurs when a quark and its anti-quark annihilate producing a gluon which then produces a top quark pair.

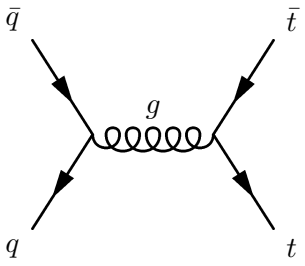

FIGURE 2.11: Top quark pair production where a top and anti-top quark is produced from quarks annihilating.

2.2.2 Definition of the top mass

Quark masses appear as parameters in the SM Lagrangian (see Figure 2.4) and generate mass through their interaction with the Higgs boson. These masses are dependent on the theoretical formalism used to define their existence and therefore will have different values. These theoretical formalisms are called schemes and refer to various renormalizations of the strong interaction term in the SM Lagrangian. The two most well-known renormalization schemes are the modified minimal subtraction ($\overline{\text{MS}}$) scheme and pole scheme [33].

When determining quark masses through the SM Lagrangian, infinities arise in the calculation but these infinities can be removed (absorbed) by introducing additional quantities in the mass and field definitions; this is known as renormalization. Renormalization schemes can describe the behaviour of the quark mass parameters at either short distances or large distances. The pole mass scheme describes the large distance quark mass parameters while the $\overline{\text{MS}}$ describes the short distances [13][4]. These two mass schemes are related by non-perturbative effects and is known up to the third loop correction term (see references [13] and [33] for more information).

The direct mass measurements conducted by the various experiments mentioned in Chapter 1 correspond to the top mass parameter given to the Monte Carlo (MC) generators, often referred to as the Monte Carlo top mass (i.e. m_{top}^{MC}) [4]. The pole mass definition of the top quark derived from direct measurements is generally agreed to be the same as the m_{top}^{MC}. However, these measurements do not correspond to the $\overline{MS}$ mass definition of the top quark but can be converted into the $\overline{MS}$ mass through the relationship mentioned above.

2.2.3 A review on the different top quark mass measurements

From the previous section, there are three different ways to quote the top mass. There is only one way to quote the top mass from direct measurements (i.e. MC mass) but two ways from indirect measurements (i.e. $\overline{MS}$ or pole mass). The world average for each of the different ways to quote the top mass are 173.0±0.4 GeV (MC top mass), 160^{+5}_{-4} GeV ($\overline{MS}$ mass) and 173.1±0.9 GeV (pole mass) [13]. Since this thesis implemented a direct measurement approach, it will only be compared to the MC top mass measurement.

The world average for direct measurements consists of combinations of direct measurements conducted by the Large Hadron Collider and Tevatron collaborations [15–18]. Each of these measurements determined the top mass by either combining the kinematics of a lepton(s) with the kinematics of jets or just from the kinematics of jets (i.e. in the lepton+jets, dilepton+jets and/ or all jets decay modes). These decay modes consist of large amounts of events and therefore, the statistical uncertainties are quite small. The systematic uncertainty in each measurement is always greater than the statistical uncertainty which is due to the reconstruction of jets. This jet uncertainty is the dominant source of systematic uncertainty in each measurement. The leading precision measurement of the top quark mass was done by the CMS collaboration with a value of 172.44±0.13±0.47 GeV, where the jet energy corrections contributed 0.37 GeV to the systematic uncertainty of 0.47 GeV [17].

The statistical uncertainty can only be reduced with more events, but the systematic uncertainty can be reduced by reducing the different systematic dependencies on the mass measurement. The leading source of uncertainty can be reduced by using a less jet-dependent top quark decay mode. One of these decay modes include the lepton+J/ψ decay mode where the J/ψ decays into two oppositely charged muons. This decay mode combines the reconstruction of three leptons to determine the mass of the top quark and therefore, should be largely independent on the jet-dependent uncertainties. Thus, producing a more precise measurement of the top quark.

Chapter 3

CERN and the LHC

3.1 CERN

In 1949, Louis de Broglie put forth a proposal to have a European laboratory and, just two years later, a resolution was made to establish the first European Council for Nuclear Research (otherwise known as CERN) [34]. In 1953, the 12 countries involved in the making of the first draft of the CERN convention, signed the agreement but, it was only in 1954 after the countries involved ratified the convention, was CERN officially born [35].

Since then CERN has grown into 22 official Member States (European countries that contribute financially and are represented on the CERN Council) and has relationships and ties with many other countries from all over the world including South Africa [36]. These other countries have different privileges and duties to the Member States at CERN but are involved and contribute to the world-class research conducted there.

The first foundation for the European laboratory located across the French-Swiss border in Geneva, Switzerland was laid in 1955 [37] and, in 1957, the first accelerator (the Synchrocyclotron) was built at CERN [38]. Since then, many new accelerators and detectors were built at CERN (see Figure 3.1) which kept CERN at the forefront of science and technology for many years. Many inventions and discoveries were made since its inception: the W and Z bosons were discovered in 1983 [39], a mere 6 years later, the World Wide Web (WWW) was invented by a British scientist while working at CERN [40], anti-matter (i.e. anti-hydrogen) was first produced at CERN in 1995 [41], and, more recently, the Higgs boson was discovered in 2012 [42]. The last discovery was made using the largest particle accelerator ever built, the Large Hadron Collider.

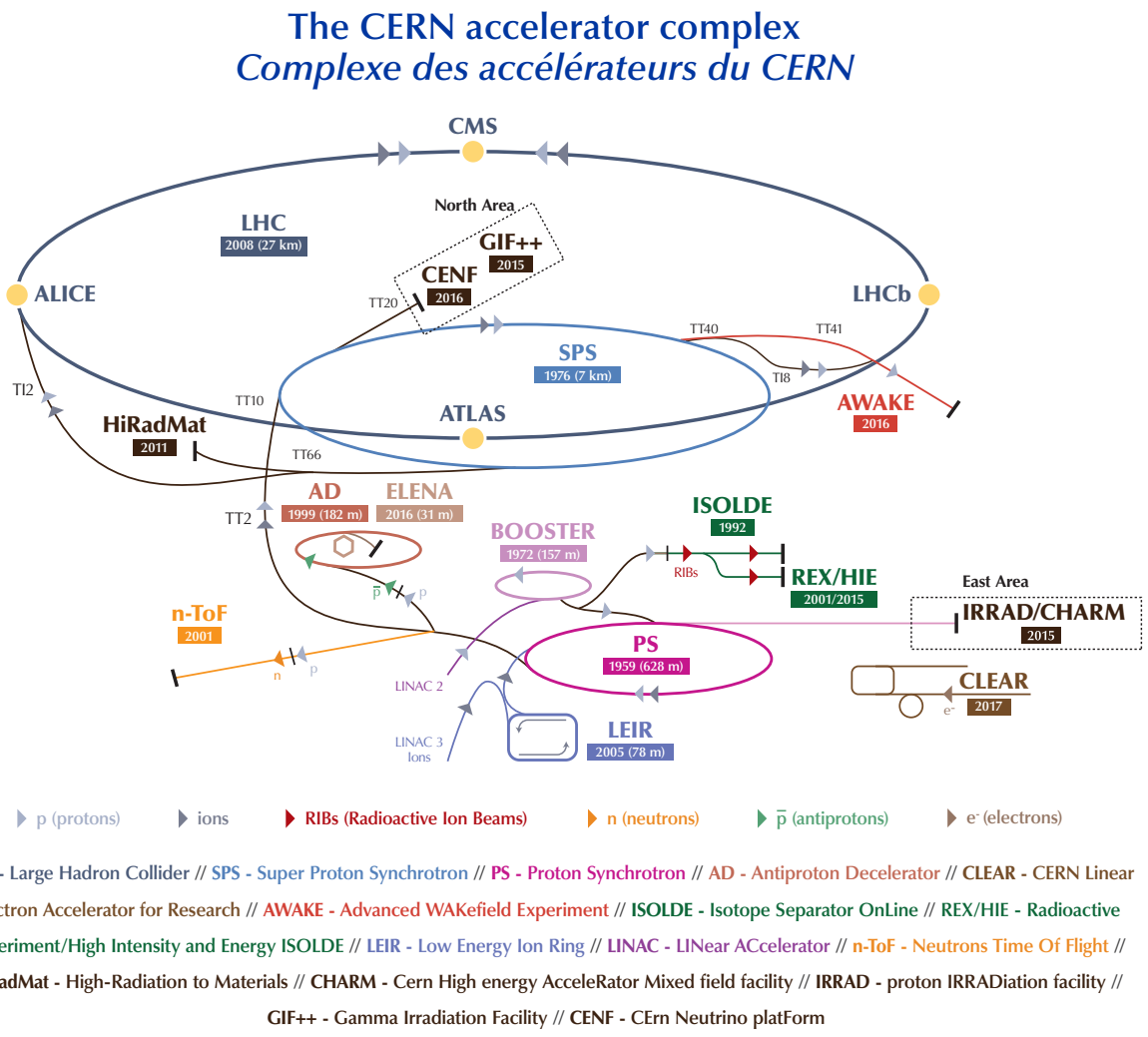

FIGURE 3.1: An illustration showing the accelerator complex at CERN [43].

3.2 The Large Hadron Collider

The Large Hadron Collider (LHC) is the most recent and largest particle collider among the other accelerators at CERN (see Figure 3.1). It's not only the largest but also the most powerful accelerator and collider, not just at CERN, but also in the world.

Before the LHC existed, CERN constructed a 26.7 km tunnel to collide electrons with positrons, called the Large Electron Positron collider (LEP), between 1984 and 1989 [44]. LEP was operational for 11 years resulting in key insight into electroweak interactions which were largely based on experimental evidence and, in the year 2000, the LEP collider reached energies around 208 GeV but was shutdown at the end of the same year to make way for the LHC [45].

The LHC was first approved by the CERN Council in 1994 and was built in the existing LEP tunnel between 1998 and 2008 [44]. The peak performance of the LHC was proposed to be operating at a centre-of-mass energy, $\sqrt{s}$, of 14 TeV with a luminosity of $10^{34}\text{cm}^2\text{s}^{-1}$ [44]. During 2016, 2017 and 2018, the LHC reached (and exceeded) the peak luminosity but only managed operating at $\sqrt{s} = 13$ TeV. At the time of writing, the LHC is currently shutdown and is being upgraded to reach the peak energy of 14 TeV.

The LHC is not the only accelerator responsible for producing such high energies. There are successive accelerators all working together, feeding each other in order to produce and collide protons at extremely high energies (see Figure 3.1). The protons come from a bottle of hydrogen gas after removing the electrons with an electric field. These protons are injected into LINAC2, the first accelerator accelerating protons up to an energy of 50 MeV [46]. After LINAC2, the protons are accelerated to an energy of 450 GeV [46] after travelling through the Proton Synchrotron Booster (PSB), the Proton Synchrotron (PS) and the Super Proton Synchrotron (SPS). The protons are then transferred into two beam pipes in the LHC tunnel and are accelerated to an energy of 6.5 TeV each [46]. After reaching 6.5 TeV of energy, the two proton beams collide at various points along the LHC ring, i.e. at ALICE, ATLAS, CMS and LHCb. Each beam is intended to consist of 2808 bunches with 1.2×10^{11} protons per bunch and will collide 40 million times per second [47]. Data-taking only happens after the proton beams are accelerated to the required energy and then aligned and focused to collide head on; this is also known as stable-beams.

The main objective of the LHC is to study the physics beyond the SM by studying the particles that are produced after high energy proton-proton collisions.

3.2.1 Luminosity

Luminosity is one of the most important values when doing accelerator-based physics and is defined as the number of particles passing through an area per second. There are two different terms used for luminosity, i.e. instantaneous and integrated, and can be calculated using the following equations [48]:

$$\mathscr{L}_{\text{instantaneous}} = \frac{n_b n_1 n_2 f_r}{2\pi \Sigma_x \Sigma_y} \tag{3.1}$$

$$L_{\text{integrated}} = \int_0^T \mathscr{L}_{\text{instantaneous}}(t)dt \tag{3.2}$$

where n_b is the number of bunch crossing per revolution, n_1 and n_2 are the number of protons per bunch, f_r is the LHC revolution frequency and Σ_x and Σ_y are the beam widths in the

transverse plane. Figure 3.2 shows the delivered (which accounts for the luminosity delivered from the start to the end of stable-beams) and recorded (which reflects detector inefficiencies) integrated luminosity by ATLAS in the data-taking period from 2015 to 2018. The luminosity is important as it is used to calculate the cross section (σ), or the probability of particle interaction, of a particular process from the number of events for that particular interaction, i.e. $N_{event} = L_{integrated}\sigma$.

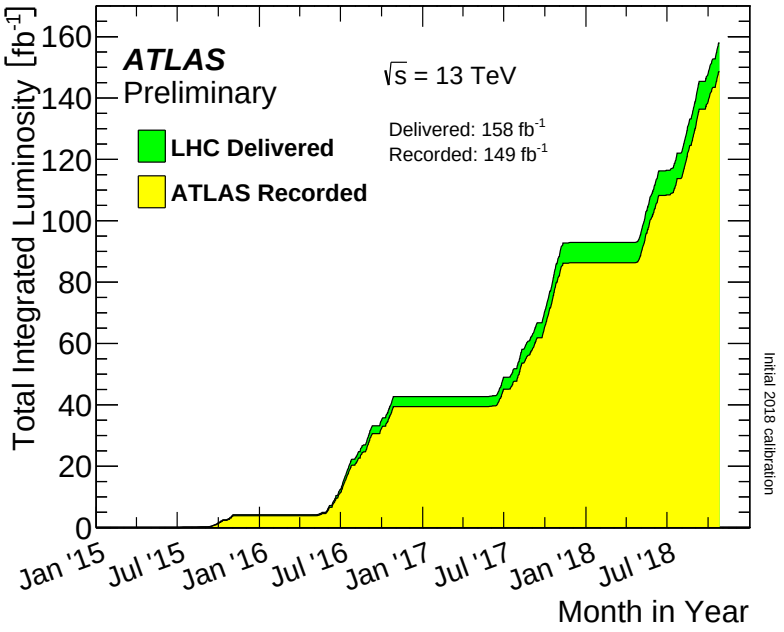

FIGURE 3.2: The cumulative luminosity delivered to ATLAS (green) and recorded by ATLAS (yellow) during stable beams for proton-proton collisions at $\sqrt{s} = 13$ TeV in the LHC during the data-taking period between 2015 and 2018 [49].

Chapter 4

The ATLAS Detector

The following chapter consists of information from "The ATLAS Experiment at the CERN Large Hadron Collider" [50] unless otherwise stated.

4.1 Overview

The ATLAS experiment is designed to take full advantage of the discovery potential of the LHC. ATLAS originally stood for a A Toroidal LHC ApparatuS but is no longer considered an acronym. The discoveries and analyses conducted within ATLAS are done by an international collaboration consisting of around 3000 scientific authors from 181 institutions around the world [51]. The ATLAS collaboration not only involves scientists but also engineers and technicians who together, create the opportunity for success and discovery. A wide variety of studies are conducted within ATLAS to answer fundamental questions about the universe and whether or not there is new physics to explore which goes beyond the SM [52].

The ATLAS detector is cylindrical in shape with a diameter of 25 m and a length of 44 m, and is symmetric in the forward-backward direction about the centre of the detector, which can be seen in Figure 4.1. It is located inside a cavern about 100 m below the ground and weighs a staggering 7000 tonnes [53]. There are many components (or subdetectors) which make up the ATLAS detector but the Magnet system is its largest feature [47]. The magnet system consists of a thin superconducting solenoid surrounding the Inner Detector and three large superconducting toroids, one barrel and two end-caps, arranged azimuthally symmetric around the Calorimeters. The other three major components of the ATLAS detector are the Inner Detector, the Calorimeter and the Muon Spectrometer. The Inner Detector is immersed in a 2 T solenoidal field which is used for momentum resolution, pattern recognition and identification of the collision point while the Calorimeters are used to measure the energy and position of

particles. The Muon Spectrometer surrounds the Calorimeters and is used to measure muon momentum. These subdetectors are integrated with a Trigger and Data Acquisition system and a Computing system which selects physics events with particular properties of interest and stores them for further analysis [53].

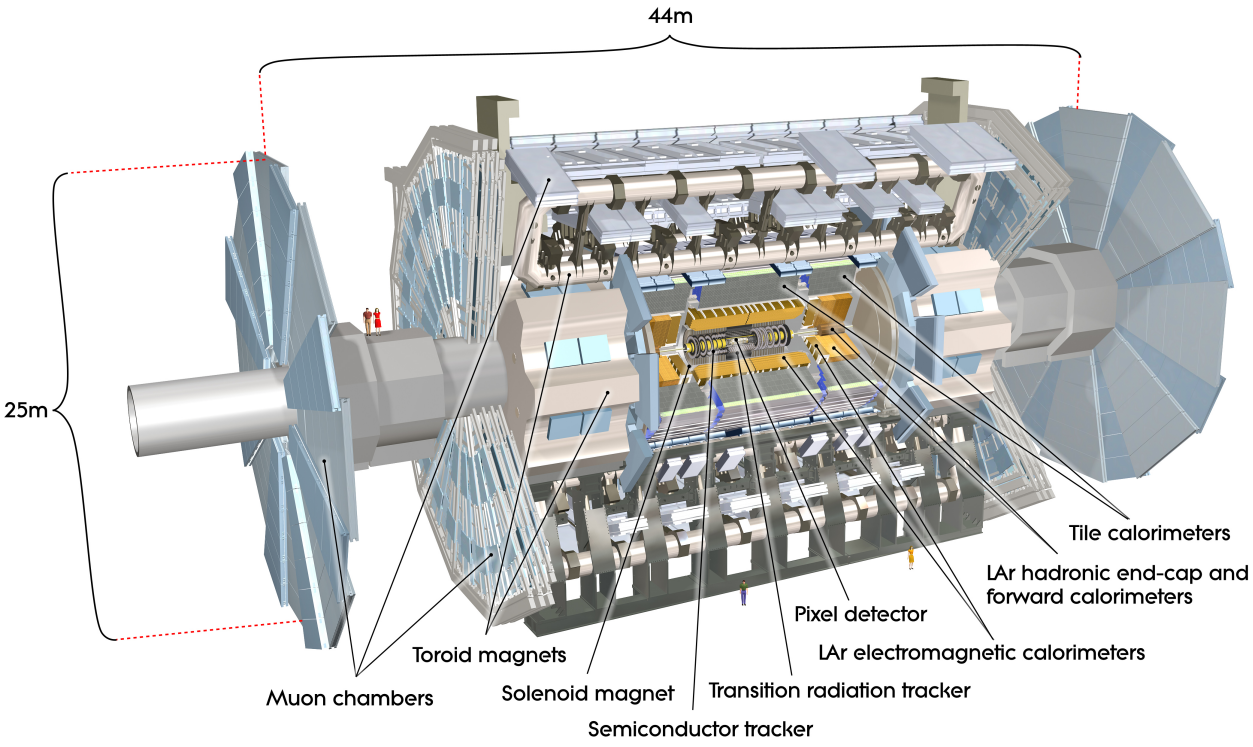

FIGURE 4.1: An illustration showing the ATLAS detector and all its sub-detectors [54].

4.1.1 The Coordinate System

The ATLAS detector uses a right-handed coordinate system where the nominal interaction point is defined as the origin. The z-axis defines the beam direction and x-y plane is therefore, transverse to the beam direction. The positive x-axis points from the interaction point to the centre of the LHC ring while the positive y-axis points upwards. The azimuthal angle ϕ is measured around the beam axis and the polar angle θ is taken as the angle from the beam axis. The polar angle is more commonly replaced with pseudorapidity which is defined as $\eta = -\ln\tan(\theta/2)$. However, when dealing with objects that have a non-negligible mass (such as jets), rapidity is used and defined as

$$y = \frac{1}{2}\ln\left[\frac{E + p_z}{E - p_z}\right]$$

where E is the energy of the object and p_z is the momentum of the object in the z-direction. Rapidity is used due to its difference being Lorentz invariant. Pseudorapidity is, however, preferred as it represents a detector quantity. A spatial quantity ΔR is defined in the η-ϕ space as $\Delta R = \sqrt{\Delta\eta^2 + \Delta\phi^2}$. There are other kinematic quantities which are commonly used and taken from the x-y plane: transverse momentum p_T, transverse energy E_T and missing transverse energy E_T^{miss}.

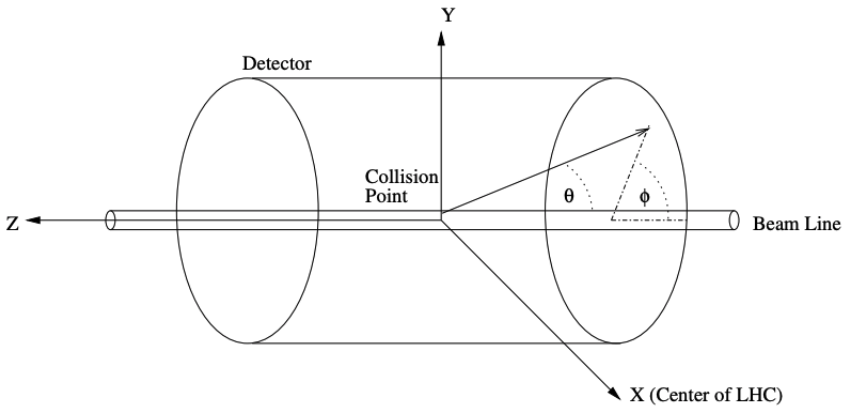

FIGURE 4.2: An illustration of the ATLAS coordinate system [55].

4.2 The Magnet System

The ATLAS detector consists of four large superconducting magnets within the magnet system. This system has a diameter of 22 m and a length of 26 m which stores 1.6 GJ of energy. The Inner Detector is surrounded by a solenoid magnet which provides a 2 T axial magnetic field while the muon detectors are surrounded by three toroid magnets, i.e. one barrel and two end-caps, which produce a toroidal magnetic field of approximately 0.5 T and 1 T, respectively. These magnets bend particles through the subdetectors of the ATLAS detector ensuring their momenta can be measured by the curvature of their trajectories [56].

FIGURE 4.3: The solenoid magnet in the factory after winding the coils [50].

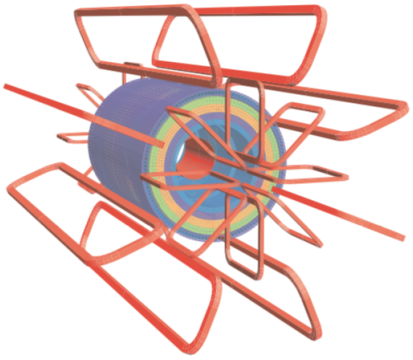

FIGURE 4.4: An illustration showing the geometry of the eight barrel and eight end-cap toroid coils [50].

4.3 Inner Detector

The Inner Detector (ID) surrounds the beam pipe which is immersed in the large superconducting solenoid magnet and is contained within a cylindrical envelope which has a length of 7024 mm and a radius of 2300 mm. It is the first part of the ATLAS detector to see the decay products after the collision. There are three subdetectors within the ID, i.e. the Pixel detector, the Semiconductor Tracker (SCT) and the Transition Radiation Tracker (TRT) (see Figure 4.5), which all work in tandem to identify primary and secondary vertices, track charged particles and measure their momentum. The ID tracks charged particles with a p_T above the nominal threshold of 0.5 GeV that falls within the pseudorapidity range $|\eta| < 2.5$ and also assists in identifying electrons within $|\eta| < 2.0$ with energies between 0.5 GeV and 150 GeV. The pixel detector and the SCT consists of semiconductor technology with high-granularity sensors while the TRT consists of gaseous straw tubes. As the pixel detector is the closest to the beam pipe, it has the highest granularity. During 2013 and 2014, the LHC was shutdown and an extra pixel layer was inserted between the beam pipe and the pixel detector, known as the insertable B-layer (IBL) [57]. The IBL was installed to deal with the higher luminosity between the data taking period of 2015 and 2018.

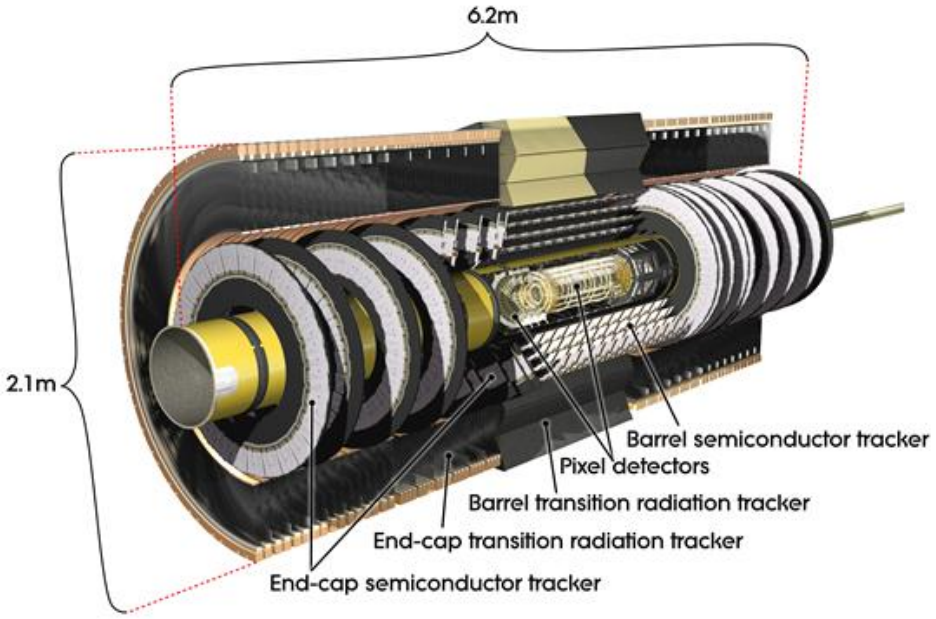

FIGURE 4.5: An illustration of the ATLAS inner detector showing all three subdetectors [58].

4.4 Calorimeters

The Calorimeters are situated between the ID and the Muon Spectrometer and are used to provide energy measurements and identify photons, electrons, jets and missing transverse energy

within $|\eta| < 4.9$. There are three Calorimeters within the ATLAS detector: the Electromagnetic Calorimeter (ECal) which consists of a barrel region and two end-cap regions, the Hadronic Calorimeter (HCal) which consists of a tile barrel region, two tile extended barrel regions and two end-cap regions, and the Forward Calorimeter (FCal). These sub-systems be seen in Figure 4.6. All three Calorimeters consist of absorber materials which causes photons to pair produce and the incoming particle to emit bremsstrahlung radiation in the ECal, or interact via the strong force in the HCal, creating a shower of particles. Additionally, the Calorimeters consist of active materials which measure the energy of the particle showers and therefore the energy of the incoming particle.

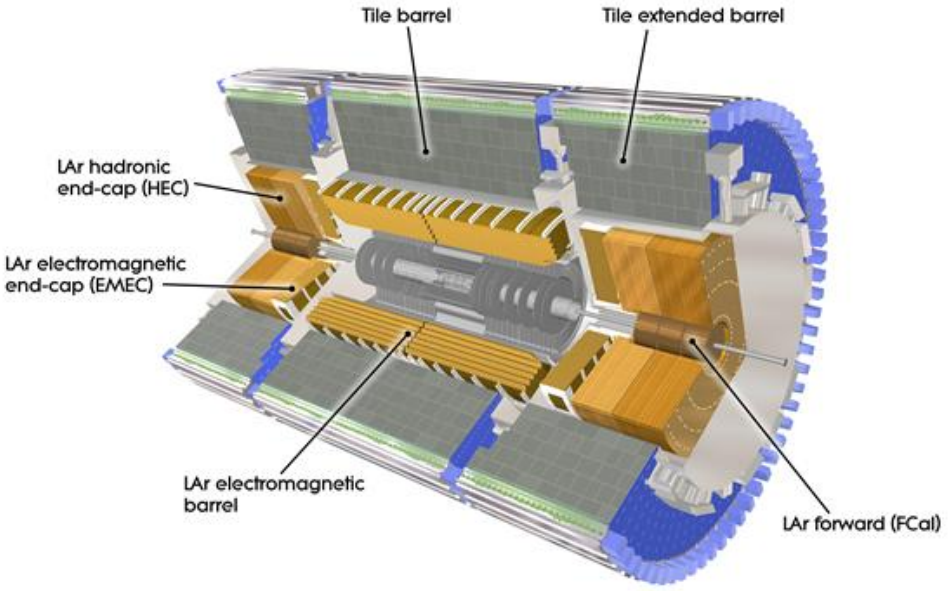

FIGURE 4.6: An illustration of the ATLAS calorimeters showing all three subdetectors [59].

The ECal, HCal end-caps and FCal all use liquid argon (LAr) as the active material which has been chosen for its resistance to radiation and linear response between the incoming and measured energy of the incoming particle. The ECal has fine granularity and is used to measure the energy of electrons and photons. The HCal has coarser granularity and is used to measure energy of jets as well as E_T^{miss}. The FCal aids both the ECal and HCal in their measurements. The HCal is designed to contain hadronic showers while the ECal contains electromagnetic showers, and both are designed to prevent the showers from reaching the Muon Spectrometer. There are very high energy hadrons which are not fully contained in the HCal and therefore, make it all the way to the Muon Spectrometer. These hadrons could be mis-reconstructed as muons.

4.5 Muon Spectrometer

The Muon Spectrometer (MS) is the outermost sub-detector of the ATLAS detector and is primarily used to measure muon momenta. Muons are leptons and therefore, do not interact via the strong force. Furthermore, muons do not lose much energy through bremsstrahlung as it is much heavier than electrons. Thus, muons will usually pass through the Calorimeters depositing small amounts of energy and be the only particles to make it to the MS.

The muon system is designed for precision tracking and object triggering. There are two subsections in the muon system which are responsible for tracking, i.e. Monitored Drift Tube chambers (MDT) and Cathode-Strip Chambers (CSC), and two subsections responsible for triggering, i.e. Resistive Plate Chambers (RPC) and Thin Gap Chambers (TGC). The MDTs and CSCs perform precision momentum measurements within $|\eta| < 2.7$. These two tracking subsections are complemented by the trigger subsections which send track information within nanoseconds after the particle passes through. The RPCs trigger on particles within $|\eta| < 1.05$ (i.e. the barrel region) while the TGCs trigger within $1.05 < |\eta| < 2.4$ (i.e. end-cap region). The trigger chambers are used to supplement the information gained by the tracking chambers in order to produce unambiguous track detection.

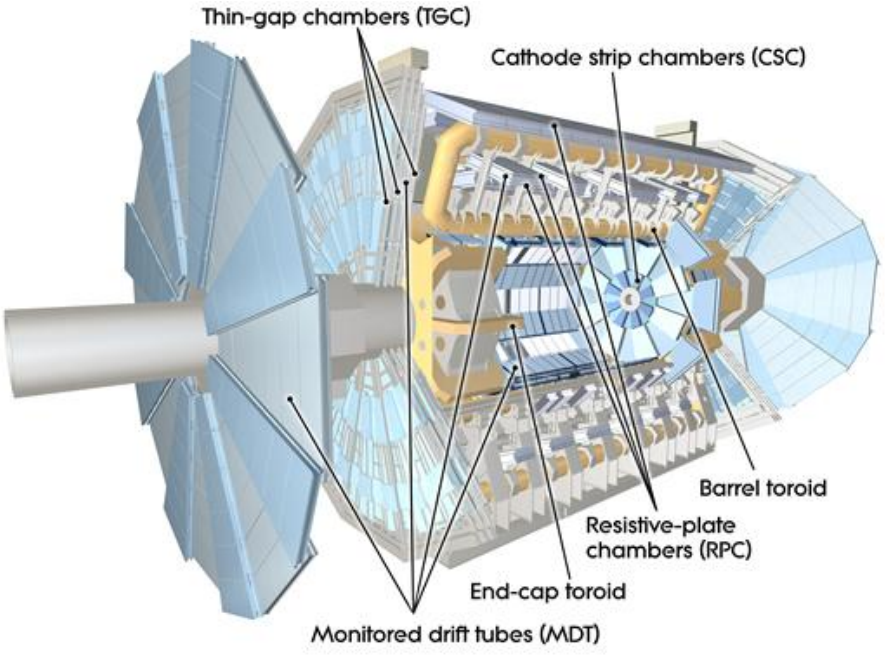

FIGURE 4.7: An illustration of the ATLAS muon subsystem [60].

4.6 Forward Detectors

In addition to the main detectors mentioned previously, there are other smaller detectors near the ATLAS detector in the forward region along the beam pipe (see Figure 4.8). There are two detectors which measure the luminosity delivered to the ATLAS detector, i.e. ALFA (Absolute Luminosity For ATLAS) and LUCID (LUminosity measurement using Cherenkov Integrating Detector) [61, 62]. The last two detectors are the ZDC (Zero-Degree Calorimeter) [63] and the AFP (ATLAS Forward Proton) [64]. The ZDC is used for heavy ion collisions while the AFP studies the energy loss and momentum transfer of very forward protons.

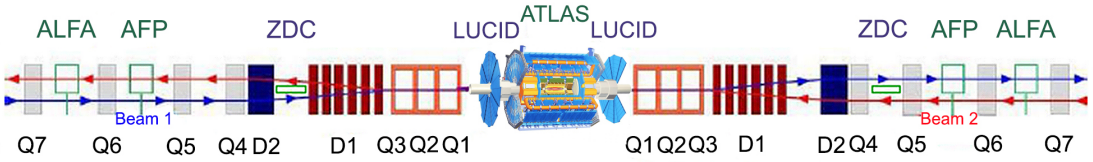

FIGURE 4.8: An illustration of the ATLAS forward detectors [65].

4.7 Trigger and Data Acquisition System

The Trigger and Data AcQuisition (TDAQ) system consists of sub-systems which uses the information collected by the sub-detectors in the ATLAS detector. The ATLAS detector consists of a Level-1 (L1) trigger, which is hardware-based, and a High-Level Trigger (HLT), which is software-based. The L1 trigger selects events with high transverse momentum photons, electrons, jets, muons and τ-leptons decaying into hadrons, as well as events with large total and missing transverse energy. This selection is conducted from the information collected from the RPC and TGC for high p_T muons and from all the Calorimeters sub-systems for the other objects. The HLT uses information from the all the sub-detectors to refine the trigger selections. The DAQ system receives the event information from the sub-detectors at the L1 trigger, buffers it and then moves it to the CERN computing centre for permanent storage. Additionally, DAQ also provides control, monitoring and configuration of the ATLAS detector during data-taking.

4.8 Pile-up

After a collision occurs, the ATLAS detector will trigger on an event with high p_T objects and/or large E_T^{miss} or large total E_T which comes from a single proton-proton collision. However, there are other protons colliding within the bunch crossing, also known as Pile-up. Pile-up can occur in two ways: 1) in-time pile-up, which occurs when additional protons collide within the same bunch crossing, and 2) out-of-time pile-up, which occurs when the debris after previous collision

remains in the sub-detectors. To determine the average amount of pile-up per bunch crossing, a mean value is calculated using the instantaneous luminosity and cross section [48], i.e.

$$\mu = \frac{\mathscr{L}_{\text{instantaneous}}\sigma_{pp}}{n_b f_r} \tag{4.1}$$

where σ_{pp} is the cross section for inelastic proton-proton interactions. The average number of pile-up per bunch crossing over a given period of time is defined as $\langle\mu\rangle$. The average amount of pile-up per bunch crossing as well as the average throughout the various years of data-taking is shown in Figure 4.9.

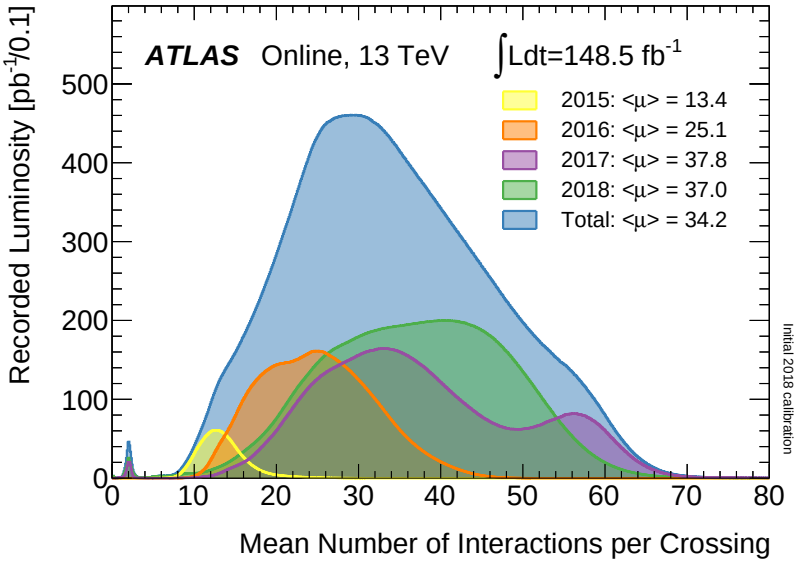

FIGURE 4.9: The recorded luminosity distribution of the mean number of interactions per bunch crossing in proton-proton collisions for the data-taking period of 2015-2018 at $\sqrt{s} = 13$ TeV [49].

Chapter 5

Particle reconstruction and identification within the ATLAS detector

The following chapter consists of information from "The ATLAS Experiment at the CERN Large Hadron Collider" [50] unless otherwise stated.

5.1 Overview

After the proton-proton collision, many different types of particles are produced and interact with the sub-detectors as they traverse the ATLAS detector. The kinematic properties and identity of these particles can only be determined from the information collected by these sub-detectors. Every particle, except neutrinos, will interact with the sub-detectors but only muons will traverse the entire detector. Neutrinos do not interact with the material in the sub-detectors and therefore pass through the ATLAS detector undetected. The ATLAS detector has certain ways of identifying specific particles. All charged particles will leave tracks in the ID but only particles which interact electromagnetically or hadronically will leave showers of particles in the ECal or HCal, respectively. Muons will, however, pass through the ID leaving tracks, pass through the Calorimeter system depositing small amounts of energy and, lastly, leave tracks in the MS. The different types of particles and interactions as seen by the ATLAS detector (i.e. their detector signatures) can be seen in Figure 5.1.

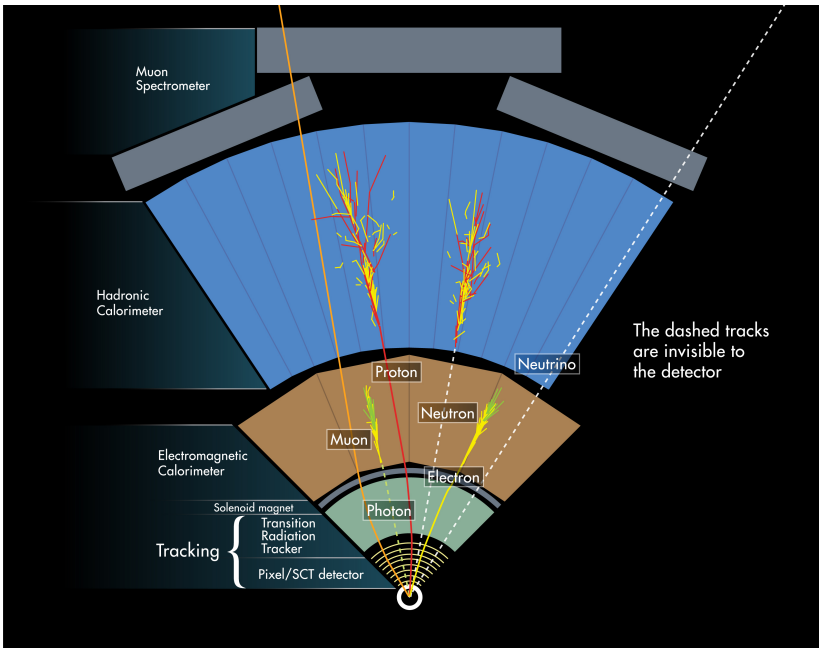

FIGURE 5.1: An illustration showing detector signatures for different particles in the ATLAS detector [66].

5.2 Charged Particles in the Inner Detector

Charged particles leave tracks as they traverse the ID. A track must have a transverse momentum greater than 0.5 GeV over $|\eta| < 2.5$ for it to be reconstructed and the momentum measured. These tracks are reconstructed in three stages: pre-processing, track-finding and post-processing.

The first stage takes the data collected from the pixel and SCT detectors and creates clusters in each layer. The SCT detector consists of double-sided layers and the cluster information on each side is combined into one "cluster", otherwise known as a space-point. The pixel detector, however, consists of single-sided layers and therefore, a space-point is formed from the cluster in each layer. The second stage consists of a wide variety of tracking strategies which cover different applications [67, 68]. These strategies use the high granularity pixel and SCT detectors to detect prompt tracks emerging from the interaction region. Track seeds are formed by combining the space-points in the pixel layers and the first SCT layer which are then extended into the other layers of the SCT detector to form track candidates. After applying several quality cuts on these track candidates, such as the number of clusters and holes per track (where a hole is layer with no associated cluster) and more, outlier clusters are first removed and fake tracks are rejected. The track candidates that pass these quality cuts are fitted and then extended into the TRT. These extended tracks undergo an additional fit which utilizes the information from all the sub-detectors in the ID and then compared to the tracks coming from just the pixel and SCT detectors. However, it is possible to have unused track information in the TRT. These unused track information is extended into the pixel and SCT detectors to

enhance the tracking of secondary vertices coming from decays of particles with longer lifetimes or from photons which have pair-produced. This is called back-tracking. The final stage of track reconstruction is dedicated to reconstructing primary vertices which subsequently reconstructs secondary vertices.

5.3 Electrons and Photons

Electron and photon candidates are reconstructed by combining track data collected in the ID and the shower information in the ECal. The reconstruction algorithm takes the shower information collected in the middle layer of the ECal and uses it to seed electron and photon candidates. A fixed size cluster is identified around the seed and these seed clusters are matched to reconstructed ID tracks. A candidate is identified as a photon if the clusters have no associated tracks in the ID while an electron is identified if the clusters are matched to an associated track. The energy that is deposited by electrons and photons is measured in both the barrel and end-cap regions of the ECal.

Electron candidates are split into three likelihood-based categories: LooseLH, MediumLH and TightLH. These categories are additional quality cuts which are based on the information from the reconstructed tracks, the shape of the showers and on the combined reconstruction information from the ID and ECal. These cuts enhance the signal efficiency and background suppression of identifying electrons with electrons defined in the TightLH category as being predominantly real. Photons are identified if they pass quality cuts similar to those in the TightLH category of electrons, since it is much harder to distinguish photons from background processes. These cuts are also based on shower shapes in the ECal but uses information in the first layer of the ECal (which has very fine granularity) and additional criteria on track isolation to suppress background (see [69] for further information on the identification definitions).

5.4 Muons

Muon candidates traverse and interact with the ID, the Calorimeter system and the MS. The proton-proton collision will produce a wide range of final-state muons. These final-state muons could have originated from J/ψ meson decays (which are usually non-isolated), W or Z boson decays (which are usually isolated), various other SM processes, or even from new physics processes. The ID provides a more accurate measurement of muon momentum in the low to intermediate range while the MS is better suited at the high momentum range (i.e. > 30 GeV). These muons are triggered over $|\eta| < 2.4$.

Similar to the ID, tracks in the MS are also reconstructed in stages. The data collected in each section of the MS are put through algorithms which do pattern-recognition, segment-making and segment-combining, as well as track-fitting. Segments are defined as straight line tracks in a single MDT or CSC chamber. There are four reconstruction strategies implemented by ATLAS to identify muon candidates: i.e. stand-alone, segment-tagged, combined and calorimeter-tagged muons. The stand-alone strategy reconstructs tracks using only data collected in the MS over the MS's acceptance range (i.e. $|\eta| < 2.7$) while the combined strategy combines track data collected by the ID and track data collected in the MS over the ID's acceptance range (i.e. $|\eta| < 2.5$). The segment-tagged strategy combines ID track data with a segment in the MS while the calorimeter-tagged strategy combines ID track data with energy deposits from the Calorimeter system.

Similar to electron candidates, muon candidates are also split into categories: i.e. Loose, Medium, Tight and High-p_T, which are dependent on the type of reconstructed muon as well as the number of holes and clusters in the ID and MS. These quality cuts suppress background, enhance signal efficiency and provide powerful momentum measurements (see [70] for further information on the identification definitions).

5.5 Jets

After the proton-proton collision, quarks and gluons are produced and, due to colour confinement, hadronise. After hadronisation, collimated streams of particles are formed which are known as jets. These jets deposit energy in the Calorimeter system and leave tracks in the ID (only if they are charged) which are then combined in the reconstruction. The ATLAS experiment uses two main ways to reconstruct jets: i.e. using Cone algorithms [71–73] or Sequential clustering algorithms [74–76]. Cone algorithms assume that the stream of particles produce a cone-shape and clusters the cone-shape information to reconstruct jets. Sequential clustering algorithms assume that particles inside the stream have small momentum differences and clusters these particles based on their momenta. However, cone algorithms severely lack precise predictions of jets due to their infrared and collinear unsafety [77]. In this analysis, a specific type of a sequential clustering algorithm called the Anti-K_T algorithm was used to reconstruct jets. This algorithm compares the distance between two clusters in the jet, d_{ij}, with the distance between one of the clusters and the beam, d_{iB}. These two variables are calculated as follows

$$d_{ij} = min\left(\frac{1}{p_{T,i}^2}, \frac{1}{p_{T,j}^2}\right)\frac{\Delta R_{ij}^2}{R^2} \tag{5.1}$$

$$d_{iB} = \frac{1}{p_{T,i}^2} \tag{5.2}$$

where $p_{T,i}$ is the transverse momentum of cluster i, R is the radial parameter used to define the size of the jet (usually between 0.4 and 0.7) and ΔR_{ij} is the distance in the η-ϕ plane between the two clusters. The algorithm first determines all the d_{ij} and d_{iB} values and then selects the minimum between these distances. If d_{iB} is found to be the minimum, cluster i is identified as a complete jet and is no longer considered in the algorithm. However, if d_{ij} is found to be the minimum, the four momenta of clusters i and j are combined and i and j are then identified as one cluster and the individual clusters are no longer considered in the algorithm. The process is reiterated until all the clusters are combined.

5.5.1 b-tagged Jets

Jets could originate from quarks and gluons hadronising. To identify jets arising from b quark hadronisation (also known as b-tagging), the jet must be within $|\eta| < 2.5$ with $p_T > 15$ GeV. When conducting b-tagging, the reconstructed tracks must be within $\Delta R < 0.4$ from the jet axis and have $p_T > 1$ GeV. The hadrons arising from b quark hadronisation (i.e. B-hadrons) have longer lifetimes (∼1.5 ps or 0.45 mm in distance [13]) than other lighter quark-hadrons and therefore will have a delayed decay and form a vertex away from the primary vertex (i.e. a secondary vertex). This is a unique feature of B-hadrons. To determine whether or not these tracks arise close to the primary vertex, impact parameter cuts are applied. There are two impact parameters: i.e. the transverse (d_0) and longitudinal (z_0) parameters. The transverse impact parameter is defined as the shortest path between the primary vertex and the track in the r-ϕ plane while the longitudinal impact parameter is the z-coordinate at this d_0 point. The tracks considered for b-tagging must originate within $|d_0| < 1$ mm and $|z_0 - z_\nu| \sin\theta < 1.5$ mm, where θ is the measured polar angle of the track and z_ν is the reconstructed position of the primary vertex in the z-direction. After reconstructing these tracks, a multivariate algorithm is used to identify the b-tagged signal efficiency and light-jet rejection [78].

5.6 Missing Transverse Energy

Protons just before a collision have momentum almost entirely in the z-direction and thus have negligible transverse momentum. If all the particles produced after the collision are detected, the total transverse momentum should be zero (due to momentum conservation). However, this is not possible as there are some particles (neutrinos and possibly new particles) which traverse the ATLAS detector undetected and thus, their momentum is unknown (i.e. missing).

The missing transverse momentum is determined by adding up the transverse momenta of all reconstructed particles and noting that the total should be zero, i.e. $\vec{p}_{\mathrm{T}}^{\,\mathrm{miss}} = -\sum_i \vec{p}_{\mathrm{T},i}$. However, this also applies to the missing transverse energy which can be calculated in a similar way, i.e.

$$\vec{E}_{\mathrm{T}}^{\,\mathrm{miss}} = -\sum_i \vec{E}_{\mathrm{T},i} \tag{5.3}$$

The energy of the detected particles is measured from the energy deposits in the Calorimeter cells using a global calibration scheme (which can be seen in reference [50]) and from the momentum measurements of muons in the MS. In order to reduce the contribution from fake muons, these muons must have a matched track in the ID. There is, however, energy that is lost between the electromagnetic barrel and tile Calorimeters and this is corrected for by using the same calibration scheme mentioned before.

5.7 Lepton Isolation

Reconstructed leptons could have many other particle tracks and energy deposits in close proximity due to the high density of particles produced after the proton-proton collision. Therefore, in addition to the above criteria used to provide signal efficiency and background suppression when reconstructing leptons, isolation requirements are used. These requirements consist of isolating the track and energy deposits of the reconstructed lepton and is defined through the spatial quantity ΔR.

There are several working points which ATLAS uses to identify the isolation of leptons which either correspond to fixed quality cuts or is dependent on the reconstructed kinematics of the particles around the lepton. A gradient isolation working point was used in this analysis and is described. The track isolation within this working point requires the sum of the $\mathrm{p_T}$ of the tracks around the lepton (excluding the reconstructed lepton track) to be within a ΔR = (10 GeV/sum of $\mathrm{p_T}$) $\leq$ 0.2 but the individual tracks must be within the ID coverage with a $\mathrm{p_T}$ > 1 GeV and originate from the primary vertex. The calorimeter isolation within this working point requires the sum of the energy deposits around the lepton (excluding the lepton energy deposits) to be within a ΔR = (sum of energy/$\mathrm{p_T}$) < 0.2. Both the track and calorimeter requirements provide an efficiency of 90 % and 99 % if the lepton has a $\mathrm{p_T}$ of 25 GeV and 60 GeV, respectively [69][70].

Chapter 6

Analysis

The top quark almost exclusively decays into a W boson and a b quark according to the SM (see Section 2.2) and therefore, events involving a $t\bar{t}$ pair will almost exclusively consist of two W bosons and two b quarks. Events involving the s-channel single top quark process will almost exclusively consist of two b quarks and a W boson. However, the single top events involving the t-channel and W+top quark associated production will consist of two b quarks and a W boson if the top quark is produced along with a b quark in the t-channel and the W boson decays into a b quark in the W+top quark associated production. This analysis searched for events consisting of a W boson which decayed leptonically into either an electron or a muon and its corresponding lepton neutrino, and at least two b quarks where one of the b quarks hadronised and the B-hadron decayed into a J/ψ meson and the J/ψ meson decayed into two oppositely charged muons. The top quark decay mode of interest is represented in Equation 6.1, i.e.

$$t \rightarrow W(\rightarrow l\nu)b(\rightarrow J/\psi[\rightarrow \mu^{+}\mu^{-}] + X) \tag{6.1}$$

The final state particles in this lepton+jets(b-tagged)+J/ψ channel can be found in many different SM processes. Therefore, in order to characterize the backgrounds associated within this channel, the theoretical predictions of signal and background had to be taken into account. There are also backgrounds which could have come from jets mis-reconstructed as leptons (known as Fake Leptons, FL) or from leptons produced in jets which leave tracks in the detector (known as Non-Prompt leptons, NP). Additionally, even more reconstruction backgrounds exist within this channel which come from J/ψ mesons originating directly from the proton-proton collision or not from top quark B-hadron decays.

The top quark mass is correlated with its decay products and therefore, can be determined from the invariant mass distribution of the lepton originating from the W boson decay and the J/ψ meson originating from the B-hadron decay through a maximum likelihood method. This

project involved estimating each background contribution and the impact these backgrounds have on the overall statistical uncertainty on the top mass measurement.

6.1 Data and Simulation

The analysis was performed using proton-proton collision data collected by the ATLAS detector in 2015 and 2016 at $\sqrt{s} = 13$ TeV corresponding to a total integrated luminosity of 36.1 fb^{-1}. The data collected required all sub-detectors to be operational and stable beam conditions to be met. In addition, each selected event also contains pile-up data.

Simulated events were used to develop the analysis and compared to data in order to assess and estimate the signal and background contributions. These simulated events come from MC generators which simulate proton-proton collisions, particle interaction and their kinematic properties. These generator outputs are then processed through detector simulations. Each MC simulation is designed to generate and simulate specific SM processes (also called MC simulated samples or simply MC samples). The EvtGen [79] generator was used to model the decays of b- and c-flavoured hadrons in all MC samples. This analysis targeted top quark production and therefore, both the top quark pair production and single top quark production processes will produce signal final state particles. The $t\bar{t}$ and three single top quark MC samples were generated using Powheg-Box [80] and the parton showering, hadronisation and underlying event were simulated using Pythia6 [81] with Perugia 2012 tunable parameters [82]. All four of these top quark samples utilized a set top quark mass of 172.5 GeV in the simulations. There are SM processes which produce the same final state particles within this lepton+jets(b-tagged)+J/ψ channel other than top quark production processes, known as background processes. These backgrounds could originate from W+jets, Z+jets and various diboson processes (i.e. WW, WZ and ZZ). The W+jets and Z+jets MC samples were generated using Madgraph5 aMC@NLO [83] and the parton showering, hadronisation and underlying event were simulated using Pythia8 [84] with the A14 tune [85] and NNPDF23LO parton distribution function set [86]. The various diboson samples were generated and the parton showering, hadronisation and underlying event were simulated using Sherpa (v2.1.1) [87] with the CT10 parton distribution function set [88]. The W+jets MC sample, however, does not account for double parton interactions, i.e. a W boson produced from one parton interaction and a J/ψ meson produced from another. This double parton scattering (DPS) process has already been measured by ATLAS [89]. The DPS process could produce the same final state particles within this lepton+jets(b-tagged)+J/ψ channel and, therefore contribute to the background in this channel. This DPS contribution was determined and described under Section 6.6.4.

Each MC generator output was processed through the full ATLAS detector simulation [90] designed using GEANT4 [91]. Additional proton-proton collisions were generated using Pythia8

[84] and used to simulate the effect of pile-up. The effect of pile-up was corrected for in the MC simulations to match the average number of interactions per bunch crossing observed in data. Since each MC sample was produced with a large number of events, the number of events in the corresponding process in data will not match. Therefore, they need to be normalized to the integrated luminosity of the data samples in order to make an accurate comparison. Both data and MC samples implemented the same algorithms and quality cuts to reconstruct particles. Detector corrections derived from dedicated data samples are also applied to the MC samples in order to improve the agreement with data (see references [69] and [70] for more information on the performances of the ATLAS detector).

6.2 Preselection

Both the data and the MC samples underwent a preselection process which reduced the amount of events to analyze and selected events tailored to the decay mode of interest. These events had to consist of two oppositely charged muons where the tracks of these muons were fitted to a common vertex and the invariant mass of the common vertex had to be within 2-3.6 GeV, corresponding to a J/ψ particle. Additionally, the preselection process stores the fitted common vertex kinematic properties and, furthermore, removes events with no muons or electrons with a $p_T > 20$ GeV within $|\eta| < 2.5$ and where the sum of the number of reconstructed muons and electrons is less than 3.

To ensure the selected events corresponded to good collision data, the following selection criteria has been applied:

Events were required to consist of at least one electron or muon with a p_T greater than the minimum p_T trigger threshold at the HLT level. The minimum trigger threshold required electrons (muons) to at least have a $p_T > 24$ (20) GeV and 26 (26) GeV in 2015 and 2016, respectively. The minimum trigger had an identification requirement (i.e. "loose or medium" for muons and "medium or tight" for electrons) which reduces the efficiency at much higher lepton p_T than the minimum threshold and therefore, additional triggers with higher p_T thresholds with either a looser or no identification requirements were included (see Table 6.1). These p_T trigger thresholds can be seen in Table 6.1 where the minimum p_T is adjacent to either "mu" (for the muon triggers) or "e" (for the electron triggers). The additional "L1MU15" ("L1EM20VH") criteria required the muons (electrons) which were triggered at the HLT level to first have had a $p_T > 15$ (20) GeV at the L1 trigger level. The "nod0" criteria within the electron triggers represents no transverse impact parameter, d0, requirements. Events were rejected if jets arose from noise bursts in the ECal or if jet timing was incompatible with the event time. The primary vertex was defined as the first vertex which had at least four associated tracks with $p_T > 400$ MeV.

Period	Muon Triggers	Electron Triggers
2015	HLT_mu20_iloose_L1MU15 HLT_mu50	HLT_e24_lhmedium_L1EM20VH HLT_e60_lhmedium HLT_e120_lhloose
2016	HLT_mu26_ivarmedium HLT_mu50	HLT_e26_lhtight_nod0_ivarloose HLT_e60_lhmedium_nod0 HLT_e140_lhloose_nod0

TABLE 6.1: Different single electron and muon triggers used in each data period.

6.3 Experimental Signature

The experimental signature involved final state particles from the decay mode of interest shown in Equation 6.1. The selected events consisted of exactly one electron or muon with a minimum $p_T > 25$ (27) GeV in 2015 (2016) which fired one of the single lepton triggers in Table 6.1, at least two b-tagged jets, $E_T^{miss} > 20$ GeV (to account for the neutrino from the W boson decay) and an oppositely charged muon pair with an invariant mass around the mass of the J/ψ, i.e. within 2 and 3.6 GeV (as $m_{J/\psi} = 3096.900 \pm 0.006$ MeV [13]). Additionally, the W boson transverse mass was calculated by combining the electron or muon candidate properties with the neutrino properties (represented by E_T^{miss}), using $m_T(\text{lepton},E_T^{miss}) = \sqrt{2p_T(\text{lepton})E_T^{miss}(1-\cos(\phi(\text{lepton})-\phi(E_T^{miss})))}$. This transverse mass of the W boson quantity improves the selection of real W bosons and therefore, an additional selection cut of $m_T(\text{lepton},E_T^{miss}) > 40$ GeV was applied. This experimental signature is also known as the signal region.

6.3.1 W boson: Electrons

Electron candidates were required to pass a tight-likelihood based selection criteria (which minimizes electrons reconstructed from photons pair-producing and suppresses hadrons identified as electrons), be found within the coverage of the ID, must have originated from the primary vertex, be isolated and have fired one of the electron triggers. Each electron candidate that fired one of the electron triggers in Table 6.1 must have had a minimum p_T of 25 (27) GeV using the triggers in 2015 (2016) or if the trigger threshold is greater 25 (27) GeV then the electron candidate must have had a minimum p_T at least 1 GeV greater than the threshold to reduce inefficient triggering.

Selection	Criteria
Reconstruction	TightLH
Isolation	Gradient
Transverse Momentum	$p_T > 25$ (27) GeV in 2015 (2016)
Pseudorapidity	$\|\eta\| < 2.5$
Longitudinal impact parameter significance	$\|\Delta z_0 \sin\theta\| < 0.5$ mm
Transverse impact parameter significance	$\|d_0\| < 5\sigma_{d_0}$

TABLE 6.2: Electron candidates passing the above criteria were considered signal electrons.

Each event with an electron candidate which passed all of the selection criteria in Table 6.2 must not contain a muon candidate with $p_T > 25$ GeV and $|\eta| < 2.5$ to ensure only one of the W bosons decayed leptonically.

6.3.2 W boson: Muons

Muon candidates were required to pass a medium based selection criteria (which minimizes the uncertainty in muon reconstruction and suppresses hadrons being identified as muons), be identified as a combined muon, be found within the coverage of the ID, must have originated from the primary vertex, be isolated and have fired one of the muon triggers. Each muon candidate that fired one of the muon triggers in Table 6.1 must have had a minimum p_T of 25 (27) GeV using the triggers in 2015 (2016) or if the trigger threshold is greater 25 (27) GeV then the muon candidate must have had a minimum p_T at least 1 GeV greater than the threshold to reduce inefficient triggering.

Selection	Criteria
Identification	Combined
Reconstruction	Medium
Isolation	Gradient
Transverse Momentum	$p_T > 25$ (27) GeV in 2015 (2016)
Pseudorapidity	$\|\eta\| < 2.5$
Longitudinal impact parameter significance	$\|\Delta z_0 \sin\theta\| < 0.5$ mm
Transverse impact parameter significance	$\|d_0\| < 3\sigma_{d_0}$

TABLE 6.3: Muon candidates passing the above criteria were considered signal muons.

Each event with a muon candidate which passed all of the selection criteria in Table 6.3 must not contain an electron candidate with $p_T > 25$ GeV and $|\eta| < 2.5$ to ensure only one of the W bosons decayed leptonically.

6.3.3 B-tagged jets

Jet candidates must have had a minimum $p_T > 40$ GeV and be found within the coverage of the ID (i.e. $|\eta| < 2.5$). These jets also had to be b-tagged which meant the multivariate algorithm must have produced a weight larger than 0.64 which corresponds to a 77 % b-tagging efficiency in $t\bar{t}$ events [92].

6.3.4 J/ψ: Muons

The muon candidates which decayed from the J/ψ meson must have had a track associated to a dimuon vertex, been reconstructed as either combined or segment-tagged muons, be found within the coverage of the ID (i.e. $|\eta| < 2.5$) and have had a minimum $p_T > 3.5$ GeV if $|\eta| < 1.3$ or $p_T > 2.5$ GeV if $|\eta| > 1.3$. If one of these muon candidates were reconstructed as the muon from the W boson, the event was rejected. If there were more than two muon tracks associated to the same dimuon vertex, the event was rejected. The muon candidate from the W boson and an oppositely charged muon candidate from the J/ψ decay was combined and, if the invariant mass of the combination was found to be within 81 GeV and 101 GeV, the events were rejected. This was to ensure the selected muons did not originate from a Z boson decay. The dimuon pair must have been oppositely charged with a post-vertexing invariant mass between 2 GeV and 3.6 GeV, $p_T > 8.5$ GeV and be found within a rapidity range of $|y| < 2.1$ to ensure high acceptance and efficiency of J/ψ candidates.

6.4 Non-prompt and Fake Lepton Background

6.4.1 Overview

Detector acceptance, quality cuts and isolation requirements were used to search for events containing top quarks. These experimental signatures more often than not involved the selection of one or more charged leptons which came from the decay of W bosons and these leptons are called prompt or real leptons.

However, due to the imperfect algorithms and detector signatures, non-prompt and fake leptons can be mis-reconstructed as prompt leptons. Non-prompt electrons and muons can arise from b and c quarks hadronising and the B- and C-hadrons decaying into leptons. Fake electrons can arise from photons pair-producing or from jets depositing large amounts of energy in the ECal. Fake muons, however, can arise from particles which emerge from highly energetic hadronic showers which leave tracks in the MS. These backgrounds emanate from multi-jet events in the

single lepton event selection and are dominated by W+jets and semi-leptonic $t\bar{t}$ events when selecting events with two leptons.

The top quark analysis groups within the ATLAS experiment have estimated the background contribution from non-prompt or fake leptons in 2014, which corresponded to the data-taking period of 2012, using a matrix method data-driven technique [20]. However, these backgrounds were determined for the lepton + jets, dilepton + jets and/ or all jets channels without any selection criteria on J/ψ mesons. Additionally, the data and MC samples used in reference [20] went through a different preselection process than the one described under Section 6.2. This different preselection process stored events which consisted of at least one electron (muon) with a $p_T > 20$ GeV within $|\eta| < 2.5$ (2.7). Every other event was removed and there was no track refitting to a common vertex done within this different preselection process. To ensure the selected events corresponded to good collision data, the same selection criteria described under Section 6.2 was used.

Selection	Top quark analysis group preselection	This analysis' preselection
Number of electrons (muons) per event	at least 1 (1)	at least 1 (1)
Electron (Muon) Transverse momentum	$p_T > 20$ (20) GeV	$p_T > 20$ (20) GeV
Electron (Muon) Pseudorapidity	$\|\eta\| < 2.5$ (2.7)	$\|\eta\| < 2.5$ (2.5)
Track Fitting to a common vertex	Not done	Yes
Invariant mass of common vertex	Not done	2-3.6 GeV
Sum of electrons and muons	Not done	at least 3

TABLE 6.4: Different preselection processes before selecting good collision data.

From Table 6.4, the two preselection processes are very different and therefore the events analyzed to determine the non-prompt or fake lepton backgrounds are different. This could bring about different non-prompt or fake lepton background contributions and thus, this background needs to be determined using this analysis' preselection process (Section 6.2). This analysis' preselection was chosen as it is closely linked to the experimental signature under study. Therefore, by applying the same matrix method data-driven technique as described in reference [20] (and under Section 6.4.4), the non-prompt or fake lepton background contribution was determined using this analysis' preselection process.

6.4.2 Data and Simulation

Due to time constraints, only the proton-proton collision data collected by the ATLAS detector in 2015 at $\sqrt{s} = 13$ TeV which corresponded to an integrated luminosity of 3.2 fb^{-1} were used to determine the non-prompt and fake lepton contribution. The same MC samples mentioned under Section 6.1 were used to perform this analysis (i.e. $t\bar{t}$, single top, W+jets, Z+jets and diboson samples). To ensure the selected events corresponded to good collision data, the same selection criteria has been applied as described under Section 6.2.

6.4.3 Object Selection

For this analysis no further selection criteria was applied to J/ψ candidates but the same selection criteria was applied for the lepton candidates (as described in Tables 6.2 and 6.3) and for b-tagged jets. If the electron (muon) candidates passed the entire selection criteria in Table 6.2 (6.3) then it was considered a "tight" electron (muon). A "loose" electron or muon candidate was defined as a lepton which passed the same selection criteria as the tight leptons except the loose candidates had no isolation requirement and, just for electrons, a relaxed identification type was required, i.e MediumLH.

6.4.4 Matrix Method

The matrix method technique was adopted from reference [20] and is described below.

Since the signal experimental signature contains a single lepton, the number of events with one tight lepton (N^T) and one loose lepton (N^L) can be expressed as a linear combination of the number of events with a real or a non-prompt or fake lepton, i.e.

$$\begin{aligned} \mathrm{N^L} &= \mathrm{N^L_{real}} + \mathrm{N^L_{fake}} \\ \mathrm{N^T} &= \epsilon_{\mathrm{real}}\mathrm{N^L_{real}} + \epsilon_{\mathrm{fake}}\mathrm{N^L_{fake}}, \end{aligned} \tag{6.2}$$

where ϵ_{real} and ϵ_{fake} are the fraction of real leptons in the loose selection which pass the tight selection and the fraction of non-prompt and fake lepton in the loose selection which pass the tight selection, respectively. Since $\mathrm{N^L}$ and $\mathrm{N^T}$ are measurable quantities, the number of events with a non-prompt or fake lepton can therefore be determined from Equation 6.2, if ϵ_{real} and ϵ_{fake} are known. These efficiencies were measured in data in control regions where non-prompt or fake leptons are enhanced. The number of tight non-prompt or fake lepton background events can be determined using Equation 6.3, i.e.

$$\mathrm{N^T_{fake}} = \frac{\epsilon_{\mathrm{fake}}}{\epsilon_{\mathrm{real}} - \epsilon_{\mathrm{fake}}}(\epsilon_{\mathrm{real}}\mathrm{N^L} - \mathrm{N^T}) \tag{6.3}$$

Since both efficiencies depend on the number of loose and tight events, i.e. $\mathrm{N^T}$ and $\mathrm{N^L}$, ϵ_{real} and ϵ_{fake} depend on the event signature and lepton kinematics. The efficiencies were parametrised as a function of the lepton's transverse momentum and pseudorapidity. To account for this non-prompt or fake lepton contribution, an event weight had to be computed and this event weight was computed using Equation 6.4, i.e.

$$w_i = \frac{\epsilon_{\text{fake}}}{\epsilon_{\text{real}} - \epsilon_{\text{fake}}}(\epsilon_{\text{real}} - \delta_i), \tag{6.4}$$

where δ_i equals one if the loose event i passes the tight selection and 0 otherwise. The non-prompt and fake lepton contribution was estimated in each bin of the final observable by the sum of the w_i over all the events in that bin.

6.4.5 Measurement of the real efficiency

The real efficiencies, ϵ_{real}, were measured in control regions enriched in Z boson leptonic decays (i.e. $Z \to ee$ or $\mu\mu$) and jets using a tag-and-probe method. This method selects an unbiased sample of loose leptons from the Z boson decay (also known as probes) by using a tight selection requirement on the other object produced from the decay (also known as tags). The tag-and-probe pair also had to pass requirements on their reconstructed invariant mass which must coincide with the mass of the Z boson (i.e. 91.1876 $\pm$ 0.0021 GeV [13]). In order to not bias the probes, each valid combination of electron or muon pairs in the event was considered (i.e. the electron or muon can be the tag in one pair and the probe in another). These events had an experimental signature which satisfied:

- At least one jet and at least one b-tagged jet in the event
- At least two electrons or muons with each pair satisfying:
  - A tight electron or muon which fired one of the triggers in Table 6.1
  - A loose electron or muon used as the probe lepton
  - The invariant mass of the pair is at least 50 GeV

Despite this rigid selection criteria, there were still non-prompt and fake leptons which were selected. The most important contribution to these backgrounds came from random combinations of two particles which did not originate from the Z boson decay. Therefore, the invariant mass selection cut was used to distinguish signal leptons from background leptons. The side-band subtraction method was used to extract the signal from the background, in other words determined ϵ_{real} in each bin. This method used the invariant mass distribution of the tag-and-probe leptons for both opposite-sign (OS) and same-sign (SS) lepton pairs, where the OS distribution corresponds to signal Z boson decay and the SS to background. The invariant mass distribution was divided into three regions A (between 70 and 79 GeV, i.e. side-band), B (between 80 and 100 GeV, i.e. central-band or signal-band) and C (between 101 and 110 GeV, i.e. side-band). The number of background events in the signal-band in the signal Z boson decay distribution (i.e. the OS distribution) and it's statistical uncertainty were estimated from the extrapolation

of the side-band regions A and C of the SS distribution and removed from the signal Z boson decay distribution.

6.4.6 Measurement of the fake efficiency

The fake efficiencies, ϵ_{fake}, were measured in control regions dominated by non-prompt and fake lepton background events, i.e. multi-jet events, but can still contain contributions from real leptons. These events had to satisfy the following selection criteria:

- At least one jet and at least one b-tagged jet in the event
- only one loose electron or muon

This control region is trying to isolate low $\mathrm{E_T^{miss}}$ and therefore, low $\mathrm{m_T(lepton,E_T^{miss})}$ to reduce contributions from real leptons. Thus, additional selection criteria has been applied on these two quantities, i.e. $\mathrm{m_T(lepton,E_T^{miss})} < 20$ GeV and $\mathrm{m_T(lepton,E_T^{miss})} + \mathrm{E_T^{miss}} < 60$ GeV. This region is dominated by $t\bar{t}$ events with very small contributions from other SM processes (see in Figures 6.1 - 6.4). These SM processes depict the contribution from real leptons within this control region and therefore, to get a pure non-prompt and fake lepton sample, these contributions need to subtracted from the data. The very small contributions from SM processes other than that of the $t\bar{t}$ is due to the derivation process which only selected events with either a J/ψ, $\psi(2S)$ or Υ meson which decayed into two oppositely charged muons. Therefore, despite there being no further selection criteria on J/ψ candidates in the non-prompt and fake lepton determination, there is still a bias on the event selection. Thus, the fake efficiency was determined for each bin using Equation 6.5, i.e.

$$\epsilon_{\text{fake}} = \left(\frac{\mathrm{N_{fake}^T}}{\mathrm{N_{fake}^L}}\right) = \left(\frac{\mathrm{N^T} - \mathrm{N_{real}^T}}{\mathrm{N^L} - \mathrm{N_{real}^L}}\right) \tag{6.5}$$

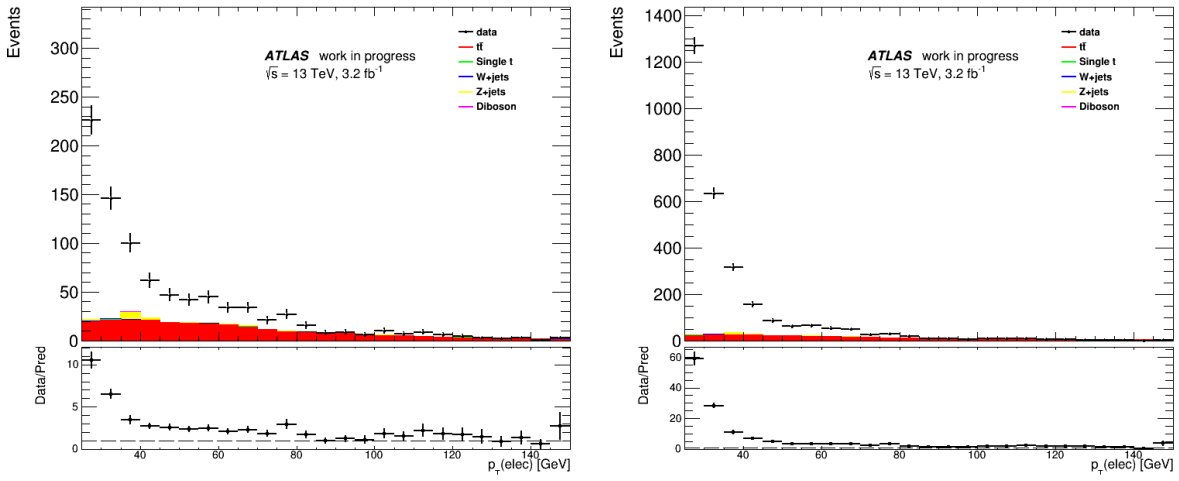

FIGURE 6.1: Distributions of the transverse momentum p_T for data and the contribution from the different SM processes for events passing the tight (left) and loose (right) selection criteria when the selected lepton is an electron candidate.

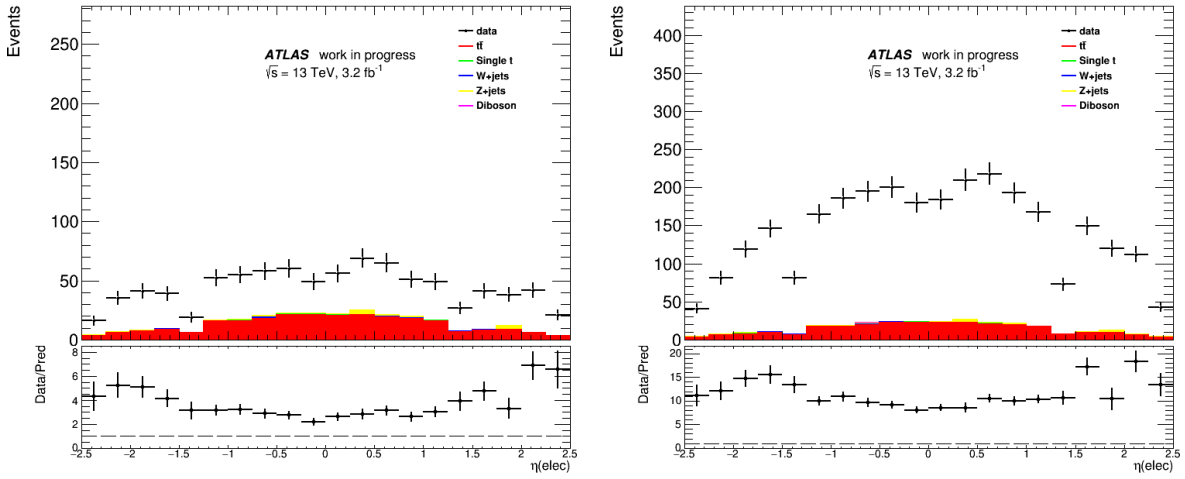

FIGURE 6.2: Distributions of the pseudorapidity for data and the contribution from the different SM processes for events passing the tight (left) and loose (right) selection criteria when the selected lepton is an electron candidate.

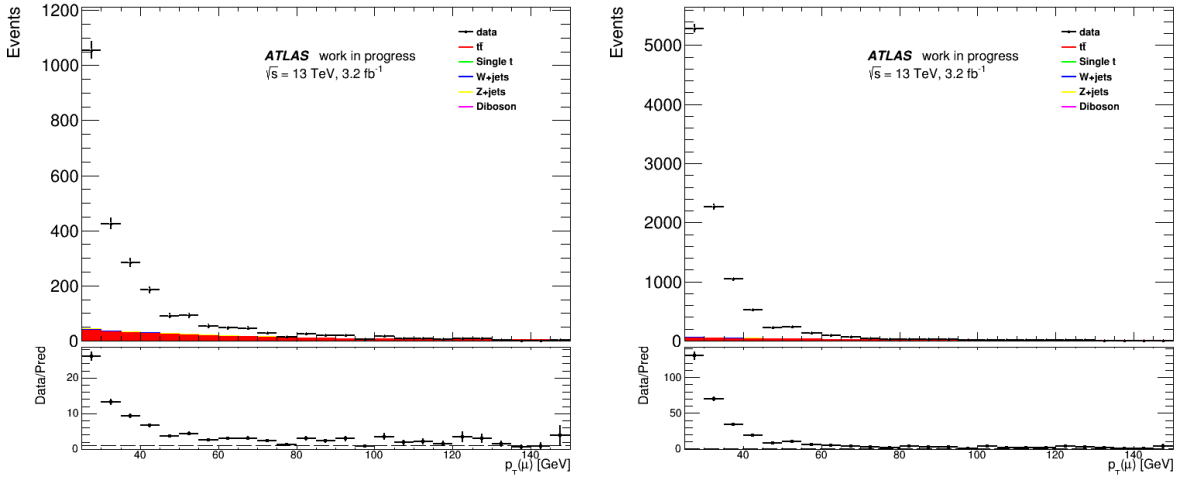

FIGURE 6.3: Distributions of the transverse momentum p_T for data and the contribution from the different SM processes for events passing the tight (left) and loose (right) selection criteria when the selected lepton is an muon candidate.

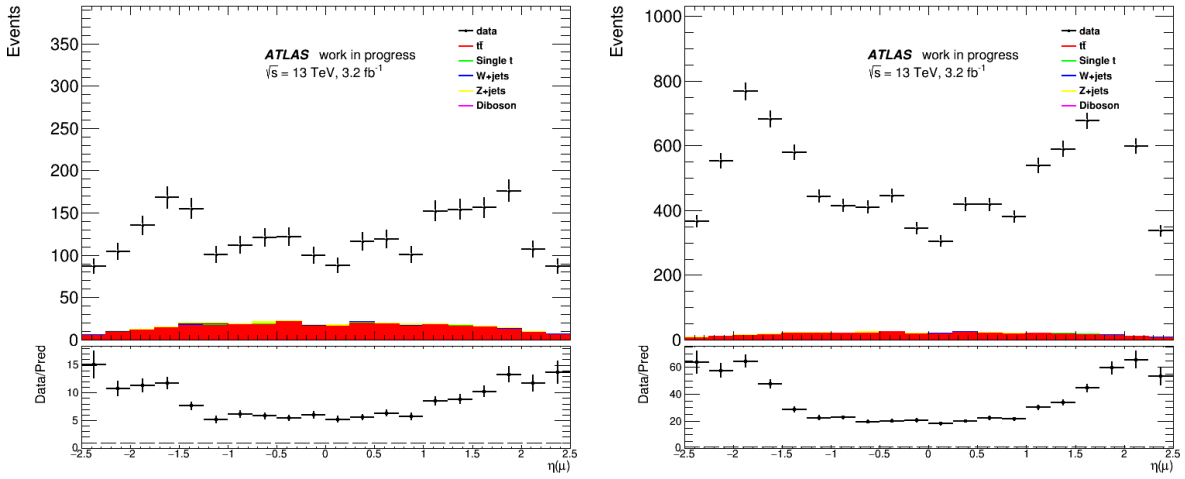

FIGURE 6.4: Distributions of the pseudorapidity for data and the contribution from the different SM processes for events passing the tight (left) and loose (right) selection criteria when the selected lepton is an muon candidate.

6.4.7 Efficiencies

The measured real and fake efficiencies in the p_T and η distributions when the selected lepton was either a muon (referred to as the muon channel) or an electron (referred to as the electron channel) are shown in Figures 6.5 and 6.6, respectively. These efficiency distributions show large statistical uncertainties due to the limited amount of events which passed the selection criteria in each control region. These figures show that the fake efficiency is dependent on the transverse momentum of the non-prompt or fake lepton and independent on the pseudorapidity.

Due to the large uncertainties in the real efficiencies in both the p_T and η distributions, the real efficiencies are independent of lepton kinematics.

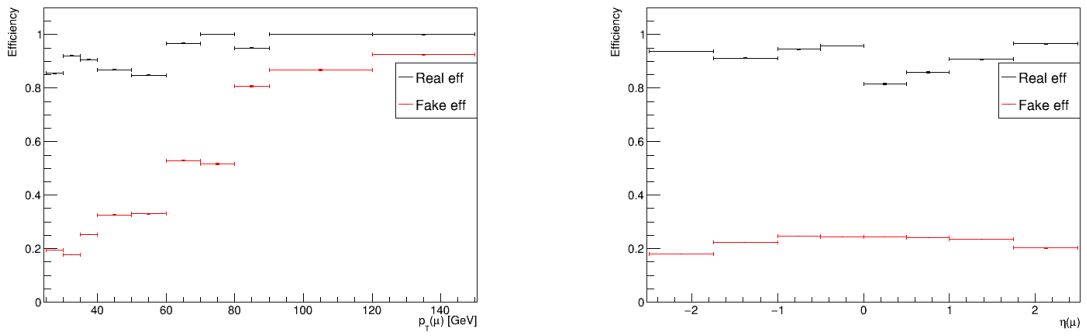

FIGURE 6.5: The measured real ϵ_{real} (blue) and fake ϵ_{fake} (red) efficiencies in the transverse momentum (left) and pseudorapidity (right) distributions in the muon channel. No systematic uncertainties are shown.

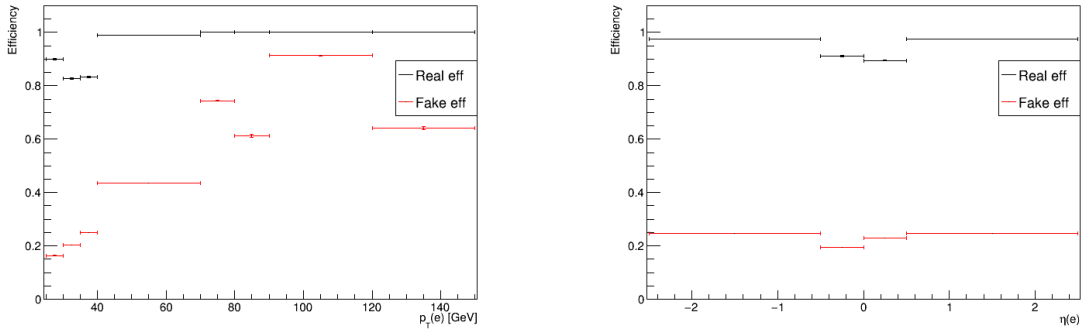

FIGURE 6.6: The measured real ϵ_{real} (blue) and fake ϵ_{fake} (red) efficiencies in the transverse momentum (left) and pseudorapidity (right) distributions in the electron channel. No systematic uncertainties are shown.

6.4.8 Validation of measured efficiencies

The non-prompt or fake lepton background was estimated using additional selection cuts on E_T^{miss} and m_T(lepton,E_T^{miss}) to reduce the contribution of real leptons. To determine the validity of the measured real and fake efficiencies determined in the control region, a validation region was used. This validation region was chosen to contain events which include both non-prompt or fake leptons and real leptons in order to distinguish the signal and background lepton contributions. Therefore, the validation region consisted of events which had only one lepton passing the tight selection criteria, exactly 2 jets and at least 1 b-tagged jet, as well as having no selection criteria on E_T^{miss} and m_T(lepton,E_T^{miss}).

Since the fake efficiencies are dependent on the transverse momentum of the non-prompt or fake lepton (Figures 6.5 and 6.6), the non-prompt or fake lepton background contribution was

determined using the fake and real efficiencies parametrised in p_T. Figures 6.7 and 6.8 show the non-prompt or fake lepton contribution within the validation region. In the electron channel (Figure 6.7), the non-prompt or fake lepton background contribution together with the signal and background SM processes agree reasonably well with data. However, in the muon channel (Figure 6.8), the non-prompt or fake lepton contribution is underestimated which is presumed to be due to the muons from the J/ψ that pass the selection cuts. According to the ratio plot in both distributions of Figure 6.8, the theory prediction appears to be underestimated by a constant factor. After fitting a polynomial of degree 0 over the pseudorapidity distribution, the constant factor comes out to be 1.80 ± 0.04. Figure 6.9 shows the contributions from the data, the individual SM processes and from the non-prompt or fake lepton background contribution after the constant factor was applied.,

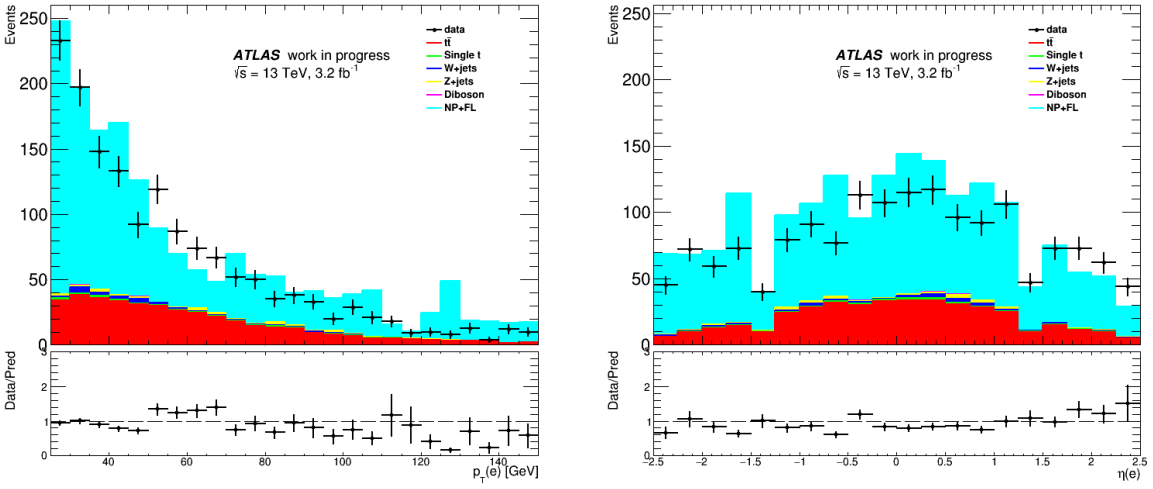

FIGURE 6.7: Distributions of the transverse momentum p_T (left) and pseudorapidity η (right) in the electron channel for data including the contributions from the non-prompt or fake lepton backgrounds and the different SM processes within the validation region. The lower plot shows the ratio between the data and the theoretical prediction.

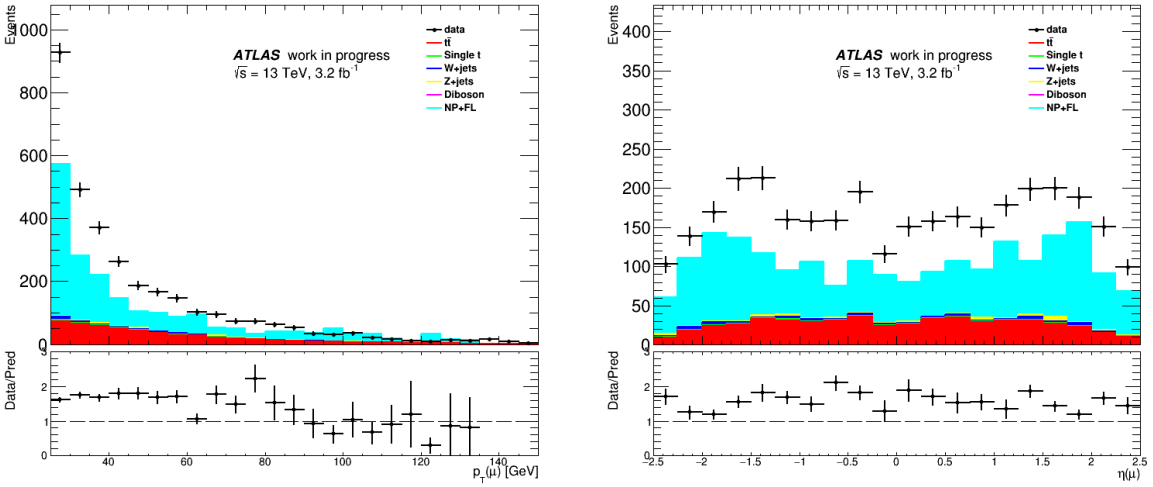

FIGURE 6.8: Distributions of the transverse momentum p_T (left) and pseudorapidity η (right) in the muon channel for data including the contributions from the non-prompt or fake lepton backgrounds and the different SM processes within the validation region. The lower plot shows the ratio between the data and the theoretical prediction.

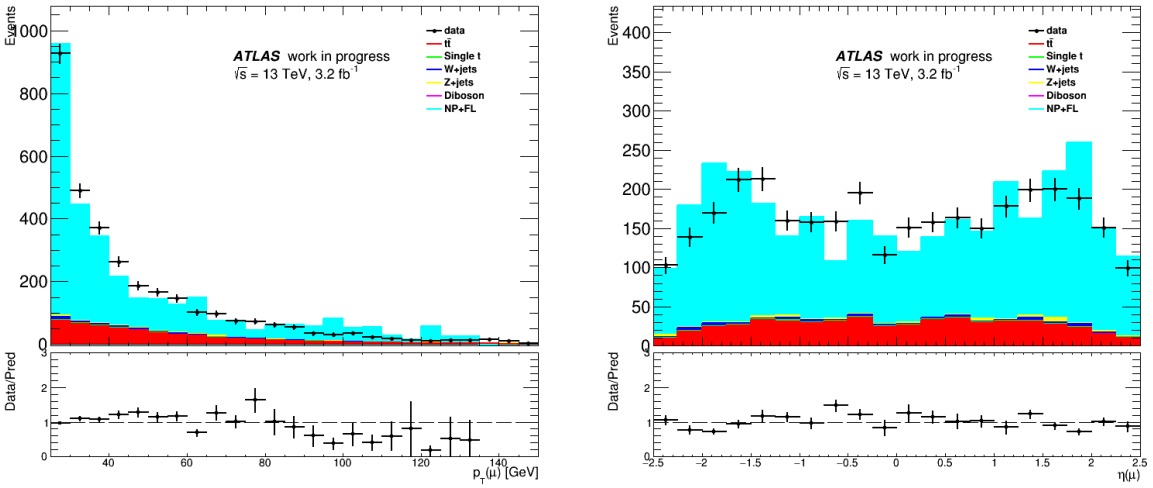

FIGURE 6.9: Distributions of the transverse momentum p_T (left) and pseudorapidity η (right) in the muon channel for data including the contributions from the non-prompt or fake lepton backgrounds after scaling by a constant factor of 1.8 and the different SM processes within the validation region. The lower plot shows the ratio between the data and the theoretical prediction.

6.5 Signal region object kinematics

Since there were large differences between the control and validation regions and the signal region, the non-prompt or fake lepton background contribution was not expected to be accurately

estimated in the signal region. However, the work was done to estimate this background contribution and therefore, the non-prompt or fake lepton background contribution was included in the signal region object kinematic distributions.

The efficiencies in the muon and electron channels were different (Figures 6.5 and 6.6) and therefore, the non-prompt or fake lepton background estimation will be different. Figures 6.10 and 6.11 show the non-prompt or fake lepton background contribution in the muon channel and electron channel, respectively. In the muon channel, the non-prompt or fake lepton background is significantly overestimated but, in the electron channel, its more accurately estimated. Therefore, the non-prompt or fake lepton background contribution was estimated in the electron channel in the object kinematic distributions in the signal region (see Figures 6.12 - 6.15). The same lepton background contribution in the muon channel is shown in Figures A.1 - A.5 in Appendix A. The muon channel distributions show the non-prompt and fake lepton background without rescaling by 1.8, since with it, the contribution will be even larger. A more reasonable estimation of the non-prompt or fake lepton background can be made by choosing control and validation regions which matches the signal region more closely and will be included in future studies.

The selected final state particles in the signal region are not unique to top quark processes and therefore, there are other SM processes which contribute to the background within the signal region. Figures 6.10 - 6.15 show different object kinematic distributions for data and the individual contributions from signal and background SM processes, as well as the contribution from non-prompt or fake lepton backgrounds in either the muon or electron channel. In each distribution in Figures 6.10 - 6.15, the signal and background SM processes overestimates the data which could point out inefficiencies in the MC simulations and will be included in future studies. However, these figures also show that almost all of the objects within this signal region originated from $t\bar{t}$ events and a small contribution from single top events. There are objects which originated from background SM processes with W+jets being the most dominant. Although, the amount of objects originating from background events is almost negligible when compared to the contribution of objects originating from signal top quark events. Figure 6.15 shows the invariant mass of the lepton+J/ψ distribution in the signal region electron channel which is used to determine the top mass. This invariant mass distribution is dominated by signal top quark SM processes with very small contributions from background processes and therefore, this signal region is a valid channel to make a top quark mass measurement.

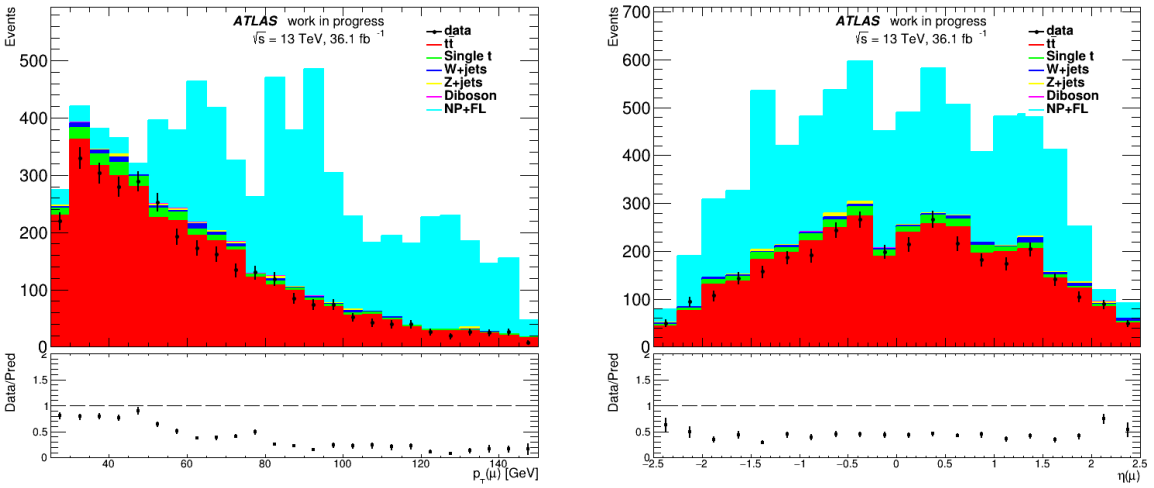

FIGURE 6.10: The upper plot shows the distributions of the transverse momentum (left) and pseudorapidity (right) of the lepton candidates in the signal region muon channel. These distributions contain the data, the contributions from the different signal and background SM processes and the contribution from non-prompt or fake lepton backgrounds. Only the statistical uncertainty in the data is shown. The lower plot shows the ratio between the data and the theoretical predictions.

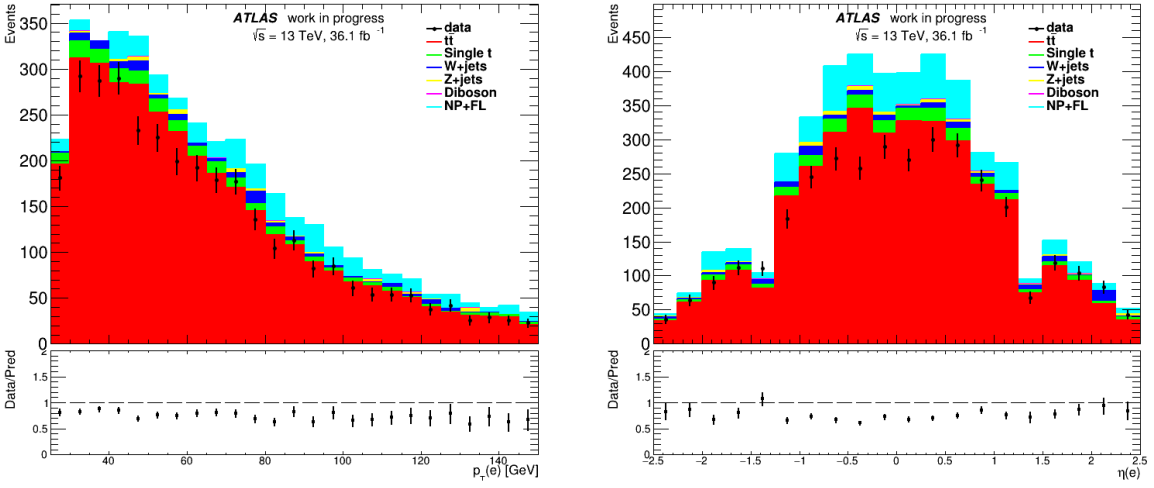

FIGURE 6.11: The upper plot shows the distributions of the transverse momentum (left) and pseudorapidity (right) of the lepton candidates in the signal region electron channel. These distributions contain the data, the contributions from the different signal and background SM processes and the contribution from non-prompt or fake lepton backgrounds. Only the statistical uncertainty in the data is shown. The lower plot shows the ratio between the data and the theoretical predictions.

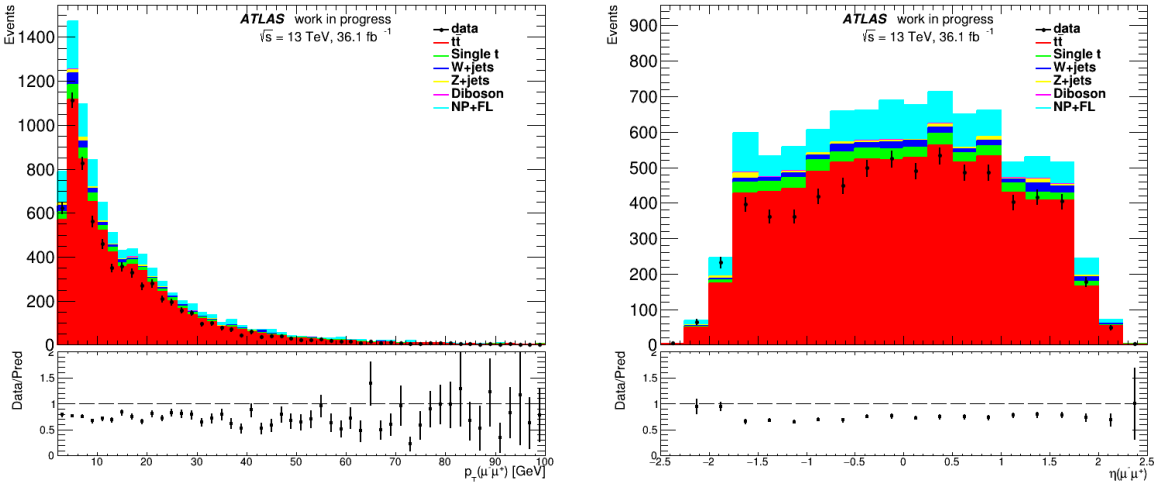

FIGURE 6.12: The upper plot shows the distributions of the transverse momentum (left) and pseudorapidity (right) of the muon candidates coming from the J/ψ in the signal region electron channel. These distributions contain the data, the contributions from the different signal and background SM processes and the contributions from non-prompt or fake lepton backgrounds. Only the statistical uncertainty in the data is shown. The lower plot shows the ratio between the data and the theoretical predictions.

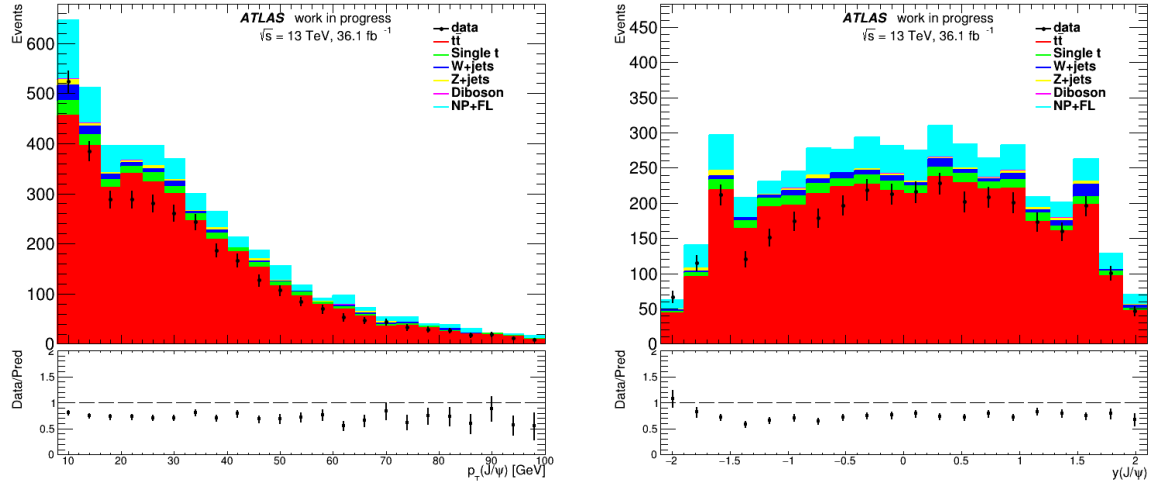

FIGURE 6.13: The upper plot shows the distributions of the transverse momentum (left) and pseudorapidity (right) of the J/ψ candidates in the signal region electron channel. These distributions contain the data, the contributions from the different signal and background SM processes and the contribution from non-prompt or fake lepton backgrounds. Only the statistical uncertainty in the data is shown. The lower plot shows the ratio between the data and the theoretical predictions.

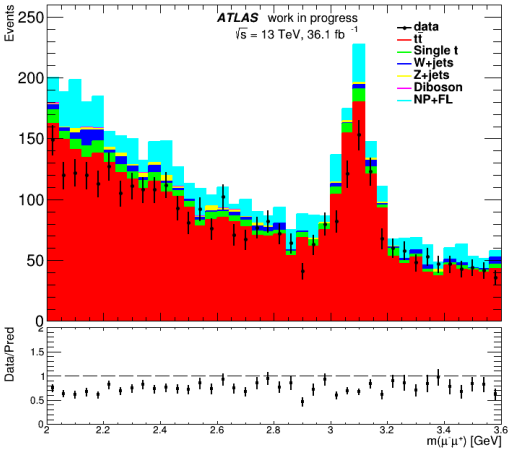

FIGURE 6.14: The upper plot shows the invariant mass distribution of the muon pairs matched to a common vertex in the signal region electron channel. This distribution contains the data, the contributions from the different signal and background SM processes and the contribution from non-prompt or fake lepton backgrounds. Only the statistical uncertainty in the data is shown. The peak within the plot represents the resonant J/ψ meson mass. The lower plot shows the ratio between the data and the theoretical predictions.

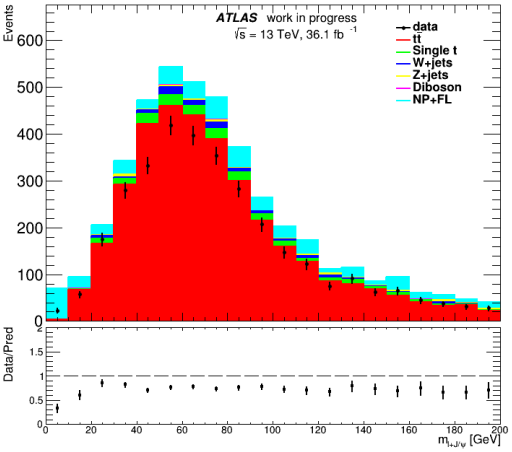

FIGURE 6.15: The upper plot shows the invariant mass distribution of the lepton and J/ψ candidates in the signal region electron channel. This distributions contains the data, the contributions from the different signal and background SM processes and the contribution from non-prompt or fake lepton backgrounds. Only the statistical uncertainty in the data is shown. The peak within the plot represents the signal contribution while the tail represents the background contribution to the top mass value which produced this distribution. The lower plot shows the ratio between the data and the theoretical predictions.

6.6 J/ψ background

The mass of a J/ψ meson is ~3.096 GeV. In Figure 6.14, there is a peak around the J/ψ mass which shows that many real J/ψ candidates were selected within the signal region electron channel. However, there are also many "other" J/ψ candidates which fall outside of this peak and are most likely coming from random muon pairings. From this point forward, the signal region will consist of data from both the muon and electron channels. The following section describes an approach to determine the different J/ψ candidates in the signal region. A similar approach was described in reference [93] and may be consulted for more information.

The reconstructed J/ψ candidates were determined by combining the track and fit information from two oppositely charged muons in every event. However, these J/ψ candidates could have originated from processes other than from top quark B-hadron decays. J/ψ candidates originating from top quark B-hadron decays and directly from the proton-proton collision are referred to as non-prompt signal and prompt J/ψ background mesons, respectively. There are,

however, other background processes which include J/ψ candidates originating from B-hadron decays not coming from top quarks (i.e. non-prompt background) or from randomly combining two oppositely charged muons that have a mass near that of the J/ψ meson (i.e. prompt and non-prompt combinatorial background).

Since B-hadron decays exhibit displaced vertices from the primary vertex, prompt and non-prompt J/ψ candidates can be distinguished by studying their decay vertices. This can be done by using a pseudo-proper time variable which makes use of time dilation and length contraction since the proton bunches collide at speeds near that of light. The proper decay time of B-hadrons is related to its proper decay length through $\tau = l/\mathrm{v}$, where l is the contracted length, v is the speed of the B-hadrons and τ is the dilated time variable. The proper decay length can be represented by its actual decay length undergoing time dilation through $l = \mathrm{L}/\gamma$, where L is the decay distance between the primary vertex and the B-hadrons decay vertex. Therefore, the proper decay time is related to the decay distance of the B-hadrons through $\tau = \mathrm{L}/(\gamma\mathrm{v})$. Using the relativistic momentum relation, i.e. $\mathrm{p} = \gamma\mathrm{mv}$, where m is the mass and p is momentum of the B-hadrons, the proper decay time can be written as $\tau = \mathrm{Lm}/\mathrm{p}$. However, since the ATLAS detector cannot fully reconstruct the momentum of the B-hadrons, a good approximation would be to use the transverse momentum (and the mass) of the J/ψ candidates coming from B-hadrons. This will also aid in approximating the decay distance description since the decay distance L can be projected onto the direction of the J/ψ candidates using the reconstructed transverse momentum. Thus, a "pseudo-proper time" variable τ can be used to represent the decay lifetime of B-hadrons, i.e.

$$\tau \equiv \frac{\vec{L} \cdot \vec{p_T}(J/\psi)}{p_T(J/\psi)} \frac{m_{\mu^+\mu^-}}{p_T(J/\psi)} \tag{6.6}$$

where $\vec{L}$ is the displacement vector from the primary vertex to the J/ψ decay vertex and $\mathrm{m}_{\mu^+\mu^-}$ is the reconstructed mass of the J/ψ candidates (using the invariant mass of the dimuon pair). In theory, non-prompt J/ψ decay vertices should have a $\tau > 0$ (which represents a displaced vertex) whereas prompt J/ψ decay vertices should have a $\tau = 0$. Experimentally, however, these decay vertices will correspond to smeared τ values due to the vertex resolution of the detector. Figure 6.16 shows the pseudo-proper time distribution of the J/ψ candidates which passed the selection criteria in the signal region electron channel. The electron channel distribution is shown to emphasize the contributions from the data and the individual SM processes and the same distribution in the muon channel can be seen in Figure A.4 in Appendix A. This distribution shows that the dominant contribution of J/ψ mesons in the signal region is coming from $t\bar{t}$ events with small contributions originating from single top quark processes and almost negligible contributions originating from background SM processes. This dominant signal top

quark process contribution is a common feature within this signal region and elucidates the fact that most of the selected candidates originated from top quarks.

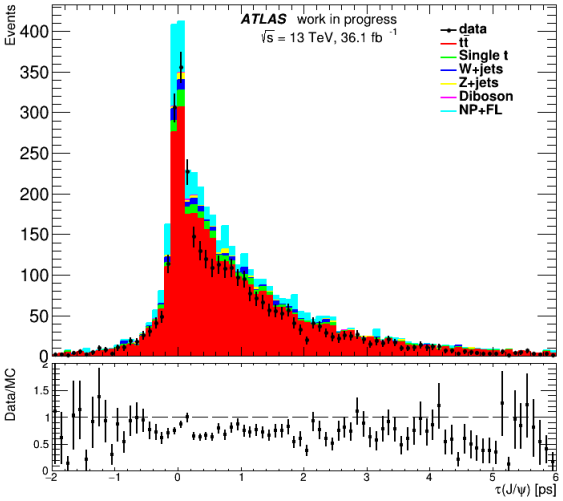

FIGURE 6.16: The upper plot shows the pseudo-proper time distribution of the J/ψ candidates within the signal region electron channel. This distribution contains the data, the contributions from the different signal and background SM processes and the contribution from non-prompt or fake lepton backgrounds. Only the statistical uncertainty in the data is shown. The peak within the plot represents the contribution from prompt J/ψ mesons. The lower plot shows the ratio between the data and the theoretical predictions.

6.6.1 Non-prompt signal J/ψ determination

Since the invariant mass and pseudo-proper time of the J/ψ candidates can be used to distinguish signal and background prompt and non-prompt J/ψ mesons, a two-dimensional fit was applied to these distributions in data to determine the individual J/ψ contributions.

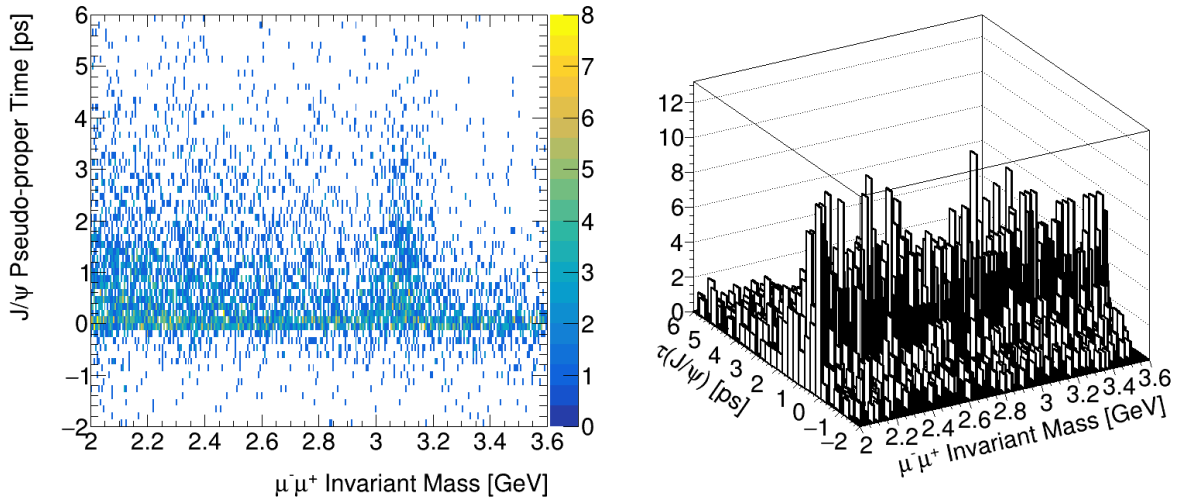

FIGURE 6.17: Two-dimensional plot of the pseudo-proper time of the J/ψ candidates and the invariant mass of the dimuon pair in the signal region. On the left is the color map where the right y-axis represents the counts and on the right is the lego plot.

In the invariant mass distribution (see Figure 6.14), the probability density functions for the prompt and non-prompt signal J/ψ candidates were modelled by Gaussian distributions while background processes were modelled by exponential functions. In the pseudo-proper time distribution (see Figure 6.16), the prompt signal and background components were modelled by the sum of a delta-function distribution and a double-sided exponential function convoluted with a Gaussian function. However, the non-prompt signal and background components were modelled by an exponential function convoluted with a Gaussian function. These probability density functions were defined in reference [93] as

$$
\begin{aligned}
M_{J/\psi}(m_{\mu^+\mu^-}) &= G(m_{\mu^+\mu^-}; m_{J/\psi}^{PDG}, \sigma_m) \\
T_{\text{prompt } J/\psi}(\tau) &= G(\tau; 0, \sigma_\tau) \otimes \left((1-a)\delta(\tau) + a e^{-|\tau|/\tau_0} \right) \\
T_{\text{non-prompt } J/\psi}(\tau) &= G(\tau; 0, \sigma_\tau) \otimes \left(\Theta(\tau) e^{-\tau/\tau_1} \right) \\
M_{\text{prompt bkg}}(m_{\mu^+\mu^-}) &= e^{-m_{\mu^+\mu^-}/k_0} \\
M_{\text{non-prompt bkg}}(m_{\mu^+\mu^-}) &= e^{-m_{\mu^+\mu^-}/k_1} \\
T_{\text{prompt bkg}}(\tau) &= G(\tau; 0, \sigma_\tau) \otimes \left((1-b)\delta(\tau) + b e^{-|\tau|/\tau_2} \right) \\
T_{\text{non-prompt bkg}}(\tau) &= G(\tau; 0, \sigma_\tau) \otimes \left(\Theta(\tau) e^{-\tau/\tau_3} \right),
\end{aligned}
$$

where $m_{J/\psi}^{PDG}$ is the mass of the J/ψ meson in the Particle Data Group (PDG, i.e. reference [13]). The a, b, σ_m, σ_τ, k_i and τ_i are nuisance parameters with limits designed to produce a convergence. The total probability density function was defined in reference [93] as

$$
\begin{aligned}
\mathrm{p}_{\mathrm{total}}(m_{\mu^+\mu^-}, \tau) = N_{\text{signal } J/\psi}[&N_{\text{prompt } J/\psi} M_{J/\psi}(m_{\mu^+\mu^-}) T_{\text{prompt } J/\psi}(\tau) \\
&+ (1 - N_{\text{prompt } J/\psi}) M_{J/\psi}(m_{\mu^+\mu^-}) T_{\text{non-prompt } J/\psi}(\tau)] \\
+ (1 - N_{\text{signal } J/\psi})[&N_{\text{prompt bkg}} M_{\text{prompt bkg}}(m_{\mu^+\mu^-}) T_{\text{prompt bkg}}(\tau) \\
&+ (1 - N_{\text{prompt bkg}}) M_{\text{non-prompt bkg}}(m_{\mu^+\mu^-}) T_{\text{non-prompt bkg}}(\tau)]
\end{aligned}
\tag{6.7}
$$

After fitting the two-dimensional plot in Figure 6.17 with the total probability density function, the total and individual fit results in the invariant mass and pseudo-proper time distributions of the selected J/ψ candidates can be seen in Figure 6.18. In the invariant mass distribution, the peak around the J/ψ mass is dominated by non-prompt signal J/ψ candidates with an almost negligible contribution from background prompt J/ψ meson. There are, however, sizable contributions from both prompt and non-prompt combinatorics with the majority coming from non-prompt. In the pseudo-proper time distribution, the combinatoric background contributions dominate and there is a reasonable contribution coming from signal non-prompt J/ψ candidates. Once again, there is an almost negligible contribution from background prompt J/ψ candidates. However, the fit results show that by applying a tighter selection cut on the mass (i.e. 2.9 GeV to 3.3 GeV) and an additional pseudo-proper time selection cut (i.e. $\tau > 0$ ps) on the J/ψ candidates in the signal region, the signal to background ratio will improve.

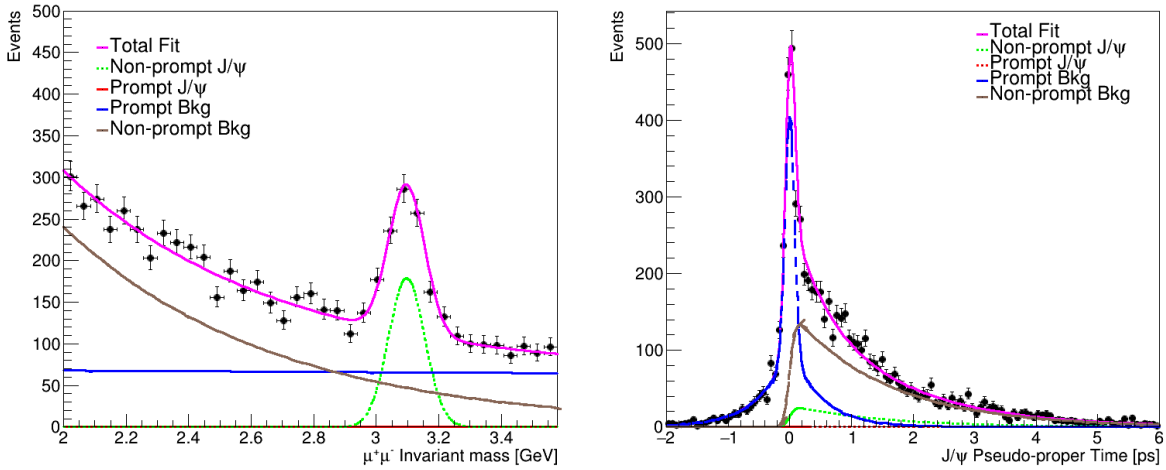

FIGURE 6.18: The invariant mass distribution of the dimuon pair (on the left) and the pseudo-proper time distribution of the J/ψ candidates (on the right) with the contributions from each individual process as well as the total contribution. The prompt J/ψ contribution comes out to be very small and can be seen by the red projection.

6.6.2 Non-prompt signal J/ψ sanity check

Since the signal region is dominated by $t\bar{t}$ events, the same procedure as described before to separate out the different J/ψ contributions can be done on the $t\bar{t}$ signal MC sample. This was done to compare the different J/ψ contributions in data with the different J/ψ contributions which originate from $t\bar{t}$ events.

A two-dimensional fit was applied in the signal region to the invariant mass and pseudo-proper time distribution in the $t\bar{t}$ MC sample using the total probability density function described in Equation 6.7. The total and individual fit results in both the invariant mass and pseudo-proper time distributions can be seen in Figure 6.19. These fit results not only show that even in $t\bar{t}$ events, there are J/ψ candidates which do not originate from top quark B-hadrons decays but also show that by applying the same tighter selection on the mass (i.e. 2.9 GeV to 3.3 GeV) and pseudo-proper time (i.e. $\tau > 0$ ps) of the J/ψ candidates, the signal to background ratio will improve. Therefore, the data does correspond to $t\bar{t}$ and, subsequently, top quark events.

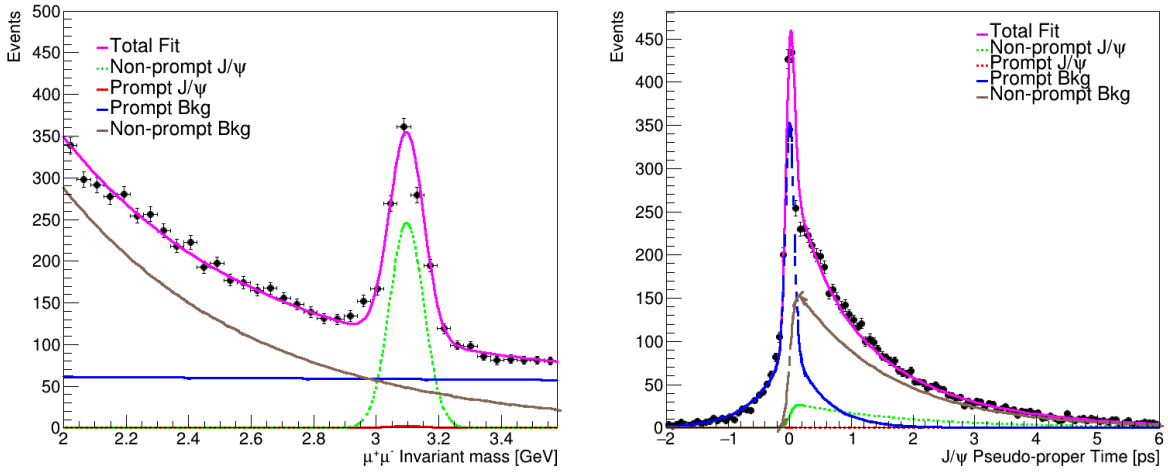

FIGURE 6.19: The invariant mass distribution of the dimuon pair (on the left) and the pseudo-proper time distribution of the J/ψ candidates (on the right) with the contributions from each individual process as well as the total contribution. The prompt J/ψ contribution comes out to be very small and can be seen by the red projection.

6.6.3 Throwing away unwanted J/ψ mesons

It is now evident that there are J/ψ mesons which do not originate from top quark B-hadron decays in top quark events. The results in Figures 6.18 and 6.19 show that by applying a tighter selection cut on the mass of the J/ψ candidates of 2.9 GeV $< m_{\mu^+\mu^-} <$ 3.3 GeV, the signal to background ratio will improve. Furthermore, the fit results also show that by including a pseudo-proper time selection cut of $\tau > 0$ ps, the signal to background ratio will improve. This can be qualitatively tested as the same two-dimensional fit using the same total probability

density function can be done after applying these tighter selection criteria separately. The left plot of Figure 6.20 shows the different J/ψ contributions in the pseudo-proper time distribution after applying only a tighter J/ψ mass selection cut between 2.9 GeV and 3.3 GeV whereas the right plot shows the different J/ψ contributions in the invariant mass distribution after only applying an additional pseudo-proper time selection cut of $\tau > 0$ ps. The left plot in Figure 6.20 shows an increase in the non-prompt signal J/ψ contribution with a decrease in the non-prompt background contribution after applying the tighter mass selection when compared to pseudo-proper time distribution in Figure 6.18. The right plot of Figure 6.20 shows a decrease in the non-prompt background, an increase in the prompt background and that the non-prompt signal contributes more to the peak around the J/ψ mass when compared to invariant mass distribution in Figure 6.18. Therefore, by applying either selection, the signal to background ratio increases.

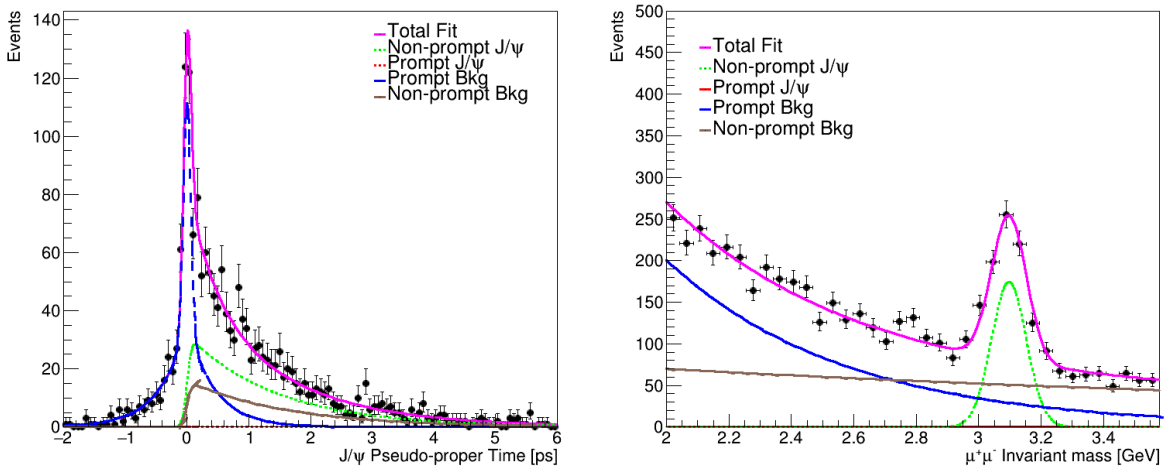

FIGURE 6.20: The left plot is the pseudo-proper time distribution of the J/ψ candidates after a tighter J/ψ mass selection cut between 2.9 GeV and 3.3 GeV was only applied. The right plot is the invariant mass distribution of the dimuon pair after the pseudo-proper time selection cut of $\tau > 0$ ps was only applied. In each distribution, the contributions from the individual processes as well as the total contribution is shown. The prompt J/ψ contribution comes out to be very small and can be seen by the red projection.

The signal to background ratio increases when the selection cuts are applied individually and therefore, should maintain this signal to background increase if the selection cuts were applied together. Figure 6.21 shows the invariant mass and pseudo-proper time distributions of the J/ψ candidates after both selection cuts were applied. When comparing the results in Figure 6.21 with the results in Figure 6.18, both background contributions are significantly reduced in the invariant mass distribution and the prompt background becomes negligible and the non-prompt background is reduced in the pseudo-proper time distribution. Therefore, by applying the selection cuts together, the signal to background ratio improves.

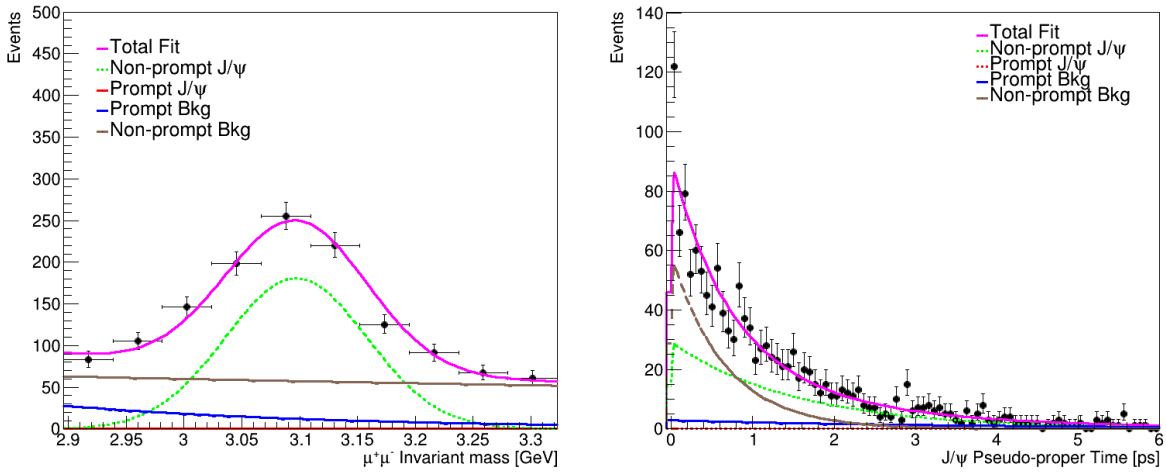

FIGURE 6.21: The invariant mass distribution of the dimuon pair (on the left) and the pseudo-proper time distribution of the J/ψ candidates (on the right) after a tighter J/ψ mass selection between 2.9 GeV and 3.3 GeV and a pseudo-proper time selection cut of $\tau > 0$ ps was applied. In each distribution, the contributions from the individual processes as well as the total contribution is shown. The prompt J/ψ contribution comes out to be very small and can be seen by the red projection.

6.6.4 Double parton scattering

When the proton bunches collide, it is possible for two different parton interactions to occur in a single proton-proton collision, which produces the final-state signature of this analysis. This is known as a double parton scattering (DPS) interaction. The fraction of DPS events producing the signal signature can be estimated by dividing the DPS cross section [94] by the signal process cross section. The DPS cross section producing the final-state signature of this analysis is defined as

$$\sigma^{\text{DPS}}_{J/\psi+W\to l\nu} = \frac{\sigma_{b\bar{b}} \times BR(b \to J/\psi)\sigma_{W\to l\nu}}{\sigma_{\text{eff}}}$$

where $\sigma_{b\bar{b}}$ (i.e. 495±2 μb [95]) and $\sigma_{W\to l\nu}$ (i.e. 20.62±0.03 nb [96]) are the cross sections for producing inclusive $b\bar{b}$ and $W \to l\nu$, respectively, and σ_{eff} is a parameter measured for DPS interactions by ATLAS (i.e. 15±3(stat) mb [94]) in $W \to l\nu$+2jet events. This σ_{eff} parameter was assumed to be independent on the scattering process. The cross section for the signal process is $\sigma_{t\bar{t}} \times BR(t \to Wb)^2 \times BR(b \to J/\psi) \times BR(W \to l\nu)$, where each of these values were taken from reference [13]. The fraction of DPS events producing the final-state signature of this analysis was found to be 8.2±1.7. However, the fraction of DPS events was expected to be significantly lower. The reason for this larger than expected contribution was due to the fact that the inclusive $b\bar{b}$ production cross section includes events outside of the acceptance in this analysis. Since b quarks are much lighter than top quarks, they and their corresponding

decay products will have high-momentum in the forward region of the detector (i.e. outside of the fiducial region in this analysis). Due to the heaviness of the top quark, the b quarks coming from top quarks (and, subsequently, the b quarks' decay products) will have higher transverse momentum in the central region of the detector than those produced directly from the proton-proton collision. Therefore, the signal selection of two b-tagged jets with a $p_{\mathrm{T}} > 40$ GeV and two oppositely charged muons found in the central region, should significantly reduce the fraction of DPS events. Accurately estimating the contribution from DPS in the lepton+jets(b-tagged)+J/ψ channel fiducial region will be the focus of future studies.

6.7 Uncertainty in the top mass measurement

The mass of the top quark can be determined from the kinematics of its decay products through a maximum likelihood method. The invariant mass of the lepton+J/ψ distribution is sensitive to the mass of the top quark and was therefore used to determine the uncertainty in the mass measurement. This process was done by linearly interpolating the invariant mass of the lepton+J/ψ distribution from two $t\bar{t}$ MC samples with predefined top mass values. The interpolation then produces a top mass value together with its statistical uncertainty which bests describes the invariant mass of the lepton+J/ψ distribution in the signal region. This process is known as template morphing. These two $t\bar{t}$ MC samples were generated using Powheg-Box and the parton showering, hadronisation and underlying event were simulated using Pythia8 with the A14 tune and NNPDF23LO parton distribution function set. These two MC samples were simulated with a top quark mass value of 170 GeV and 175 GeV, respectively. The two MC samples went through the same preselection and experimental signature selection process as described under Section 6.2 and 6.3 and were normalized to data. These two top quark values were used since all the measured values for the mass of the top quark were between 170 GeV and 175 GeV (see reference [13] for the measured values).

6.7.1 Extracting the mass from the data

The invariant mass of the lepton+J/ψ distribution can be modelled by the sum of a Gaussian distribution [97], which is expected to describe the peak and signal component, and a Gamma distribution [97], which is expected to describe the tail and background component. The background component in this distribution originates from pairing the lepton and the J/ψ meson from different top quarks as well as from possible non-correlated backgrounds [98]. This model describes a shape which the distribution follows (also called a template) and the invariant mass of the lepton+J/ψ template is dependent on the mass of the top quark. Figure 6.22 shows the invariant mass of the lepton+J/ψ distribution for data and the two $t\bar{t}$ template MC samples.

A one-to-one comparison between the data and the MC in Figure 6.22 cannot be made due to background contributions present in the data and not in the signal-only MC samples.

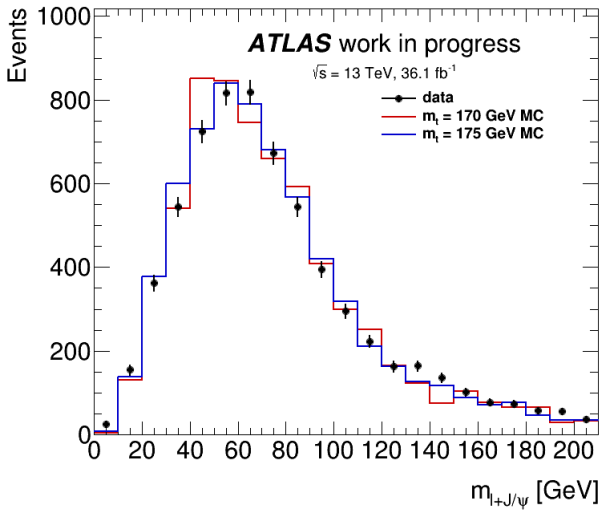

FIGURE 6.22: The invariant mass distribution of the J/ψ and lepton candidates for the data and the two template MC samples. The MC samples were normalized to data.

The probability density function of the sum of the Gaussian and Gamma distributions was fitted over the two $t\bar{t}$ template distributions. The Gaussian and Gamma parameters were allowed to vary between limits which produced convergences. Figure 6.23 shows the invariant mass of the lepton+J/ψ distribution which includes the probability density function fit and the individual contributions from the signal and background components for both the 170 GeV and 175 GeV templates. The parameter results for both template fits can be seen in Table 6.5. The fit results show that the peak in the invariant mass distribution is mostly described by the signal component but has a sizable contribution from the background component and the tail is dominated by the background component. This sizable background contribution is believed to be due to the background J/ψ mesons within the signal region.

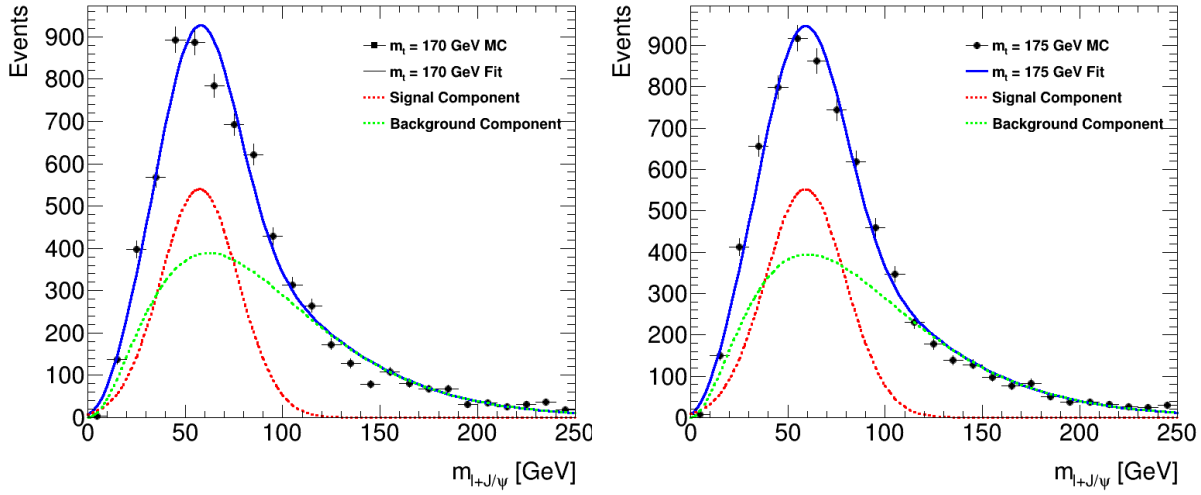

FIGURE 6.23: The invariant mass distribution of the J/ψ and lepton candidates for the 170 GeV (left) and 175 GeV (right) MC samples in the signal region. The probability density function fit and the signal and background components are shown.

Parameter	m_t = 170 GeV MC	m_t = 175 GeV MC
Fraction of signal component	0.389 ± 0.036	0.398 ± 0.035
μ_{Gauss}	57.33 ± 0.97	59.05 ± 0.89
σ_{Gauss}	19.8 ± 0.8	20.6 ± 0.7
Γ_γ	3.2 ± 0.1	3.0 ± 0.1
Γ_β	28.2 ± 1.2	29.5 ± 1.2

TABLE 6.5: Parameter fit results of the two $t\bar{t}$ MC samples.

The final parameters from the fitted probability density functions in the two MC templates were used as starting templates and then linearly interpolated to determine the top mass value which produced the invariant mass of the lepton+J/ψ distribution in the signal region. However, this analysis is primarily focused on the uncertainty in the top mass measurement and therefore, the exact value of the top mass is unknown. Figure 6.24 shows interpolated templates for different top mass values and the interpolated fit over the data in the signal region. The interpolation produced a statistical uncertainty of 2.9 GeV in the top mass measurement. However, no convergence was found and the result for the uncertainty can not be trusted. This non-convergence is believed to be from limited statistics and therefore, with more statistics, a convergence could be found.

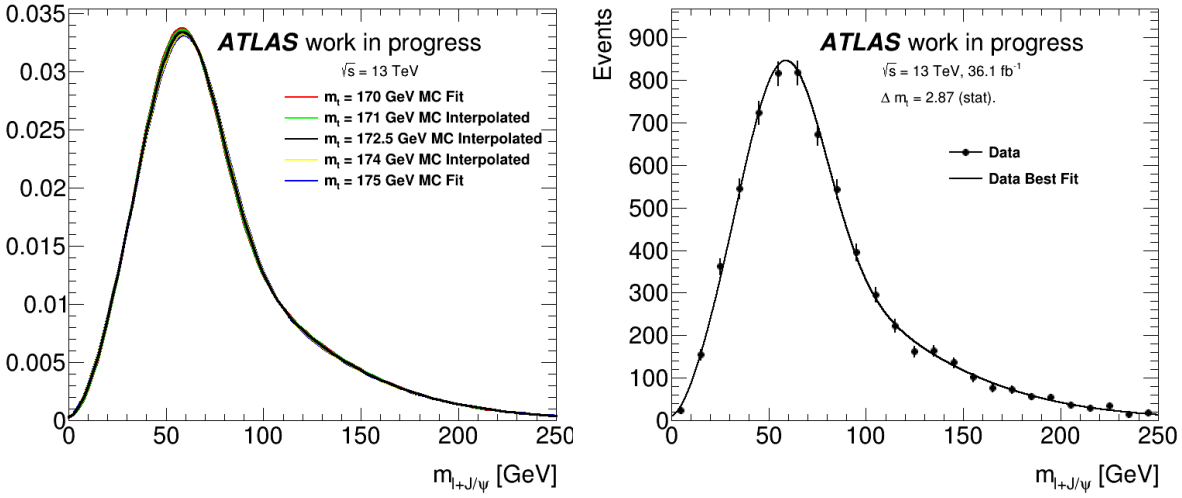

FIGURE 6.24: The interpolated templates which represent the invariant mass distribution of the J/ψ and lepton candidates for different values for the top mass, starting with two MC template samples of 170 GeV and 175 GeV is shown on the left. The invariant mass distribution of the J/ψ and lepton candidates for data and the probability density function fit result of the interpolation between 170 GeV and 175 GeV is shown on the right. In the upper right of the right plot, the statistical uncertainty of the top mass measurement is shown.

6.7.2 Impact on the uncertainty measurement

The signal to background ratio can improve if the selection criteria of the J/ψ candidates tighten. From Figure 6.18, a tighter mass selection and an additional pseudo-proper time selection can be used to reduce the background J/ψ contributions. The following sections show the impact of these selections separately and then together on the two MC template samples. The interpolation was made to data in each case but no convergences was found and therefore, the uncertainty results can not be trusted. For completeness, the uncertainty results in each case were quoted.

6.7.2.1 Tighter J/ψ mass cut

From the invariant mass distribution in Figure 6.18, the prompt and non-prompt background contributions can be reduced by applying a tighter selection criteria around the J/ψ mass to be between 2.9 GeV and 3.3 GeV. After applying this tighter selection criteria to the two template MC samples, the probability density function had to be refitted. The probability density function fit result can be seen in Figure 6.25 and the parameter fit results in Table 6.6.

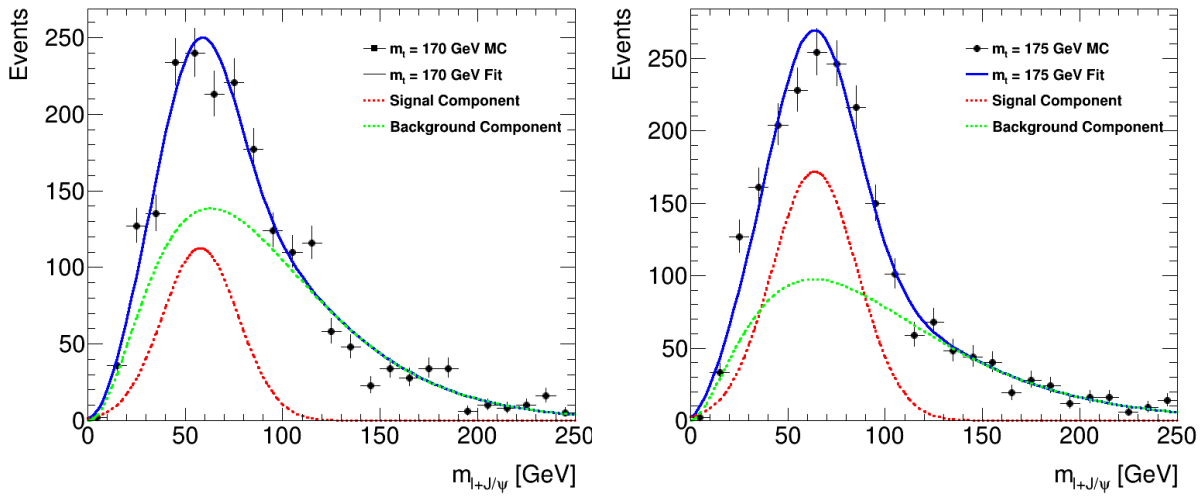

FIGURE 6.25: The invariant mass distribution of the J/ψ and lepton candidates for the 170 GeV (left) and 175 GeV (right) MC samples in the signal region after applying a tighter J/ψ mass selection between 2.9 GeV and 3.3 GeV. The probability density function fit and the signal and background components are shown.

Parameter	m_t = 170 GeV MC	m_t = 175 GeV MC
Fraction of signal component	0.267 ± 0.063	0.443 ± 0.063
μ_{Gauss}	57.76 ± 2.58	63.78 ± 1.51
σ_{Gauss}	19.44 ± 1.86	21.89 ± 1.25
Γ_γ	3.25 ± 0.19	2.79 ± 0.18
Γ_β	28.02 ± 1.85	35.34 ± 3.01

TABLE 6.6: Parameter fit results of the two $t\bar{t}$ MC samples after applying a tighter selection on the mass of the J/ψ candidates to be between 2.9 GeV and 3.3 GeV.

After applying this tighter mass selection, the background J/ψ contributions is reduced and the signal to background ratio improves (see Section 6.6.3). Therefore, the fraction of the signal component should increase. However, the results of the fit in the 170 GeV sample show a decrease in the signal component but show an increase in the signal component in the 175 GeV sample. The decrease in signal component in the 170 GeV sample can be attributed to the limited amount of statistics within this tighter mass region and the fewer J/ψ candidates at the peak (i.e. not a sharp peak) in the mass distribution of the J/ψ candidates (which contributes to the background component and can be seen in Figure 6.26). The interpolation was made to data and the statistical uncertainty improved from 2.9 GeV to 0.64 GeV. However, no convergence was found which is believed to be due to limited statistics and therefore, the result cannot be trusted.

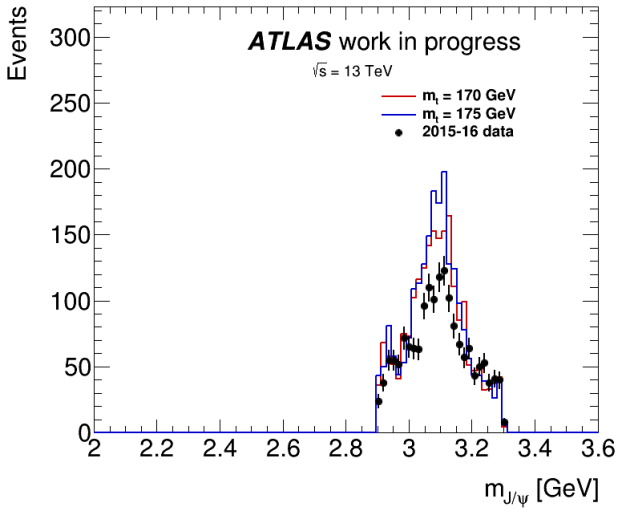

FIGURE 6.26: The mass distribution of the J/ψ candidates in the signal region after applying a tighter J/ψ mass selection cut to be between 2.9 GeV and 3.3 GeV for data and the two template MC samples.

6.7.2.2 Additional pseudo-proper time cut

From the pseudo-proper time distribution in Figure 6.18, the prompt and non-prompt background can be reduced by applying an additional pseudo-proper time cut to the J/ψ candidates. A possible cut was to select J/ψ candidates which had a pseudo-proper time greater than 0 ps (i.e. $\tau > 0$ ps). After applying this additional selection criteria to the two template MC samples, the probability density function had to be refitted. The probability density function fit result can be seen in Figure 6.27 and the parameter fit results in Table 6.7.

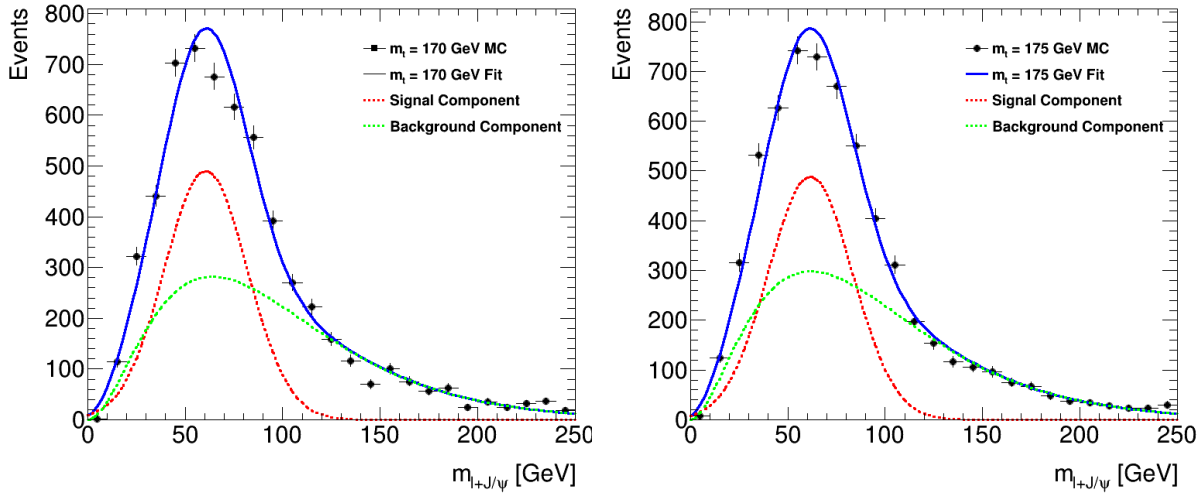

FIGURE 6.27: The invariant mass distribution of the J/ψ and lepton candidates for the 170 GeV (left) and 175 GeV (right) MC samples in the signal region after applying a pseudo-proper time selection cut of $\tau > 0$ ps on the J/ψ candidates. The probability density function fit and the signal and background components are shown.

Parameter	m_t = 170 GeV MC	m_t = 175 GeV MC
Fraction of signal component	0.445 ± 0.039	0.436 ± 0.039
μ_{Gauss}	60.59 ± 0.91	61.57 ± 0.91
σ_{Gauss}	21.27 ± 0.74	21.59 ± 0.74
Γ_γ	3.05 ± 0.12	2.94 ± 0.11
Γ_β	31.33 ± 1.56	31.90 ± 1.56

TABLE 6.7: Parameter fit results of the two $t\bar{t}$ MC samples after applying an additional pseudo-proper time selection cut of $\tau > 0$ on the J/ψ candidates.

After applying this additional pseudo-proper time selection, the background J/ψ contributions is reduced and the signal to background ratio improves. This can be seen by the increase in the signal component in both the 170 GeV and 175 GeV samples. Despite the limited amount of statistics after applying this τ cut, the fits converge and both sets of parameters agree within uncertainty. The interpolation was made to data and the statistical uncertainty increased from 2.87 GeV to 4.63 GeV. However, no convergence was found which is believed to be due to limited statistics and therefore, the result cannot be trusted.

6.7.2.3 Tighter J/ψ mass and an additional pseudo-proper time cut

The previous sections applied the tighter selections individually and showed that the signal to background ratio improves in both template samples after applying the pseudo-proper time cut but only the 175 GeV sample signal to background ratio improved after applying the mass cut. However, the reduction in signal in the 170 GeV is believed to be due to limited statistics. Under Section 6.6.3, the signal to background ratio should improve even further if both selection cuts were applied. After applying both selection cuts to the J/ψ candidates in the two template MC samples, the probability density function had to be refitted. The probability density function fit result can be seen in Figure 6.28 and the parameter fit results in Table 6.8.

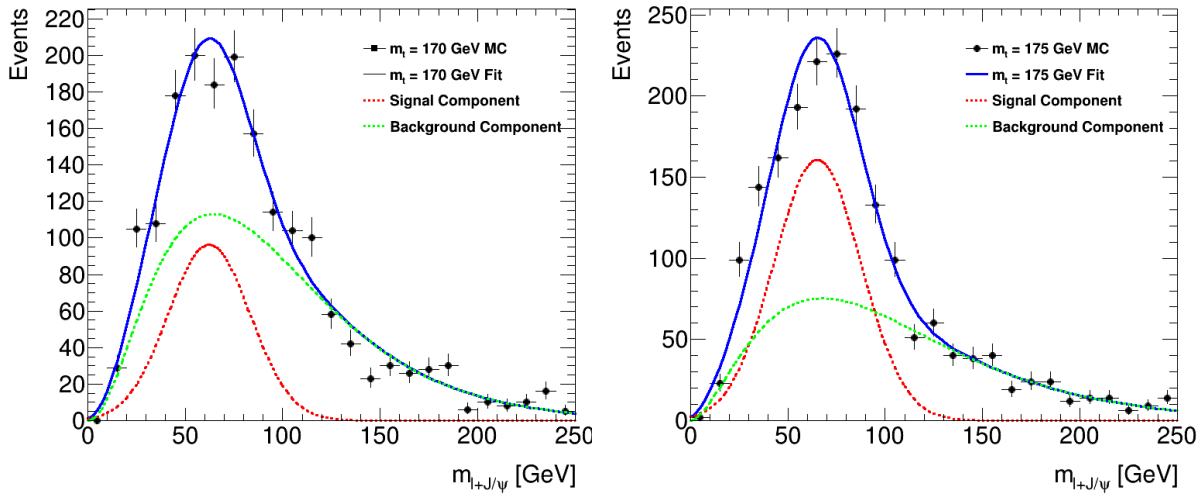

FIGURE 6.28: The invariant mass distribution of the J/ψ and lepton candidates for the 170 GeV (left) and 175 GeV (right) MC samples in the signal region after applying a tighter J/ψ mass selection cut to be between 2.9 GeV and 3.3 GeV and a pseudo-proper time selection cut of $\tau > 0$ ps on the J/ψ candidates. The probability density function fit and the signal and background components are shown.

Parameter	m_t = 170 GeV MC	m_t = 175 GeV MC
Fraction of signal component	0.285 ± 0.072	0.479 ± 0.065
μ_{Gauss}	62.31 ± 2.69	65.18 ± 1.49
σ_{Gauss}	20.91 ± 1.97	22.24 ± 1.28
Γ_γ	3.20 ± 0.19	2.81 ± 0.21
Γ_β	29.35 ± 2.29	37.29 ± 3.58

TABLE 6.8: Parameter fit results of the two $t\bar{t}$ MC samples after applying a tighter mass selection between 2.9 GeV and 3.3 GeV and an additional pseudo-proper time selection $\tau > 0$ ps on the J/ψ candidates.

After applying both cuts, the signal component decreases in the 170 GeV sample but increases in the 175 GeV sample. The decrease in the 170 GeV sample can once again be attributed the limited statistics and limited J/ψ candidates at the peak of the mass distribution of the J/ψ candidates (see Figure 6.29). Figure 6.29 shows the mass distribution of the J/ψ candidates after both selection cuts were applied. The interpolation was made to data and the statistical uncertainty improved from 2.87 GeV to 0.30 GeV. However, no convergence was found which is believed to be due to limited statistics and therefore, the result cannot be trusted. Since the signal to background ratio increases as the selection cuts are applied and with more statistics, a convergence could be found and the statistical uncertainty in the mass measurement should improve.

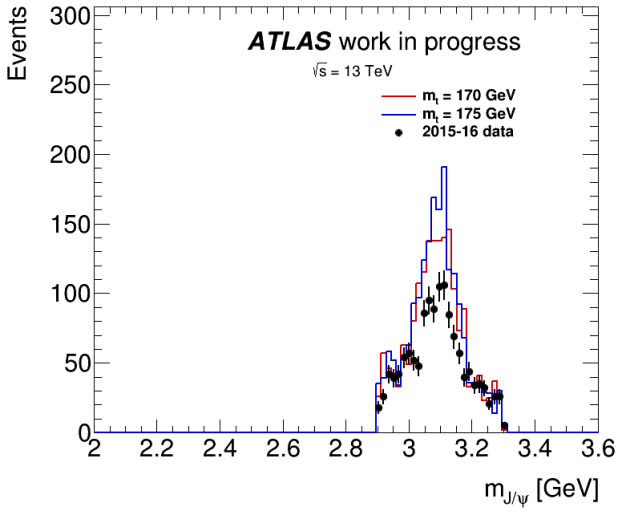

FIGURE 6.29: The mass distribution of the J/ψ candidates in the signal region after applying a tighter J/ψ mass selection cut to be between 2.9 GeV and 3.3 GeV and a pseudo-proper time selection cut of $\tau > 0$ ps on the J/ψ candidates for data and the two template MC samples.

Chapter 7

Conclusion

The top quark is not only the heaviest quark but also the heaviest known fundamental particle within the SM. The top quark has a uniquely high coupling with the Higgs boson and therefore, is a key link in understanding the Higgs sector in greater detail. The mass of the top quark, however, is a very important property of the top quark. The mass of the top quark brings about many questions, specifically, on the fact that its almost forty times larger than the b quark mass which is the second heaviest quark within the SM. Other than the enormity of the top quark mass compared to other quarks, its mass provides a good test of physics which go BSM as well as (together with the Higgs mass) determines the vacuum stability of the SM. Therefore, precision measurements of the top quark mass is of utmost importance.

The common lepton + jets, dilepton + jets and all-jets channels, which have no selection criteria on J/ψ mesons, provide precise measurements of the top quark mass as its average relative uncertainty is 0.23 %. However, the vacuum stability of the SM and models which describe the physics BSM require an even more precise measurement. These common channels all suffer from the uncertainty which are derived from jets and thus, the uncertainty can only be reduced if the reconstruction of jets improves. There are other uncommon channels which could be used to determine the top quark mass and reduce the aforementioned jet uncertainty by combining other top quark decay products to determine its mass. One of these uncommon experimental signatures is the lepton+jets(b-tagged)+J/ψ channel where the J/ψ comes from B-hadron decays and the J/ψ decays into two oppositely charged muons. This uncommon signature is limited by the number of events as the branching fraction of these processes are very small. This uncommon channel became viable as enough data became available at the LHC. The CMS collaboration provided the first top quark mass measurement within this channel but the uncertainty in the measurement was still high. However, by further investigating the objects within this channel, this uncertainty can be reduced.

This analysis investigated this uncommon channel using proton-proton collision data collected by the ATLAS detector in 2015 and 2016 which corresponded to a total integrated luminosity of 36.1 fb^{-1}. This data sample underwent a preselection process which not only stored events where two muons which produced an invariant mass around the mass peak of the J/ψ meson but also tagged the muons which decayed from these J/ψ mesons. This meant that the background contamination could be reduced by only selecting J/ψ mesons which came from these muons. However, these muons could have originated from other objects such as jets or from jets which were mis-reconstructed as muons. This also applies to the muons and electrons which came from the decay of the W boson. Therefore, these non-prompt and fake lepton contributions had to be determined. The matrix method technique defined by the top analysis groups within the ATLAS experiment which determines this non-prompt and fake lepton background contribution was applied. However, this method overestimated the non-prompt and fake lepton contribution in the muon channel but more accurately estimated it in the electron channel. Due to this difference, this method was not the right approach to determine the non-prompt or fake lepton contribution in the signal region. A possible approach would be to include further selection criteria on the J/ψ candidates and/ or the number of (b-tagged) jets which could produce reasonably well estimated lepton background contributions in both channels.

This uncommon experimental signature is dominated by top quark events (as can be seen in Figures 6.10 - 6.16) and therefore, the majority of the selected objects within this signature stems from the top quark decay mode of interest in Equation 6.1. There are, however, very small contributions from background processes within this signature and thus, this experimental signature provides a valid approach to measure the mass of the top quark. Despite the fact that the selected objects mostly originated from top quark decays, most of the selected J/ψ mesons did not originate from top quark B-hadron decays (see Figure 6.19). Many of the selected J/ψ mesons were actually originating from background processes. This experimental signature relied on J/ψ candidates originating from top quark B-hadron decays which can be distinguished from other J/ψ candidates due to the displayed decay vertex of B-hadrons. To distinguish between signal non-prompt and background J/ψ candidates selected in the signal region, a pseudo-proper time τ variable was used. Due to the selection of J/ψ candidates being dependent on the mass distribution and the distinguishing capabilities of the pseudo-proper time of the J/ψ candidates, the different J/ψ contributions were determined. A two-dimensional fit was applied to these distributions and the different J/ψ contributions were shown in Figure 6.18. From this result, tighter selection cuts on the mass and pseudo-proper time of the J/ψ candidates could be used to reduce the background J/ψ contributions. These additional selection cuts on the J/ψ candidates were implemented (i.e. 2.9 GeV $< m_{J/\psi} <$ 3.3 GeV and $\tau > 0$ ps) separately and together, and the result in each case was an improvement in the signal to background ratio (see Figures 6.20 and 6.21).

The invariant mass of the lepton and J/ψ distribution is sensitive to the top quark mass and therefore, is used to determine the top quark mass through a maximum likelihood method. This was done using a template morphing technique which used predefined top mass templates and linearly interpolates them to determine which top mass value produced the invariant mass distribution within this uncommon experimental signature. This analysis was primarily focused on the uncertainty in the top mass measurement and therefore, only the uncertainty was quoted. The probability density function which modelled the invariant mass distribution was defined as the sum of a Gaussian distribution for the signal component and a Gamma distribution for the background component. Before reducing the J/ψ background contributions, the two templates showed a sizable background component in the invariant mass distribution. After interpolating these two templates, no convergence was found and the statistical uncertainty in the mass measurement could not be trusted. This non-convergence is believed to be due to the limited amount of statistics. After applying a tighter J/ψ mass selection between 2.9 GeV and 3.3 GeV but before applying the pseudo-proper time selection, the signal component reduced in the 170 GeV sample whereas it should have increased as was the case in the 175 GeV sample (Figure 6.25 and Table 6.6). This was due to the limited statistics and the limited J/ψ candidates at the peak in the J/ψ mass distribution (see Figure 6.26). However, after applying a pseudo-proper time selection of $\tau > 0$ ps but before the tighter J/ψ mass selection, the signal component increased in both template samples showing an improvement in the signal to background ratio (Figure 6.27 and Table 6.7). After applying both selections, the 170 GeV signal component decreased but the 175 GeV signal component increased (Figure 6.28 and Table 6.8). This is believed to be due to the limited statistics and limited J/ψ candidates at the peak in the mass distribution of the 170 GeV sample (see Figure 6.29). Due to the limited statistics, no convergences was found to the interpolation of the two templates to data after applying the tighter selections individually and together, and therefore, a quantitative result could not be shown which would depict the improvement in signal to background and, subsequently, an improvement in the mass measurement of the top quark.

This channel not only provides a valid approach to measure the mass of the top quark but, after reducing background J/ψ candidates, could provide a more precise measurement of the mass of the top quark. There are other ways which could be the focus of further studies to reduce the background contributions even further. When selecting the objects in the signal region, a ΔR selection between the lepton from the W boson and the J/ψ meson from B-hadron decays could be implemented to ensure these decay products kinematics originate from the same top quark. In this instance, the invariant mass of the lepton+J/ψ distribution should predominantly consist of the signal component. During this project, work was done to implement an event filter which only produced J/ψ candidates originating from B-hadron decays. This will reduce the background J/ψ contributions significantly and also produce top quark events with J/ψ mesons originating from top quark B-hadron decays. This project showed that $t\bar{t}$ and, subsequently,

top quark events describe the data in this signal region very well but these top quark events consist of J/ψ candidates not only originating from top quark B-hadron decays. Therefore, this event filter will reduce the top quark signal contributions in the signal region by reducing the background J/ψ mesons and thus, show the need for the non-prompt or fake lepton background contribution in the signal region. Many further studies need to be done in order to measure the top quark mass within this experimental signature. These further studies include evaluating the systematic uncertainties within this experimental signature, determining the non-prompt or fake lepton background contribution from control and validation regions which are closely linked to this experimental signature and including the data taken by the ATLAS detector in 2017 and 2018 which corresponded to an integrated luminosity of ~ 113 fb^{-1} (i.e. triple the amount of statistics used in this analysis) in order to improve the statistics and measure the mass of the top quark in this experimental signature.

Appendix A

Signal region object kinematics

The following figures show the overestimated non-prompt or fake lepton background contribution in the signal region object kinematic distributions in the muon channel.

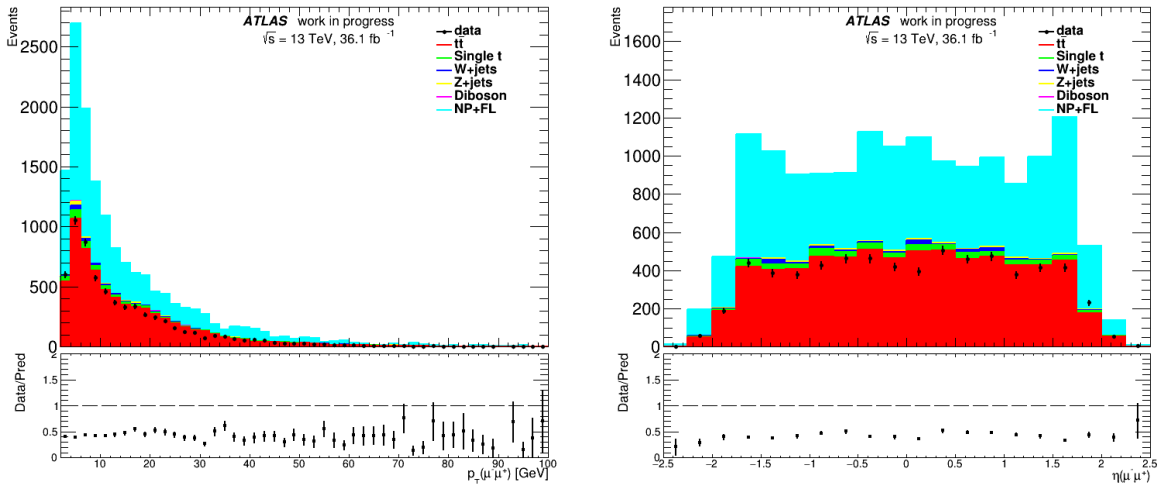

FIGURE A.1: The upper plot shows the distributions of the transverse momentum (left) and pseudorapidity (right) of the muon candidates coming from the J/ψ in the signal region muon channel. These distributions contain the data, the contributions from the different signal and background SM processes and the contributions from non-prompt or fake lepton backgrounds. Only the statistical uncertainty in the data is shown. The lower plot shows the ratio between the data and the theoretical predictions.

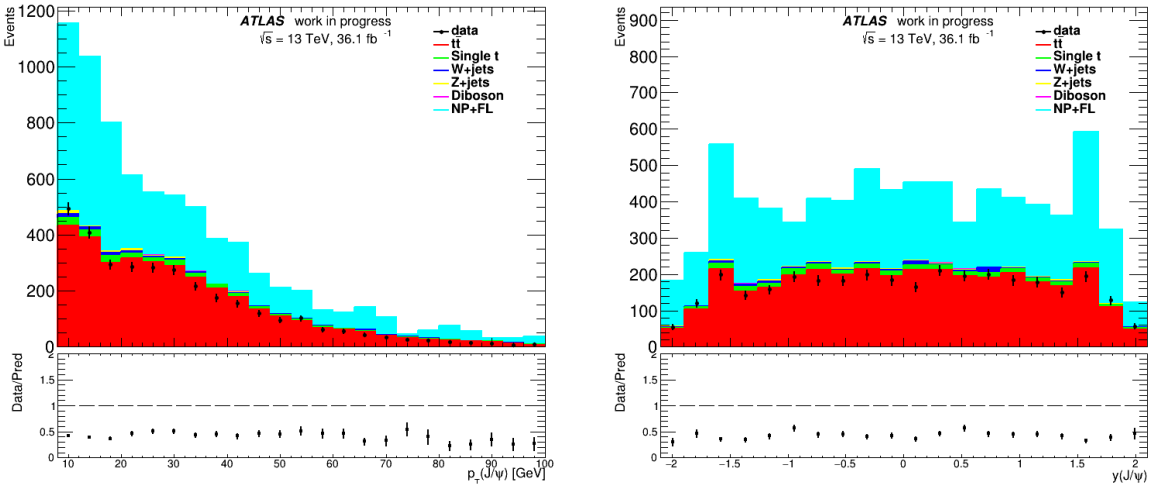

FIGURE A.2: The upper plot shows the distributions of the transverse momentum (left) and pseudorapidity (right) of the J/ψ candidates in the signal region muon channel. These distributions contain the data, the contributions from the different signal and background SM processes and the contribution from non-prompt or fake lepton backgrounds. Only the statistical uncertainty in the data is shown. The lower plot shows the ratio between the data and the theoretical predictions.

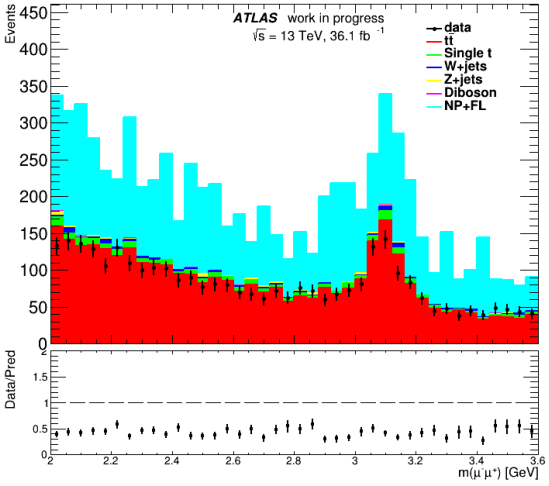

FIGURE A.3: The upper plot shows the invariant mass distribution of the muon pairs matched to a common vertex in the signal region muon channel. This distribution contains the data, the contributions from the different signal and background SM processes and the contribution from non-prompt or fake lepton backgrounds. Only the statistical uncertainty in the data is shown. The peak within the plot represents the resonant J/ψ meson mass. The lower plot shows the ratio between the data and the theoretical predictions.

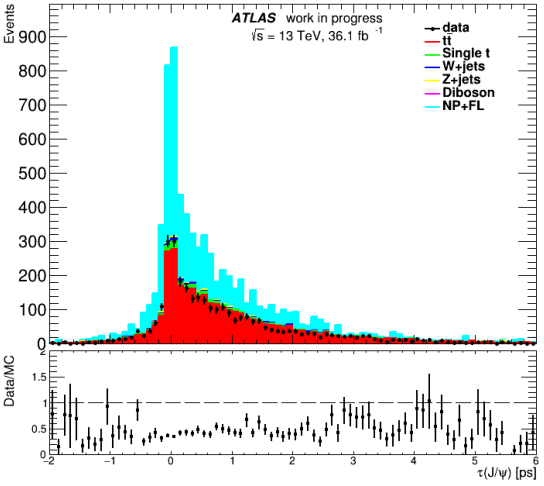

FIGURE A.4: The upper plot shows the pseudo-proper time distribution of the J/ψ candidates in the signal region muon channel. This distribution contains the data, the contributions from the different signal and background SM processes and the contribution from non-prompt or fake lepton backgrounds. Only the statistical uncertainty in the data is shown. The peak within the plot represents the contribution from prompt J/ψ mesons. The lower plot shows the ratio between the data and the theoretical predictions.

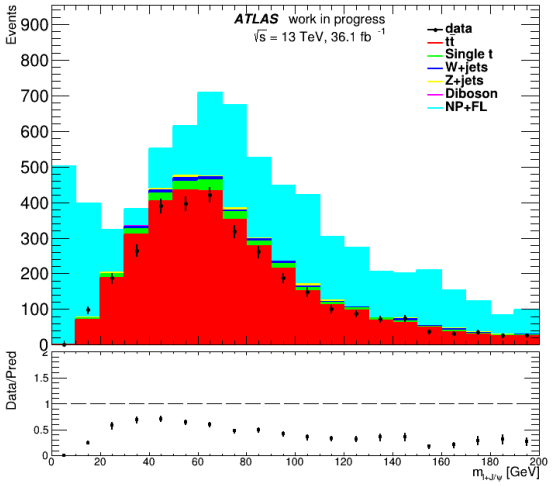

FIGURE A.5: The upper plot shows the invariant mass distribution of the lepton and J/ψ candidates in the signal region muon channel. This distributions contains the data, the contributions from the different signal and background SM processes and the contribution from non-prompt or fake lepton backgrounds. Only the statistical uncertainty in the data is shown. The peak within the plot represents the signal contribution while the tail represents the background contribution to the top mass value which produced this distribution. The lower plot shows the ratio between the data and the theoretical predictions.

Bibliography

[1] F. Abe et al. Observation of top quark production in $\bar{p}p$ collisions. *Phys. Rev. Lett.*, 74: 2626–2631, 1995. doi: 10.1103/PhysRevLett.74.2626.

[2] S. Abachi et al. Observation of the top quark. *Phys. Rev. Lett.*, 74:2632–2637, 1995. doi: 10.1103/PhysRevLett.74.2632.

[3] Victor Mukhamedovich Abazov et al. Determination of the pole and $\overline{MS}$ masses of the top quark from the $t\bar{t}$ cross section. *Phys. Lett.*, B703:422–427, 2011. doi: 10.1016/j.physletb.2011.08.015.

[4] S. Moch. Precision determination of the top-quark mass. *PoS*, LL2014:054, 2014. doi: 10.22323/1.211.0054.

[5] S. Heinemeyer, S. Kraml, W. Porod, and G. Weiglein. Physics impact of a precise determination of the top quark mass at an e^+e^- linear collider. *JHEP*, 09:075, 2003. doi: 10.1088/1126-6708/2003/09/075.

[6] Michele Gallinaro. Top quark physics: A tool for discoveries. *Journal of Physics: Conference Series*, 447(1):012012, 2013. URL http://stacks.iop.org/1742-6596/447/i=1/a=012012.

[7] Giorgio Cortiana. Top-quark mass measurements: review and perspectives. *Rev. Phys.*, 1: 60–76, 2016. doi: 10.1016/j.revip.2016.04.001.

[8] Giuseppe Degrassi, Stefano Di Vita, Joan Elias-Miro, Jose R. Espinosa, Gian F. Giudice, Gino Isidori, and Alessandro Strumia. Higgs mass and vacuum stability in the Standard Model at NNLO. *JHEP*, 08:098, 2012. doi: 10.1007/JHEP08(2012)098.

[9] M. Baak, J. Cth, J. Haller, A. Hoecker, R. Kogler, K. Mnig, M. Schott, and J. Stelzer. The global electroweak fit at NNLO and prospects for the LHC and ILC. *Eur. Phys. J.*, C74: 3046, 2014. doi: 10.1140/epjc/s10052-014-3046-5.

[10] Fedor Bezrukov and Mikhail Shaposhnikov. Why should we care about the top quark Yukawa coupling? *J. Exp. Theor. Phys.*, 120:335–343, 2015. doi: 10.1134/S1063776115030152. [Zh. Eksp. Teor. Fiz.147,389(2015)].

[11] Georges Aad et al. Observation of a new particle in the search for the Standard Model Higgs boson with the ATLAS detector at the LHC. *Phys. Lett.*, B716:1–29, 2012. doi: 10.1016/j.physletb.2012.08.020.

[12] Serguei Chatrchyan et al. Observation of a new boson at a mass of 125 GeV with the CMS experiment at the LHC. *Phys. Lett.*, B716:30–61, 2012. doi: 10.1016/j.physletb.2012.08.021.

[13] C. Patrignani et al. Review of Particle Physics. *Chin. Phys.*, C40(10):100001, 2016. doi: 10.1088/1674-1137/40/10/100001.

[14] Gino Isidori, Giovanni Ridolfi, and Alessandro Strumia. On the metastability of the standard model vacuum. *Nucl. Phys.*, B609:387–409, 2001. doi: 10.1016/S0550-3213(01)00302-9.

[15] Albert M Sirunyan et al. Measurement of the top quark mass using single top quark events in proton-proton collisions at $\sqrt{s} = 8$ TeV. *Eur. Phys. J.*, C77(5):354, 2017. doi: 10.1140/epjc/s10052-017-4912-8.

[16] Morad Aaboud et al. Measurement of the top quark mass in the $t\bar{t} \to$ dilepton channel from $\sqrt{s} = 8$ TeV ATLAS data. *Phys. Lett.*, B761:350–371, 2016. doi: 10.1016/j.physletb.2016.08.042.

[17] Vardan Khachatryan et al. Measurement of the top quark mass using proton-proton data at $\sqrt{(s)} = 7$ and 8 TeV. *Phys. Rev.*, D93(7):072004, 2016. doi: 10.1103/PhysRevD.93.072004.

[18] Tevatron Electroweak Working Group and T. Aaltonen. Combination of CDF and D0 results on the mass of the top quark using up 9.7 fb^{-1} at the Tevatron. *arXiv:1608.01881*, 2016.

[19] Vardan Khachatryan et al. Measurement of the mass of the top quark in decays with a J/ψ meson in pp collisions at 8 TeV. *JHEP*, 12:123, 2016. doi: 10.1007/JHEP12(2016)123.

[20] The ATLAS collaboration. Estimation of non-prompt and fake lepton backgrounds in final states with top quarks produced in proton-proton collisions at $\sqrt{s} = 8$ TeV with the ATLAS detector. 2014. URL https://cds.cern.ch/record/1319687.

[21] The ATLAS collaboration. Reconstruction of J/ψ mesons in $t\bar{t}$ final states in proton-proton collisions at $\sqrt{s} = 8$ TeV with the ATLAS detector. 2015. URL https://cds.cern.ch/record/2046216.

[22] Mark Thomson. *Modern particle physics*. Cambridge University Press, New York, 2013. ISBN 9781107034266. URL http://www-spires.fnal.gov/spires/find/books/www?cl=QC793.2.T46::2013.

[23] David Griffiths. *Introduction to elementary particles*. 2008. ISBN 9783527406012.

[24] S. L. Glashow. Partial Symmetries of Weak Interactions. *Nucl. Phys.*, 22:579–588, 1961. doi: 10.1016/0029-5582(61)90469-2.

[25] Steven Weinberg. A Model of Leptons. *Phys. Rev. Lett.*, 19:1264–1266, 1967. doi: 10.1103/PhysRevLett.19.1264.

[26] F. Englert and R. Brout. Broken Symmetry and the Mass of Gauge Vector Mesons. *Phys. Rev. Lett.*, 13:321–323, 1964. doi: 10.1103/PhysRevLett.13.321. [,157(1964)].

[27] Wikipedia. Standard Model, 2018. URL https://en.wikipedia.org/wiki/Standard_Model. Accessed: 2018-10-15.

[28] The Physicist. Q:What is the most complicated equation?, 2018. URL https://www.askamathematician.com/2018/05/q-what-is-the-most-complicated-equation/. Accessed: 2019-01-11.

[29] Julia Woithe, Gerfried J. Wiener, and Frederik F. Van der Veken. Lets have a coffee with the Standard Model of particle physics! *Phys. Educ.*, 52(3):034001, 2017. doi: 10.1088/1361-6552/aa5b25.

[30] Yong Tang. Vacuum Stability in the Standard Model. *Mod. Phys. Lett.*, A28:1330002, 2013. doi: 10.1142/S0217732313300024.

[31] Andrea Giammanco. Single top quark production at the LHC. *Rev. Phys.*, 1:1–12, 2016. doi: 10.1016/j.revip.2015.12.001.

[32] Kevin Krninger, Andreas B. Meyer, and Peter Uwer. Top-Quark Physics at the LHC. In Thomas Schrner-Sadenius, editor, *The Large Hadron Collider: Harvest of Run 1*, pages 259–300. 2015. doi: 10.1007/978-3-319-15001-7_7.

[33] Kirill Melnikov and Timo van Ritbergen. The Three loop relation between the MS-bar and the pole quark masses. *Phys. Lett.*, B482:99–108, 2000. doi: 10.1016/S0370-2693(00)00507-4.

[34] CERN. Origins, 2018. URL https://timeline.web.cern.ch/events/origins. Accessed: 2018-12-10.

[35] CERN. The European Organization for Nuclear Research is born, 2018. URL https://timeline.web.cern.ch/events/the-european-organization-for-nuclear-research-is-born. Accessed: 2018-12-10.

[36] CERN. Our Member States, 2018. URL https://home.cern/about/who-we-are/our-governance/member-states. Accessed: 2018-12-10.

[37] CERN. Where did it all begin?, 2018. URL https://home.cern/about/who-we-are/our-history. Accessed: 2018-12-10.

[38] CERN. CERN's first accelerator - the Synchrocyclotron - starts up, 2018. URL https://timeline.web.cern.ch/cerns-first-accelerator-synchrocyclotron-starts. Accessed: 2018-12-10.

[39] CERN. W and Z particles discovered, 2018. URL https://timeline.web.cern.ch/events/w-and-z-particles-discovered. Accessed: 2018-12-10.

[40] CERN. The birth of the Web, 2018. URL https://home.cern/science/computing/birth-web. Accessed: 2018-12-10.

[41] CERN. First antiatoms produced: antihydrogen, at CERN, 2018. URL https://timeline.web.cern.ch/events/first-antiatoms-produced-antihydrogen-at-cern. Accessed: 2018-12-10.

[42] CERN. The Higgs boson, 2018. URL https://home.cern/science/physics/higgs-boson. Accessed: 2018-12-10.

[43] Esma Mobs. The CERN accelerator complex. August 2018. URL https://cds.cern.ch/record/2636343. General Photo.

[44] Lyndon Evans and Philip Bryant. LHC Machine. *JINST*, 3:S08001, 2008. doi: 10.1088/1748-0221/3/08/S08001.

[45] CERN. Large Electron-Positron collider: First injection, 2018. URL https://timeline.web.cern.ch/events/large-electron-positron-collider-first-injection. Accessed: 2018-12-11.

[46] CERN. The accelerator complex, 2018. URL https://home.cern/science/accelerators/accelerator-complex. Accessed: 2018-12-11.

[47] LHC Guide. Mar 2017. URL https://cds.cern.ch/record/2255762.

[48] Georges Aad et al. Improved luminosity determination in pp collisions at $\sqrt{s} = 7$ TeV using the ATLAS detector at the LHC. *Eur. Phys. J.*, C73(8):2518, 2013. doi: 10.1140/epjc/s10052-013-2518-3.

[49] ATLAS Collaboration. LuminosityPublicResultsRun2, 2018. URL https://twiki.cern.ch/twiki/bin/view/AtlasPublic/LuminosityPublicResultsRun2. Accessed: 2019-01-10.

[50] G. Aad et al. The ATLAS Experiment at the CERN Large Hadron Collider. *JINST*, 3: S08003, 2008. doi: 10.1088/1748-0221/3/08/S08003.

[51] ATLAS Collaboration. The Collaboration, 2018. URL https://atlas.cern/discover/collaboration. Accessed: 2018-12-13.

[52] ATLAS Collaboration. The Physics, 2018. URL https://atlas.cern/discover/physics. Accessed: 2018-12-13.

[53] ATLAS Collaboration. Detector & Technology, 2018. URL https://atlas.cern/discover/detector. Accessed: 2018-12-13.

[54] Joao Pequenao. Computer generated image of the whole ATLAS detector. Mar 2008. URL https://cds.cern.ch/record/1095924.

[55] Matthias Schott and Monica Dunford. Review of single vector boson production in pp collisions at $\sqrt{s} = 7$ TeV. *Eur. Phys. J.*, C74:2916, 2014. doi: 10.1140/epjc/s10052-014-2916-1.

[56] ATLAS Collaboration. Magnet System, 2019. URL https://atlas.cern/discover/detector/magnet-system. Accessed: 2019-01-07.

[57] M Capeans, G Darbo, K Einsweiller, M Elsing, T Flick, M Garcia-Sciveres, C Gemme, H Pernegger, O Rohne, and R Vuillermet. ATLAS Insertable B-Layer Technical Design Report. Technical Report CERN-LHCC-2010-013. ATLAS-TDR-19, Sep 2010. URL https://cds.cern.ch/record/1291633.

[58] Joao Pequenao. Computer generated image of the ATLAS inner detector. Mar 2008. URL https://cds.cern.ch/record/1095926.

[59] Joao Pequenao. Computer generated image of the ATLAS calorimeter. Mar 2008. URL https://cds.cern.ch/record/1095927.

[60] Joao Pequenao. Computer generated image of the ATLAS Muons subsystem. Mar 2008. URL https://cds.cern.ch/record/1095929.

[61] Peter Jenni, Markus Nordberg, Marzio Nessi, and Kerstin Jon-And. *ATLAS Forward Detectors for Measurement of Elastic Scattering and Luminosity*. Technical Design Report ATLAS. CERN, Geneva, 2008. URL https://cds.cern.ch/record/1095847.

[62] Peter Jenni and Marzio Nessi. ATLAS Forward Detectors for Luminosity Measurement and Monitoring. Technical Report CERN-LHCC-2004-010. LHCC-I-014, CERN, Geneva, Mar 2004. URL https://cds.cern.ch/record/721908. revised version number 1 submitted on 2004-03-22 14:56:11.

[63] Peter Jenni, Marzio Nessi, and Markus Nordberg. Zero Degree Calorimeters for ATLAS. Technical Report CERN-LHCC-2007-001. LHCC-I-016, CERN, Geneva, Jan 2007. URL http://cds.cern.ch/record/1009649.

[64] L Adamczyk, E Bana, A Brandt, M Bruschi, S Grinstein, J Lange, M Rijssenbeek, P Sicho, R Staszewski, T Sykora, M Trzebiski, J Chwastowski, and K Korcyl. Technical Design Report for the ATLAS Forward Proton Detector. Technical Report CERN-LHCC-2015-009. ATLAS-TDR-024, May 2015. URL https://cds.cern.ch/record/2017378.

[65] ATLAS Collaboration. ATLAS Forward Detectors. General Photo, Jun 2018. URL http://cds.cern.ch/record/2627582.

[66] Joao Pequenao and Paul Schaffner. An computer generated image representing how ATLAS detects particles. Jan 2013. URL https://cds.cern.ch/record/1505342.

[67] T Cornelissen, M Elsing, S Fleischmann, W Liebig, E Moyse, and A Salzburger. Concepts, Design and Implementation of the ATLAS New Tracking (NEWT). Technical Report ATL-SOFT-PUB-2007-007. ATL-COM-SOFT-2007-002, CERN, Geneva, Mar 2007. URL http://cds.cern.ch/record/1020106.

[68] *ATLAS inner detector: Technical Design Report, 1.* Technical Design Report ATLAS. CERN, Geneva, 1997. URL http://cds.cern.ch/record/331063.

[69] Electron efficiency measurements with the ATLAS detector using the 2015 LHC proton-proton collision data. Technical Report ATLAS-CONF-2016-024, CERN, Geneva, Jun 2016. URL http://cds.cern.ch/record/2157687.

[70] Georges Aad et al. Muon reconstruction performance of the ATLAS detector in protonproton collision data at $\sqrt{s}$ =13 TeV. *Eur. Phys. J.*, C76(5):292, 2016. doi: 10.1140/epjc/s10052-016-4120-y.

[71] G. Arnison et al. Hadronic Jet Production at the CERN Proton - anti-Proton Collider. *Phys. Lett.*, 132B:214, 1983. doi: 10.1016/0370-2693(83)90254-X.

[72] Gerald C. Blazey et al. Run II jet physics. In *QCD and weak boson physics in Run II. Proceedings, Batavia, USA, March 4-6, June 3-4, November 4-6, 1999*, pages 47–77, 2000. URL http://lss.fnal.gov/cgi-bin/find_paper.pl?conf-00-092.

[73] Gavin P. Salam and Gregory Soyez. A Practical Seedless Infrared-Safe Cone jet algorithm. *JHEP*, 05:086, 2007. doi: 10.1088/1126-6708/2007/05/086.

[74] S. Catani, Yuri L. Dokshitzer, M. H. Seymour, and B. R. Webber. Longitudinally invariant K_t clustering algorithms for hadron hadron collisions. *Nucl. Phys.*, B406:187–224, 1993. doi: 10.1016/0550-3213(93)90166-M.

[75] Matteo Cacciari, Gavin P. Salam, and Gregory Soyez. The anti-k_t jet clustering algorithm. *JHEP*, 04:063, 2008. doi: 10.1088/1126-6708/2008/04/063.

[76] A Cambridge-Aachen (C-A) based Jet Algorithm for boosted top-jet tagging. Technical Report CMS-PAS-JME-09-001, CERN, Geneva, Jul 2009. URL https://cds.cern.ch/record/1194489.

[77] Gavin P. Salam. Towards Jetography. *Eur. Phys. J.*, C67:637–686, 2010. doi: 10.1140/epjc/s10052-010-1314-6.

[78] Expected performance of the ATLAS b-tagging algorithms in Run-2. Technical Report ATL-PHYS-PUB-2015-022, CERN, Geneva, Jul 2015. URL https://cds.cern.ch/record/2037697.

[79] D. J. Lange. The EvtGen particle decay simulation package. *Nucl. Instrum. Meth.*, A462: 152–155, 2001. doi: 10.1016/S0168-9002(01)00089-4.

[80] Stefano Frixione, Paolo Nason, and Carlo Oleari. Matching NLO QCD computations with Parton Shower simulations: the POWHEG method. *JHEP*, 11:070, 2007. doi: 10.1088/1126-6708/2007/11/070.

[81] Torbjorn Sjostrand, Stephen Mrenna, and Peter Z. Skands. PYTHIA 6.4 Physics and Manual. *JHEP*, 05:026, 2006. doi: 10.1088/1126-6708/2006/05/026.

[82] Peter Zeiler Skands. Tuning Monte Carlo Generators: The Perugia Tunes. *Phys. Rev.*, D82:074018, 2010. doi: 10.1103/PhysRevD.82.074018.

[83] J. Alwall, R. Frederix, S. Frixione, V. Hirschi, F. Maltoni, O. Mattelaer, H. S. Shao, T. Stelzer, P. Torrielli, and M. Zaro. The automated computation of tree-level and next-to-leading order differential cross sections, and their matching to parton shower simulations. *JHEP*, 07:079, 2014. doi: 10.1007/JHEP07(2014)079.

[84] Torbjorn Sjostrand, Stephen Mrenna, and Peter Z. Skands. A Brief Introduction to PYTHIA 8.1. *Comput. Phys. Commun.*, 178:852–867, 2008. doi: 10.1016/j.cpc.2008.01.036.

[85] ATLAS Run 1 Pythia8 tunes. Technical Report ATL-PHYS-PUB-2014-021, CERN, Geneva, Nov 2014. URL https://cds.cern.ch/record/1966419.

[86] Richard D. Ball et al. Parton distributions with LHC data. *Nucl. Phys.*, B867:244–289, 2013. doi: 10.1016/j.nuclphysb.2012.10.003.

[87] T. Gleisberg, Stefan. Hoeche, F. Krauss, M. Schonherr, S. Schumann, F. Siegert, and J. Winter. Event generation with SHERPA 1.1. *JHEP*, 02:007, 2009. doi: 10.1088/1126-6708/2009/02/007.

[88] Hung-Liang Lai, Marco Guzzi, Joey Huston, Zhao Li, Pavel M. Nadolsky, Jon Pumplin, and C. P. Yuan. New parton distributions for collider physics. *Phys. Rev.*, D82:074024, 2010. doi: 10.1103/PhysRevD.82.074024.

[89] Georges Aad et al. Measurement of the production cross section of prompt J/ψ mesons in association with a $W^{\pm}$ boson in pp collisions at $\sqrt{s} = 7$ TeV with the ATLAS detector. *JHEP*, 04:172, 2014. doi: 10.1007/JHEP04(2014)172.

[90] G. Aad et al. The ATLAS Simulation Infrastructure. *Eur. Phys. J.*, C70:823–874, 2010. doi: 10.1140/epjc/s10052-010-1429-9.

[91] S. Agostinelli et al. GEANT4: A Simulation toolkit. *Nucl. Instrum. Meth.*, A506:250–303, 2003. doi: 10.1016/S0168-9002(03)01368-8.

[92] Optimisation of the ATLAS b-tagging performance for the 2016 LHC Run. Technical Report ATL-PHYS-PUB-2016-012, CERN, Geneva, Jun 2016. URL https://cds.cern.ch/record/2160731.

[93] Georges Aad et al. Measurement of the production cross section of prompt J/ψ mesons in association with a $W^{\pm}$ boson in pp collisions at $\sqrt{s} = 7$ TeV with the ATLAS detector. *JHEP*, 04:172, 2014. doi: 10.1007/JHEP04(2014)172.

[94] Georges Aad et al. Measurement of hard double-parton interactions in $W(\rightarrow l\nu)+$ 2 jet events at $\sqrt{s}$=7 TeV with the ATLAS detector. *New J. Phys.*, 15:033038, 2013. doi: 10.1088/1367-2630/15/3/033038.

[95] Roel Aaij et al. Measurement of forward J/ψ production cross-sections in pp collisions at $\sqrt{s} = 13$ TeV. *JHEP*, 10:172, 2015. doi: 10.1007/JHEP05(2017)063,10.1007/JHEP10(2015)172. [Erratum: JHEP05,063(2017)].

[96] Georges Aad et al. Measurement of $W^{\pm}$ and Z-boson production cross sections in pp collisions at $\sqrt{s} = 13$ TeV with the ATLAS detector. *Phys. Lett.*, B759:601–621, 2016. doi: 10.1016/j.physletb.2016.06.023.

[97] Wouter Verkerke and David P. Kirkby. The RooFit toolkit for data modeling. *eConf*, C0303241:MOLT007, 2003. [,186(2003)].

[98] S Behar and Y Rozen. Top Mass Determination from J/Psi - lepton correlation. Technical Report ATL-PHYS-INT-2008-039-1. ATL-COM-PHYS-2008-045, CERN, Geneva, Apr 2008. URL https://cds.cern.ch/record/1098695.